Copyright 2012 Albert Daen Liao

PROBING THE UPPER LIMITS OF CURRENT FLOW IN ONE-DIMENSIONAL CARBON CONDUCTORS

BY

ALBERT DAEN LIAO

DISSERTATION

Submitted in partial fulfillment of the requirements
for the degree of Doctor of Philosophy in Electrical and Computer Engineering
in the Graduate College of the
University of Illinois at Urbana-Champaign, 2012

Urbana, Illinois

Doctoral Committee:

Associate Professor Eric Pop, Chair
Professor James J. Coleman
Professor William P. King
Professor Jean-Pierre Leburton
Professor Joseph W. Lyding

ABSTRACT

We use breakdown thermometry to study carbon nanotube (CNT) devices and graphene nanoribbons (GNRs) on SiO_2 substrates. Experiments and modeling find the CNT-substrate thermal coupling scales proportionally to CNT diameter. Diffuse mismatch modeling (DMM) reveals the upper limit of thermal coupling ~0.7 $WK^{-1}m^{-1}$ for the largest diameter (3-4 nm) CNTs. Similarly, we extracted the GNR thermal conductivity (TC), ~80 (130) $Wm^{-1}K^{-1}$ at 20 (600) ^oC across our samples, dominated by phonons, with estimated <10% electronic contribution. The TC of GNRs is an order of magnitude lower than that of micron-sized graphene on SiO_2, suggesting strong roles of edge and defect scattering, and the importance of thermal dissipation in small GNR devices.

We also compare the peak current density of metallic single-walled CNTs with GNRs. We find that as the "footprint" (width) between such a device and the underlying substrate decreases, heat dissipation becomes more efficient (for a given width), allowing for higher current densities. Because of their smaller dimensions and lack of edges, CNTs can carry larger current densities than GNRs, up to ~16 mA/μm for an m-SWNT with a diameter of ~0.7 nm versus ~3 mA/μm for a GNR having a width of ~15 nm. Such current densities are the highest possible in any diffusive conductor, to our knowledge.

We also study semiconducting and metallic single-walled CNTs under vacuum. Semiconducting single-wall CNTs under high electric field stress (~10 V/μm) display a remarkable current increase due to avalanche generation of free electrons and holes. Unlike in other materials, the avalanche process in such 1D quantum wires involves access to the third subband and is insensitive to temperature, but strongly dependent on diameter ~$\exp(-1/d^2)$. Comparison with a theoretical model yields a novel approach to obtain the inelastic optical phonon emission length, $\lambda_{OP,ems} \approx 15d$ nm.

We find that current in metallic single-walled CNTs does not typically saturate, unlike previous observations which suggested a maximum current of ~25 μA. In fact, at very high fields (>10 V/μm) the current continues to increase with a slope ~0.5–1 μA/V, allowing m-CNTs to reach currents well in excess of 25 μA. Subsequent modeling suggests that carriers tunnel from the contacts into higher subbands. This allows currents to reach ~30–35 μA, which correspond to a current density of ~9 mA/μm for diameters of ~1.2 nm.

To my grandparents, for all the sacrifices they made to provide a quality education for generations to come.

ACKNOWLEDGMENTS

I would like to first acknowledge my adviser, Prof. Eric Pop, for guiding me through graduate school. Your advice on topics ranging from research and academics to career decisions has played an invaluable role in shaping this thesis and my future. I would also like to thank the other members serving on my committee: Prof. Jean-Pierre Leburton, Prof. Joseph Lyding, Prof. James Coleman, and Prof. William King. The work in this thesis and my graduate studies were funded through the Nanoelectronics Research Initiative's Hans J. Coufal Fellowship.

One of the greatest resources at the University of Illinois was my fellow students. Special thanks go to Dr. Coskun Kocabas and Dr. Taner Ozel for teaching me the nuances of carbon nanotube growth and to Dr. Varun Verma for introducing me to a lot of fabrication techniques and tools in the cleanroom. I would also like to acknowledge many important conversations I had with Dr. Marcelo Kuroda. A big thanks to my fellow group members who all strive to help one another and make the Pop lab experience a fun and productive one. Particularly, I would like to thank Dr. Zhun-yong Ong and David Estrada for their great help in establishing this great Pop lab atmosphere from the beginning. I would also like to thank the helpful staff at the Micro and Nanotechnology Lab for their technical support. Last but not least, thanks to all the undergrads that put in countless hours of device mapping, upon which my research was so dependent.

During my time in graduate school I have had the privilege of working in numerous collaborations. I would like to acknowledge my Illinois collaborations with Prof. William King, Prof. Jungchul Lee, Prof. K. Jimmy Hsia, Dr. Rouholla Alizadegan, Prof. Moonsub Shim, and Cheng-Lin (Johnathon Tsai). I would also like to acknowledge my external collaborations with Prof. Hongjie Dai (Stanford), Prof. Xinran Wang (Stanford), Justin Wu (Stanford), Prof. Debdeep Jena (Notre Dame), Dr. Kristof Tahy (Notre Dame), and Dr. Curt Richter (NIST).

Finally I would like to thank all my friends and family. Thanks to my friends for providing me with the necessary distractions when I needed them. Thanks to my family for their unwavering support of this lengthy endeavor. To my father, thanks for taking an interest in my academic career and always telling me to "think big." To my mother, thanks for all the care packages you sent to give me a slice of the bay area in Illinois.

TABLE OF CONTENTS

LIST OF FIGURES

CHAPTER 1

ONE-DIMENSIONAL CARBON NANOSTRUCTURES

1.1 Introduction

Despite current success in electronic device scaling, the workhorse materials (i.e. Si and Cu) will eventually reach their physical limits. It will become impractical to construct components out of these materials as they become harder and more expensive to fabricate, or their performance and reliability wane. While there are eligible candidates scattered throughout the periodic table, carbon has emerged as a strong choice as a next generation electronic material. One reason it has attracted so much attention is that it exists in stable low-dimensional forms as balls (0-D) [1], tubes (1-D) [2], and sheets (2-D) [3]. Of these allotropes, those that are bonded in the hexagonal sp^2 configuration, shown in Fig. 1.1, have attracted a lot of attention in recent years. This is a result of possessing physical properties that are comparable to or better than other bulk materials, in spite of their nanoscale stature.

One-dimensional structures, in particular, offer great versatility either as wires or ac-

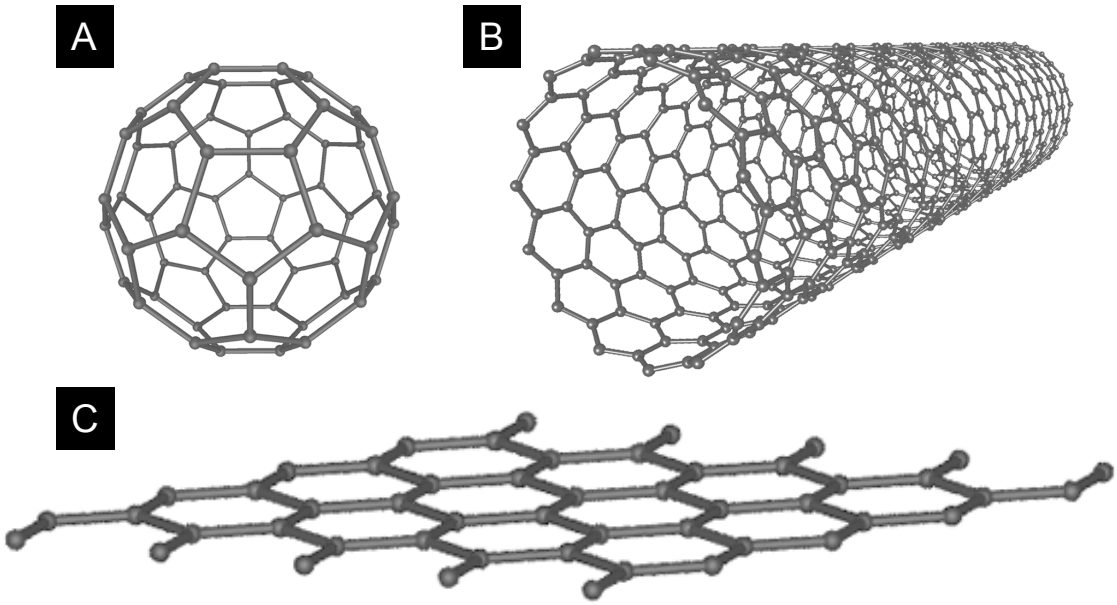

Fig. 1.1 Low-dimensional allotropes of carbon (A) fullerene (B) carbon nanotube (C) graphene. Images courtesy of Michael Ströck via Wikipedia.

tive conducting components in devices. There are currently two different 1-D carbon nano-structures, the carbon nanotube (CNT) and the graphene nanoribbon (GNR). Their wide range of promising physical properties has led to the creation and proposal of a large variety of applications. Some of these applications include transistors [4-7], interconnects [8-11] and electrodes [12], chemical and biological sensors [13-15], heaters [16], and heat sinks [17, 18].

The electronic properties of one-dimensional carbon nanostructures can be derived from the band diagram of two-dimensional graphene and graphite [19, 20]. The important feature is at the Dirac point where the conduction and valence band touch. Here the electronic bands are linear and symmetric. When the 2-D sheet is confined into one dimension, certain electronic states become forbidden. Which states are excluded depends on the direction and angle (i.e. the chirality) of the 1-D strip with respect to the lattice as illustrated in Fig. 1.2 [5]. These materials will appear metallic if the Dirac point is preserved, but will appear semiconducting if it is excluded. When all chiral possibilities are considered, one-third of the 1-D nanostructures are metallic and two-thirds are semiconducting. In the case of semiconductors, the bands are hyperbolic instead of linear.

The size of the bandgap depends on the dimensions of the sample. The bandgap of a semiconducting CNT scales inversely with the diameter as $1/d$. From tight-binding calcu-

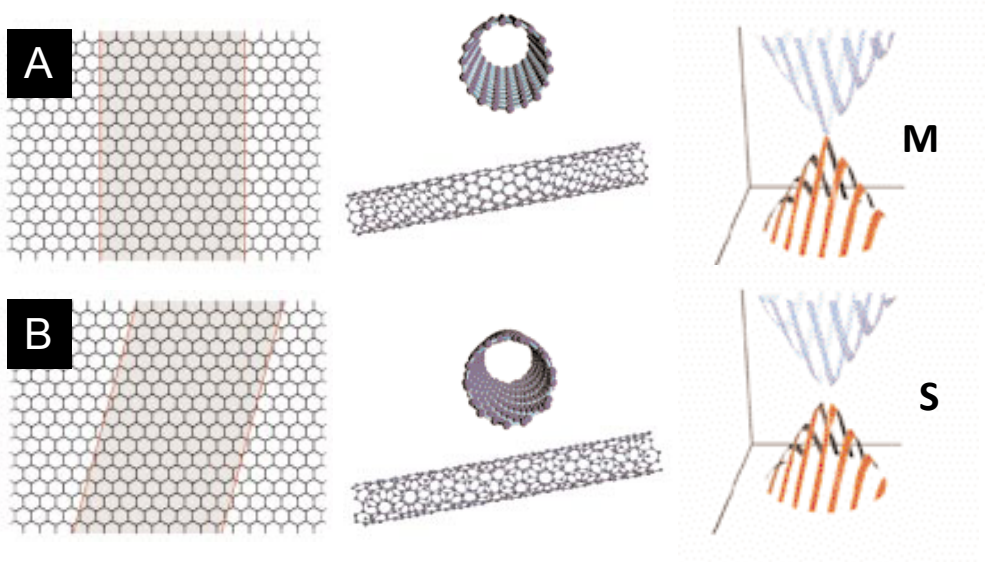

Fig. 1.2 Band structure for two carbon nanotubes with different chiralities (A) metallic and (B) semiconducting [5].

lations, the band gap is given as [21]

$$E_G = \frac{2\gamma a_{C-C}}{d} \tag{1.1}$$

where $\gamma \sim 2.9 \pm 0.1$ eV is the tight-binding overlap energy and $a_{C\text{-}C} = 0.142$ nm is the bond length between nearest neighboring carbon atoms. In addition to a diameter dependence, there is also a small chirality dependence as well [22]. Often times, however, the exact chirality is not known in experiments (see section 1.3). Several different experiments have matched the theoretical tight-binding predictions. Odom et al. used scanning tunneling microscopy (STM) to electronically probe the band gap [23], observing the inverse diameter scaling from equation 1.1. The chirality dependence on the energy gap can also be mapped out using optical methods such as Raman spectroscopy [24], photoluminescence [25], and Rayleigh scattering [26].

What make GNRs and CNTs attractive for electronic device applications are their high mobility (~10^3-10^4 cm^2/Vsec) [6, 27, 28], high maximum current density (~10^9 A/cm^2) [8, 29], and large thermal conductivity (~10^2-10^3 $Wm^{-1}K^{-1}$) [29, 30]. These values are typically better for CNTs than GNRs because the edges from GNRs often introduce edge scattering. While there have been several studies focused on measuring these properties, most do so in an ideal fashion (e.g. suspended devices and low temperature measurements). However in a practical device, CNTs and GNRs will come in contact with other materials and may be operated under more extreme conditions. There has been strong theoretical and experimental evidence showing that these physical properties can be altered when interacting with other materials [31-34]. Therefore it is critical that these interactions be properly studied, so the best design choices can be made to maximize performance and energy efficiency.

1.2 Device Fabrication

The three-terminal (source, drain, gate) device is the most popular test structure used in measuring carbon device transport. Schematics of completed CNT and GNR devices are shown in Fig. 1.3. The source and drain are used to control the lateral field and the gate is used to modulate carrier density. Typical fabrication involves depositing or growing the carbon nanostructure on top of thermally grown SiO_2. Source and drain contacts

are then defined by lithography. Optical lithography is used to fabricate channels larger than one micron and electron-beam lithography is used for anything smaller than one micron. It is typical to use a high work function material, such as Pd or Au, to form ohmic contacts as carbon is naturally doped P-type by oxygen [35, 36]. Most of the time, a thin sticking layer (~0.5 nm of Ti or Cr) is used for better adhesion to the SiO_2 surface.

There are several methods for growing or depositing CNTs. These include arc-discharge [2], laser ablation [37], and chemical vapor deposition [38]. The first CNTs were created using arc-discharge wherein an electrostatic arc is discharged between two graphite electrodes, causing soot, fullerenes, and CNTs to be produced. Later, the laser ablation method was developed. This method aims a high-powered laser at a target made from metal catalysts and graphite. These methods all required catching CNTs either on a filter or in solution and required purification steps to separate the CNT from soot. These fabrication techniques produce CNTs with lengths that are typically < 1 μm. To fabricate devices, CNTs must be spun onto a substrate. When deposited at a high density, percolating network devices can be formed. At low density, e-beam should be used to contact individual CNTs since there is no control over the placement of the CNTs on the substrate. Since these growth techniques create a mixture of CNTs having different chiralities, density ultra-centrifugation has been introduced recently as a method of separating CNTs by chirality [39].

As an alternative, chemical vapor deposition allows for CNTs to be grown directly on substrate. While still producing a mixture of different chiralities, it allows for control

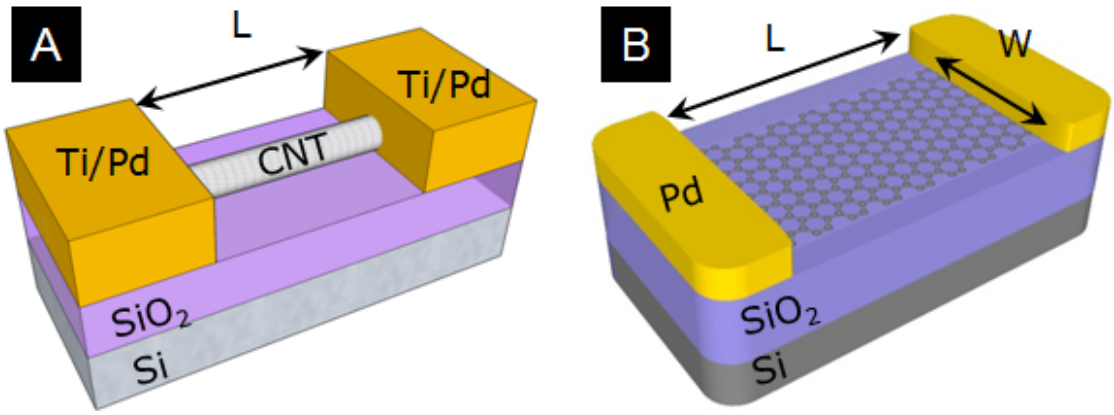

Fig. 1.3 Three-dimensional schematic of a (A) CNT and (B) GNR device.

over the starting placement of the CNT on substrate [40]. The starting placement is controlled by patterning metallic catalysts on a substrate. Next the sample is put into a tube furnace. Carbon carrying gasses are then flown into the furnace at an elevated temperature, resulting in CNTs growing out of the catalyst. In addition to controlling the initial placement of CNTs, a variety of densities and types of CNT can be grown depending on the catalyst, temperature, pressure, and gas precursors. Generally these parameters can be tuned to grow vertical forests of multiwalled CNTs, dense percolating networks, and individual CNTs. An example of each is given in Fig. 1.4. Furthermore, by controlling the growth time, the length of CNTs can be controlled to be as short as nanometers to as long as centimeters [41].

The choice of substrate can have a strong impact on CNT growth. For the most part growths are performed on SiO_2. When growing on dielectrics the CNTs generally grow in a randomly oriented direction. The exceptions are quartz [42] and sapphire [4], which have been shown to produce horizontally aligned growth. Some substrates such as silicon do not produce growth because the silicon will poison the catalyst by forming a silicide. To remedy this problem, a liner such as alumina can be deposited before depositing the catalyst. A typical catalyst choice is one that is Fe based. One method of depositing catalyst is to electron-beam evaporate a very thin layer of Fe. The thickness of Fe evaporated controls the density of the growth. For single-walled CNTs, a film of 1-3 Å (as read on the evaporator's crystal monitor) should be deposited. For mutli-walled vertical forest growth, ~1-2 nm should be deposited. Subsequent high-temperature annealing (~900 °C) then causes parts of the film to ball up and form nanoparticles from which CNTs will sprout.

Finally, the temperature, gas flow rates, and pressure can all be adjusted to control the

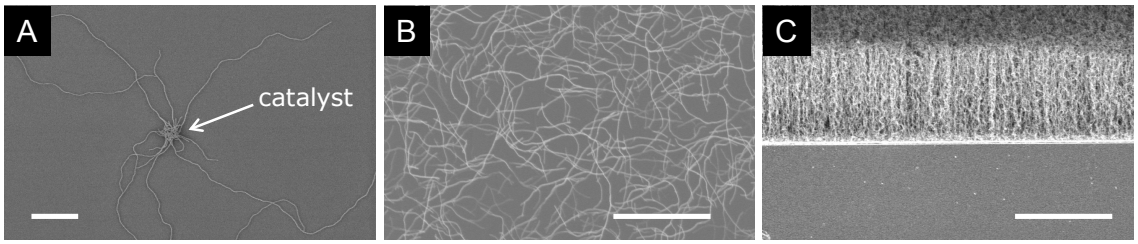

Fig. 1.4 Scanning electron microscope (SEM) images of CVD grown (A) CNTs from a patterned catalyst dot (B) CNT network image courtesy of David Estrada (C) vertical CNT forest. All scale bars represent 10 μm. In cases (A) and (C) the catalyst was Fe. In (B) the catalyst was ferretin.

concentration of carbon inside the tube furnace. Higher temperatures, higher gas flow rates, and higher pressure mean more carbon will be available. The additional carbon means an increase in density and length. If these parameters are too high, then extra soot may be produced in addition to CNTs. The extra soot can be removed with a subsequent annealing step in Ar/H_2 environment at 300 °C. The gasses used in CNT growth usually involve a carrier gas and a carbon feedstock. Argon can be flowed during the annealing step, used to form nanoparticles, to prevent further oxidation of the catalyst. Hydrogen is commonly used as the carrier gas, although Ar can be used as well to decrease the partial pressure of carbon. The type of carbon feedstock used has a strong influence on the resulting growth [43]. Methane is a good choice for lower density and single-walled growth because it breaks at a high temperature (~800-900 °C) and has one carbon atom per four hydrogen atoms. Alternatively, ethylene is a good choice for multiwalled or high-density growths because it breaks at lower temperatures (~600-700 °C) and has two carbon atoms per four hydrogen atoms.

Graphene nanoribbons can be fabricated either from larger graphene flakes [8, 44, 45] or from multiwalled CNTs [46]. The most popular way of fabricating GNRs is to use e-beam lithography to pattern a protective mask that is followed by an O_2 or H_2 plasma etch. This technique gives precise control over where the ribbons are formed. This technique also makes it easy to pattern aligned arrays of GNRs. The drawback is that the etch itself is difficult to control precisely and makes it difficult to produce very thin ribbons at a set dimension on a consistent basis. Most GNRs fabricated in this manner are ~20-50 nm wide at best, too wide to observe electron confinement effects (e.g. opening of a bandgap). To achieve thinner GNRs, multiwalled CNTs can be unzipped. These have been shown fabricate GNRs having widths of ~10-20 nm. However the drawback of this technique is that it often produces mutli-layered GNRs in addition to losing precise control over the GNRs placement.

1.3 Characterization and Measurements of Carbon Devices

1.3.1 Electrical Measurements

There are many different experimental methods used to measure and characterize carbon devices. In this section, some of the more common methods will be reviewed. The most basic of measurements are electrical measurements. Two common measurements used are an I_D-V_{GS} sweep and an I_D-V_{DS} sweep. In an I_D-V_{GS} sweep, the drain bias is held constant while the gate voltage is swept. This measurement is helpful for distinguishing between semiconducting and metallic behavior. Shown in Fig. 1.5A are typical I_D-V_{GS} sweeps for metallic and semiconducting CNTs. Devices with an ON/OFF current ratio (I_{MAX}/I_{MIN}) less than ten are considered to be metallic. Typical semiconducting devices have an ON/OFF current ratio of ~10^4 and have OFF currents that are limited by the parameter analyzer's lower detection limit. An I_D-V_{DS} measurement, shown in Fig. 1.5B, is performed at a constant gate bias while sweeping the drain bias. At low bias the current varies linearly with voltage and is most limited by the contact resistance. Thus the inverse slope can be taken to be an approximation of the contact resistance. For CNTs, the I_D-V_{DS} measurement can also be used as an approximate way to determine if there is one single-walled CNT connected between source drain electrodes. Typical single-wall CNTs display current saturation around 25-30 μA. Multiple connections will exhibit much higher currents > 40 μA.

Electrical measurements on three-terminal back-gated carbon devices will exhibit

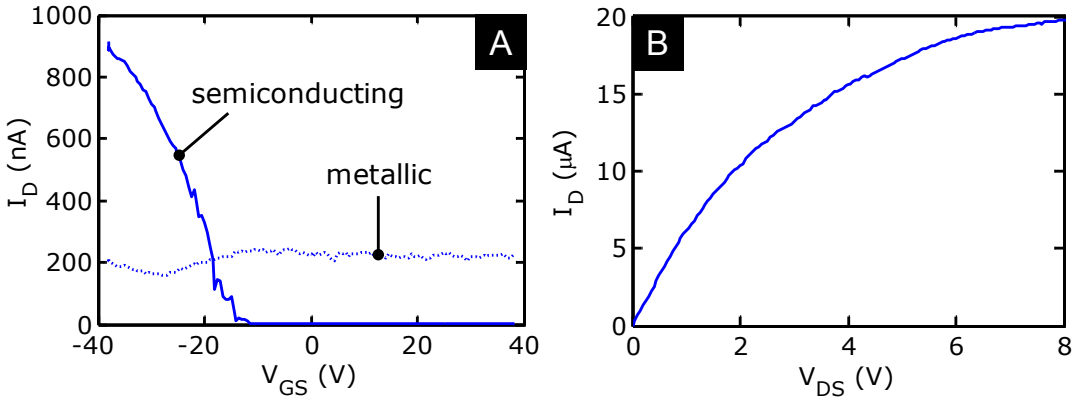

Fig. 1.5 (A) An I_D-V_{GS} sweep of a semiconducting and metallic CNT [47]. (B) A typical I_D-V_{DS} sweep of a CNT.

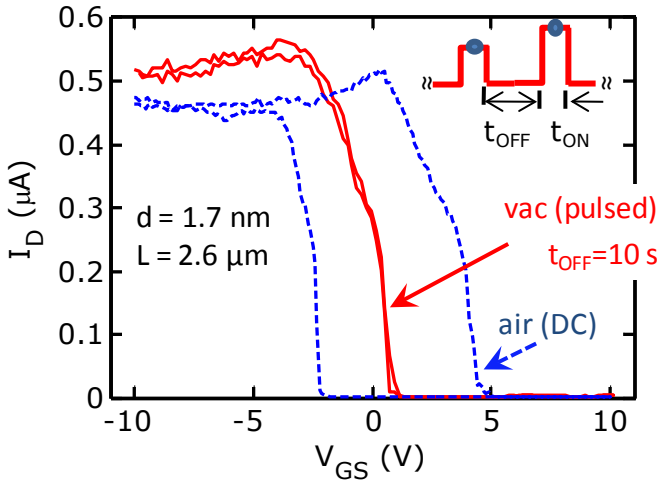

Fig. 1.6 Comparison between a DC sweep in air (dashed blue line) and a pulsed vacuum sweep (solid red line) of the same CNT. The inset is an illustration of the pulsing sequence for the gate bias. Measurements are made while the voltage is pulsed on and carriers are given time to escape traps during the off time.

hysteresis. The hysteresis is often attributed to charge trapping from the surrounding water molecules [48] and charge injection into the underlying dielectric [49]. This hysteresis if often not symmetrical and can thus cause a discrepancy in extracted values such as mobility. To remedy this problem, a pulsed measurement technique can be implemented [28]. The principle behind the pulsed technique is to turn off the bias periodically to give carriers sufficient time to escape traps. As a result the hysteresis becomes negligible as seen in Fig. 1.6.

It is important to characterize the dimensions of carbon materials since they impact physical and device properties such as band gap, mobility, thermal conductivity, thermal dissipation, and contact resistance. There exist many different methods by which these measurements can be made, all with their own set of advantages and disadvantages. Scanning electron microscopy (SEM), tunneling electron microscopy (TEM) [2], atomic force microscopy (AFM) [50, 51], and scanning tunneling microscopy (STM) [52, 53] extract dimensional information through imaging. Photoluminescence (PL) [25, 54], Raman spectroscopy [24, 55], and Rayleigh scattering [26, 56] are optical methods that can extract dimensional information by relating electrical and optical transitions with the dimensions. Following is a review of these techniques and how they are used to characterize carbon nanomaterials.

1.3.2 Nanoscale Imaging

The quickest imaging technique is SEM. The danger with SEM is that it is possible to induce defects with the electron beam. Therefore, it is important to use a low accelerating voltage (<1 kV). When imaging CNTs and GNRs on top of an oxide, they deflect electrons and charge up the underlying oxide, which causes the material to glow (as seen in Fig. 1.7A). Because of the glowing, the diameter or width of the material cannot be measured with SEM. Only the length can be accurately measured. Given the low accelerating voltages, it is often difficult to focus, and therefore resolution is sometimes limited to 100s of nanometers. If defects are of no concern then a higher accelerating voltage can be used to achieve better resolution. Given the speed of the measurement, the SEM is an invaluable tool for fabrication analysis (e.g. checking alignment). To obtain better resolution with electron microscopy, one can use TEM. However the drawback of TEM is that samples must be placed on very thin substrates, which requires a much larger degree of difficulty in fabrication.

Atomic force microscopy is a method by which both length and diameter information can be disseminated (see Fig. 1.7B). An AFM works by measuring the Van der Waals (vdW) interactions between a cantilevered tip and a surface. An AFM can be operated in two ways, contact mode and tapping mode. In the case of contact mode, the tip touches the surface gently while rastering the desired area. Changes in topography are detected as the tip runs over the surface. A laser that deflects off the back of the cantilever to a detec-

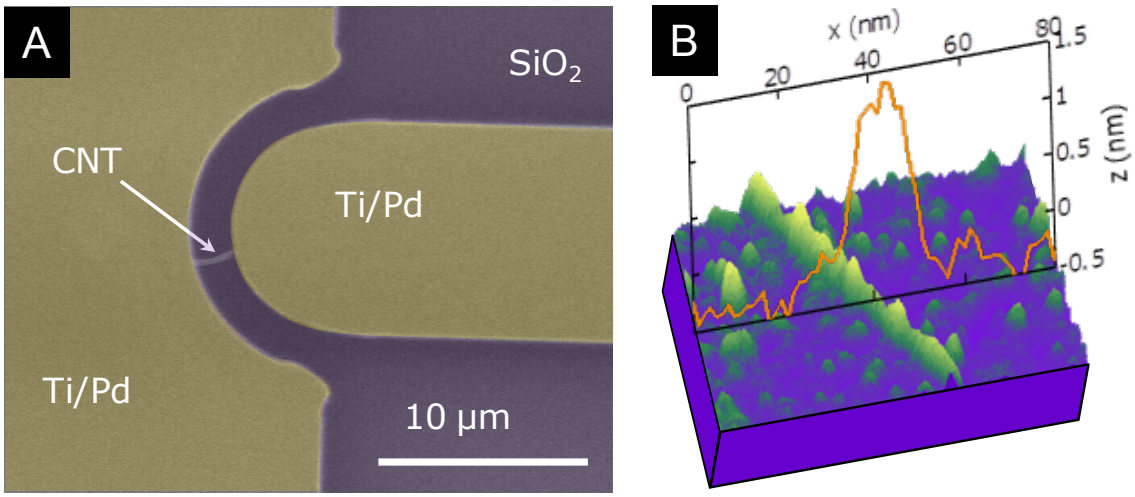

Fig. 1.7 (A) An SEM image of a CNT device. (B) Three-dimensional rendering of a CNT scanned with an AFM. On top is a cut plot of a cut across the CNT. All colors are false.

tor is used to measure this deflection. In tapping mode the tip oscillates over the surface. As the tip is raster scanned over the surface, changes in topography will cause changes in the oscillation amplitude, which are detected by the laser. For general imaging, tapping mode is used because contact mode scanning can lead to damaging and breaking of materials. In addition to imaging surfaces, the tip can be used for more than just force sensing. It can be electrically biased or Joule heated for use as a nanoprobe [51].

To obtain better resolution via scanning probe microscopy requires the use of STM. In STM, an atomically sharp tip is scanned over a surface while a tunneling current is monitored between the tip and the surface. As the distance between the surface and the tip decreases, the tunneling current through the vacuum potential will increase. This technique is a lot slower than AFM since the tip needs to be placed much closer to the surface and scans are usually limited to small areas. In addition, because it relies on monitoring the tunneling current, a conductive substrate is a requirement, making it non-ideal for scanning devices made on top of insulators. However, the payoff is the ability to obtain atomic resolution. Like an AFM, the tip can be used as a nanoprobe for other applications outside of just imaging a surface.

1.3.3 Optical Spectroscopy

The drawback of any scanning probe method is that they can be affected by tip-surface interactions [50]. In the case of single-walled CNTs, the vdW interactions are strong enough to deform the shape of the nanotube. How much the CNT deforms depends on the magnitude of the force being applied via the tip and the diameter of the CNT itself. These interactions, along with surface roughness, lead to a high level of uncertainty in measuring the diameter of the CNT. Optical methods can be used as alternatives for more accurate measurements. While these optical techniques do not have good spatial resolution (micron resolution), they rely on the relationship between optical transitions and the physical dimensions of the material to make accurate measurements.

Raman spectroscopy is one of the most used optical techniques to characterize carbon nanomaterials. The measurement is performed by illuminating a sample with a laser. The photons will undergo inelastic scattering with phonons at the surface of the material. These interactions cause the photons to re-emit at a different wavelength. The shift in the wavelength is known as the Raman shift. A detector counts photons reflected back from a

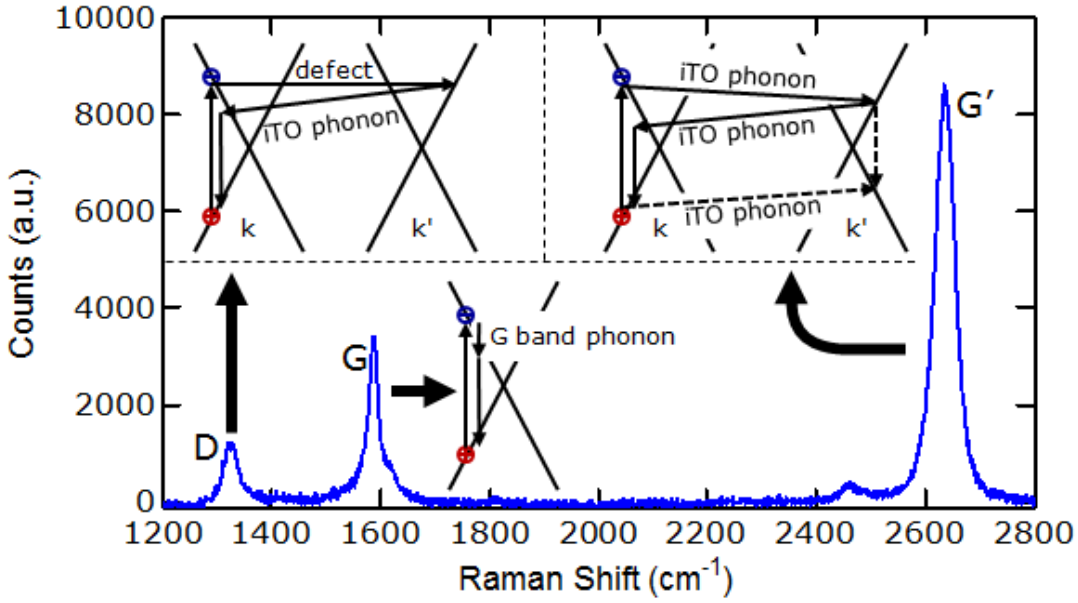

Fig. 1.8 (A) Raman spectrum for a monolayer of graphene (background subtracted). Scattering diagrams show the origin of each process. Dashed line for G' peak indicate the alternative triple resonant process. Spectrum is courtesy of Joshua D. Wood.

surface and plots this shift and peaks in the Raman spectrum indicate where these shifts occur. In graphitic materials there are three such shifts of note: the G-peak, the D-peak, and the G′ (also known as the 2D) peak (see Fig. 1.8). The G-peak refers to the sp^2 carbon-carbon bond and is present in all graphitic materials. The G-peak occurs approximately at 1600 cm^{-1}. The D-peak, appearing around 1300 cm^{-1}, is a double resonant (DR) process that is mediated through defects and the in-plane transverse optical (iTO) phonon. The G′-peak, at ~2600 cm^{-1}, is also a DR (and sometimes triple resonant) process, but scatters with the iTO phonon instead of defects. The scattering diagrams for these three processes are shown in Fig. 1.7 [57].

The G/G′ intensity ratio can be used to differentiate monolayer graphene from multilayered graphene. Graphene with a G/G′ ratio of ½ is considered to be monolayer. This works, however, only for Bernal stacked graphene layers. If graphene layers are randomly oriented, then the result will appear the same as monolayer graphene. One should also be careful when extending this method to counting layers of GNRs since the edges of GNRs will lower the intensity of the G-peak in addition to giving rise to a D-peak. Another technique specific for counting the number of graphene layers on SiO_2, would be to

compare the integrated G-peak intensity with the optical phonon peaks from Si [58]. This technique will work in the range where there are more than four layers.

The G-peak in CNTs is affected by the cylindrical structure of the CNT. This structure causes strain in the lattice and will cause the G-peak to split into a G^+ and G^- peak. Since the level of strain depends on the diameter, the amount of splitting in the G-peak will change with diameter. The smaller the diameter, the larger the splitting, because of the increased amount of strain. The G-band splitting can be given by the empirical formula $\Delta\omega_G = C/D^2$ cm^{-1} where D is the diameter in nm and C is a constant determined by the chirality (semiconducting or metallic) of the CNT ($C = 47.7$ cm^{-1}nm^2 for semiconducting CNTs, and $C = 79.5$ cm^{-1}nm^2 for metallic CNTs) [55, 59]. Unfortunately, the G-peak splitting and positioning can also be influenced by doping levels in metallic CNTs [60]. Therefore the G-peak splitting alone should never be used as a measure of the CNT's diameter.

A peak unique to CNTs is the radial breathing mode (RBM) which comes from the radial expansion of the tube [24]. These peaks, plotted in Fig. 1.9A, are generally very low (< 300cm^{-1}) and depend strongly on the optical transition energies between energy bands. The RBM also requires that the peak is resonant with the laser energy in order to excite the RBM. These optical transition energies depend on the chirality which determines the diameter. From the RBM peak the diameter can be determined from the following equation:

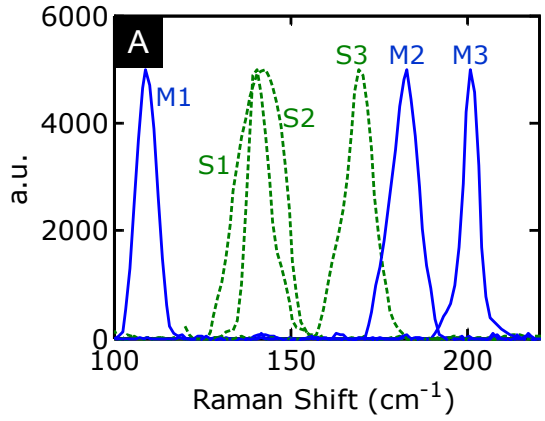

B

H_{AFM} (nm)	D_{RBM}(nm)	$D_{\Delta G}$(nm)	Chirality	S/M
1.2 ± 0.3	1.78	1.75	(19,5)	S1
1.4 ± 0.3	1.78	1.85	(23,0)	S2
1.7± 0.3	2.27	2.47	(18,18)	M1
1.6± 0.3	1.46	1.68	(19,0)	S3
1.2± 0.3	1.32	1.39	(15,3)	M2
1.2± 0.3	1.18	1.23	(15,0)	M3
1.2± 0.2*	1.12*	2.38*	(11,5)*	M*
1.3± 0.2*	1.37*	1.31*	(13,7)*	M*
1.5†	1.33†	1.35†	(NA)†	S†

Fig. 1.9 (A) RBM peaks for various CNTs. Metallic CNTs are indicated in solid blue and semiconducting CNTs are in dashed green. (B) Table comparing the height measured by AFM (H_{AFM}), RBM (D_{RBM}), G-peak splitting ($D_{\Delta G}$). The entries are from the plot on the left and from Refs. [61] and [62] marked by * and † respectively [50].

$$\omega_{RBM} = (A/D)\sqrt{1 + C_e D^2} \tag{1.1}$$

where C_e accounts for the environmental effects (e.g. substrate) [24, 55], A = 227 cm^{-1}nm is the proportionality constant from elasticity theory, D is in nm, and ω_{RBM} is in cm^{-1}. When combined with information from G-peak splitting and AFM measurements, the specific chiral indices can be assigned as shown in the table in Fig. 1.9B [50].

Other optical techniques include Rayleigh scattering and PL. Both of these techniques allow for chiral identification of CNTs. The drawback of photoluminescence is that it is restricted to semiconducting CNTs because the technique requires a bandgap. Rayleigh scattering and resonant Raman spectroscopy have the added benefit that they can be used to detect both metallic and semiconducting CNTs. While Rayleigh scattering events occur more frequently than Raman scattering events, environmental perturbations from the substrate significantly lower their signal to noise ratio. Originally to avoid this issue, CNTs were suspended over trenches, making sample preparation difficult [56]. Recently, a new technique which coats the CNTs with a material of similar refractive index to the substrate was used to increase the signal-to-noise ratio [26]. Cancelling out the substrate effect allows the acquisition times for scanning a CNT to be dramatically lower than for Raman spectroscopy.

1.4 References

[1] H. W. Kroto, J. R. Heath, S. C. Obrien, R. F. Curl, and R. E. Smalley, "C-60 - Buckminsterfullerene," *Nature,* vol. 318, pp. 162-163, 1985.

[2] S. Iijima, "Helical Microtubules of Graphitic Carbon," *Nature,* vol. 354, pp. 56-58, Nov 7 1991.

[3] K. S. Novoselov, A. K. Geim, S. V. Morozov, D. Jiang, Y. Zhang, S. V. Dubonos, I. V. Grigorieva, and A. A. Firsov, "Electric field effect in atomically thin carbon films," *Science,* vol. 306, pp. 666-669, Oct 22 2004.

[4] K. Ryu, A. Badmaev, C. Wang, A. Lin, N. Patil, L. Gomez, A. Kumar, S. Mitra, H. S. P. Wong, and C. W. Zhou, "CMOS-Analogous Wafer-Scale Nanotube-on-Insulator Approach for Submicrometer Devices and Integrated Circuits Using Aligned Nanotubes," *Nano Letters,* vol. 9, pp. 189-197, Jan 2009.

[5] P. G. Collins and P. Avouris, "Nanotubes for electronics," *Scientific American,* vol. 283, p. 62, Dec 2000.

[6] A. Cresti, N. Nemec, B. Biel, G. Niebler, F. Triozon, G. Cuniberti, and S. Roche, "Charge Transport in Disordered Graphene-Based Low Dimensional Materials," *Nano Research,* vol. 1, pp. 361-394, Nov 2008.

[7] F. Schwierz, "Graphene transistors," *Nature Nanotechnology,* vol. 5, pp. 487-496, Jul 2010.

[8] A. Behnam, A. S. Lyons, M.-H. Bae, E. K. Chow, S. Islam, C. M. Neumann, and E. Pop, "Transport in Nanoribbon Interconnects Obtained from Graphene Grown by Chemical Vapor Deposition," *Nano Letters,* Aug 2012.

[9] G. F. Close, S. Yasuda, B. Paul, S. Fujita, and H. S. P. Wong, "A 1 GHz integrated circuit with carbon nanotube interconnects and silicon transistors," *Nano Letters,* vol. 8, pp. 706-709, Feb 2008.

[10] R. H. Kim, M. H. Bae, D. G. Kim, H. Y. Cheng, B. H. Kim, D. H. Kim, M. Li, J. Wu, F. Du, H. S. Kim, S. Kim, D. Estrada, S. W. Hong, Y. G. Huang, E. Pop, and J. A. Rogers, "Stretchable, Transparent Graphene Interconnects for Arrays of Microscale Inorganic Light Emitting Diodes on Rubber Substrates," *Nano Letters,* vol. 11, pp. 3881-3886, Sep 2011.

[11] H. Li, C. Xu, N. Srivastava, and K. Banerjee, "Carbon Nanomaterials for Next-Generation Interconnects and Passives: Physics, Status, and Prospects," *IEEE Transactions on Electron Devices,* vol. 56, pp. 1799-1821, Sep 2009.

[12] F. Xiong, A. D. Liao, D. Estrada, and E. Pop, "Low-Power Switching of Phase-Change Materials with Carbon Nanotube Electrodes," *Science,* vol. 332, pp. 568-570, Apr 29 2011.

[13] J. Li, Y. J. Lu, Q. Ye, M. Cinke, J. Han, and M. Meyyappan, "Carbon nanotube sensors for gas and organic vapor detection," *Nano Letters,* vol. 3, pp. 929-933, Jul 2003.

[14] A. Salehi-Khojin, D. Estrada, K. Y. Lin, M. H. Bae, F. Xiong, E. Pop, and R. I. Masel, "Polycrystalline Graphene Ribbons as Chemiresistors," *Advanced Materials,* vol. 24, p. 53, Jan 2012.

[15] B. M. Venkatesan, D. Estrada, S. Banerjee, X. Z. Jin, V. E. Dorgan, M. H. Bae, N. R. Aluru, E. Pop, and R. Bashir, "Stacked Graphene-Al2O3 Nanopore Sensors for Sensitive Detection of DNA and DNA-Protein Complexes," *ACS Nano,* vol. 6, pp. 441-450, Jan 2012.

[16] F. Xiong, A. Liao, and E. Pop, "Inducing chalcogenide phase change with ultra-narrow carbon nanotube heaters," *Applied Physics Letters,* vol. 95, p. 243103, Dec 14 2009.

[17] K. Kordás, G. Toth, P. Moilanen, M. Kumpumaki, J. Vahakangas, A. Uusimaki, R. Vajtai, and P. M. Ajayan, "Chip cooling with integrated carbon nanotube microfin architectures," *Applied Physics Letters,* vol. 90, p. 123105, Mar 19 2007.

[18] R. Prasher, T. Tong, and A. Majumdar, "An acoustic and dimensional mismatch model for thermal boundary conductance between a vertical mesoscopic nanowire/nanotube and a bulk substrate," *Journal of Applied Physics,* vol. 102, p. 104312, Nov 2007.

[19] J. W. Mcclure, "Band Structure of Graphite and Dehaas-Vanalphen Effect," *Physical Review,* vol. 108, pp. 612-618, 1957.

[20] J. C. Slonczewski and P. R. Weiss, "Band Structure of Graphite," *Physical Review,* vol. 109, pp. 272-279, 1958.

[21] R. Saito, G. Dresselhaus, and M. S. Dresselhaus, *Physical Properties of Carbon Nanotubes*. London: Imperial College Press, 1998.

[22] R. Saito, G. Dresselhaus, and M. S. Dresselhaus, "Trigonal warping effect of carbon nanotubes," *Physical Review B,* vol. 61, pp. 2981-2990, Jan 15 2000.

[23] T. W. Odom, J. L. Huang, P. Kim, and C. M. Lieber, "Atomic structure and electronic properties of single-walled carbon nanotubes," *Nature,* vol. 391, pp. 62-64, Jan 1 1998.

[24] A. Jorio, R. Saito, J. H. Hafner, C. M. Lieber, M. Hunter, T. McClure, G. Dresselhaus, and M. S. Dresselhaus, "Structural (n, m) determination of isolated single-wall carbon nanotubes by resonant Raman scattering," *Physical Review Letters,* vol. 86, pp. 1118-1121, Feb 5 2001.

[25] S. M. Bachilo, M. S. Strano, C. Kittrell, R. H. Hauge, R. E. Smalley, and R. B. Weisman, "Structure-assigned optical spectra of single-walled carbon nanotubes," *Science,* vol. 298, pp. 2361-2366, Dec 20 2002.

[26] D. Y. Joh, L. H. Herman, S. Y. Ju, J. Kinder, M. A. Segal, J. N. Johnson, G. K. L. Chan, and J. Park, "On-Chip Rayleigh Imaging and Spectroscopy of Carbon Nanotubes," *Nano Letters,* vol. 11, pp. 1-7, Jan 2011.

[27] L. Y. Jiao, X. R. Wang, G. Diankov, H. L. Wang, and H. J. Dai, "Facile synthesis of high-quality graphene nanoribbons," *Nature Nanotechnology,* vol. 5, pp. 321-325, May 2010.

[28] D. Estrada, S. Dutta, A. Liao, and E. Pop, "Reduction of hysteresis for carbon nanotube mobility measurements using pulsed characterization," *Nanotechnology,* vol. 21, p. 085702, Feb 26 2010.

[29] A. D. Liao, J. Z. Wu, X. R. Wang, K. Tahy, D. Jena, H. J. Dai, and E. Pop, "Thermally Limited Current Carrying Ability of Graphene Nanoribbons," *Physical Review Letters,* vol. 106, p. 256801, Jun 20 2011.

[30] E. Pop, D. A. Mann, K. E. Goodson, and H. J. Dai, "Electrical and thermal transport in metallic single-wall carbon nanotubes on insulating substrates," *Journal of Applied Physics,* vol. 101, p. 093710, May 1 2007.

[31] V. Perebeinos, S. V. Rotkin, A. G. Petrov, and P. Avouris, "The Effects of Substrate Phonon Mode Scattering on Transport in Carbon Nanotubes," *Nano Letters,* vol. 9, pp. 312-316 2009.

[32] Z. Y. Ong and E. Pop, "Effect of substrate modes on thermal transport in supported graphene," *Physical Review B,* vol. 84, p. 075471, Aug 12 2011.

[33] Z. Y. Ong, E. Pop, and J. Shiomi, "Reduction of phonon lifetimes and thermal conductivity of a carbon nanotube on amorphous silica," *Physical Review B,* vol. 84, p. 165418, Oct 10 2011.

[34] J. H. Seol, I. Jo, A. L. Moore, L. Lindsay, Z. H. Aitken, M. T. Pettes, X. S. Li, Z. Yao, R. Huang, D. Broido, N. Mingo, R. S. Ruoff, and L. Shi, "Two-Dimensional Phonon Transport in Supported Graphene," *Science,* vol. 328, pp. 213-216, Apr 9 2010.

[35] W. Kim, A. Javey, R. Tu, J. Cao, Q. Wang, and H. J. Dai, "Electrical contacts to carbon nanotubes down to 1 nm in diameter," *Applied Physics Letters,* vol. 87, p. 173101, Oct 24 2005.

[36] D. Mann, A. Javey, J. Kong, Q. Wang, and H. J. Dai, "Ballistic transport in metallic nanotubes with reliable Pd ohmic contacts," *Nano Letters,* vol. 3, pp. 1541-1544, Nov 2003.

[37] T. Guo, P. Nikolaev, A. G. Rinzler, D. Tomanek, D. T. Colbert, and R. E. Smalley, "Self-Assembly of Tubular Fullerenes," *Journal of Physical Chemistry,* vol. 99, pp. 10694-10697, Jul 6 1995.

[38] M. José-Yacamán, M. Mikiyoshida, L. Rendon, and J. G. Santiesteban, "Catalytic Growth of Carbon Microtubules with Fullerene Structure (Applied Physics Letter, Vol 62, Pg 202, 1993)," *Applied Physics Letters,* vol. 62, pp. 657-659, Feb 8 1993.

[39] M. S. Arnold, A. A. Green, J. F. Hulvat, S. I. Stupp, and M. C. Hersam, "Sorting carbon nanotubes by electronic structure using density differentiation," *Nat Nano,* vol. 1, pp. 60-65, 2006.

[40] J. Kong, H. T. Soh, A. M. Cassell, C. F. Quate, and H. J. Dai, "Synthesis of individual single-walled carbon nanotubes on patterned silicon wafers," *Nature,* vol. 395, pp. 878-881, Oct 29 1998.

[41] L. X. Zheng, M. J. O'Connell, S. K. Doorn, X. Z. Liao, Y. H. Zhao, E. A. Akhadov, M. A. Hoffbauer, B. J. Roop, Q. X. Jia, R. C. Dye, D. E. Peterson, S. M. Huang, J. Liu, and Y. T. Zhu, "Ultralong single-wall carbon nanotubes," *Nature Materials,* vol. 3, pp. 673-676, Oct 2004.

[42] C. Kocabas, S. H. Hur, A. Gaur, M. A. Meitl, M. Shim, and J. A. Rogers, "Guided growth of large-scale, horizontally aligned arrays of single-walled carbon nanotubes and their use in thin-film transistors," *Small,* vol. 1, pp. 1110-1116, Nov 2005.

[43] G. Eres, A. A. Kinkhabwala, H. T. Cui, D. B. Geohegan, A. A. Puretzky, and D. H. Lowndes, "Molecular beam-controlled nucleation and growth of vertically aligned single-wall carbon nanotube arrays," *Journal of Physical Chemistry B,* vol. 109, pp. 16684-16694, Sep 8 2005.

[44] D. Jena, T. Fang, Q. Zhang, and H. L. Xing, "Zener tunneling in semiconducting nanotube and graphene nanoribbon p-n junctions," *Applied Physics Letters,* vol. 93, Sep 15 2008.

[45] M. Y. Han, J. C. Brant, and P. Kim, "Electron Transport in Disordered Graphene Nanoribbons," *Physical Review Letters,* vol. 104, p. 056801, Feb 5 2010.

[46] L. Y. Jiao, L. Zhang, X. R. Wang, G. Diankov, and H. J. Dai, "Narrow graphene nanoribbons from carbon nanotubes," *Nature,* vol. 458, pp. 877-880, Apr 16 2009.

[47] A. Liao, Y. Zhao, and E. Pop, "Avalanche-Induced Current Enhancement in Semiconducting Carbon Nanotubes," *Physical Review Letters,* vol. 101, p. 256804, Dec 19 2008.

[48] W. Kim, A. Javey, O. Vermesh, O. Wang, Y. M. Li, and H. J. Dai, "Hysteresis caused by water molecules in carbon nanotube field-effect transistors," *Nano Letters,* vol. 3, pp. 193-198, Feb 2003.

[49] S. Kar, A. Vijayaraghavan, C. Soldano, S. Talapatra, R. Vajtai, O. Nalamasu, and P. M. Ajayan, "Quantitative analysis of hysteresis in carbon nanotube field-effect devices," *Applied Physics Letters,* vol. 89, p. 132118, Sep 25 2006.

[50] R. Alizadegan, A. D. Liao, F. Xiong, E. Pop, and K. J. Hsia, "Effects of tip-nanotube interactions on atomic force microscopy imaging of carbon nanotubes," *Nano Research,* vol. 5, pp. 235-247, Apr 2012.

[51] J. Lee, A. Liao, E. Pop, and W. P. King, "Electrical and Thermal Coupling to a Single-Wall Carbon Nanotube Device Using an Electrothermal Nanoprobe," *Nano Letters,* vol. 9, pp. 1356-1361, Apr 2009.

[52] J. W. G. Wildoer, L. C. Venema, A. G. Rinzler, R. E. Smalley, and C. Dekker, "Electronic structure of atomically resolved carbon nanotubes," *Nature,* vol. 391, pp. 59-62, Jan 1 1998.

[53] K. A. Ritter and J. W. Lyding, "The influence of edge structure on the electronic properties of graphene quantum dots and nanoribbons," *Nature Materials,* vol. 8, pp. 235-242, Mar 2009.

[54] R. B. Weisman and S. M. Bachilo, "Dependence of optical transition energies on structure for single-walled carbon nanotubes in aqueous suspension: An empirical Kataura plot," *Nano Letters,* vol. 3, pp. 1235-1238, Sep 2003.

[55] A. Jorio, M. S. Dresselhaus, R. Saito, and G. Dresselhaus, *Raman Spectroscopy in Graphene Related Systems*. Weinheim, Germany: WILEY-VCH, 2011.

[56] M. Y. Sfeir, F. Wang, L. M. Huang, C. C. Chuang, J. Hone, S. P. O'Brien, T. F. Heinz, and L. E. Brus, "Probing electronic transitions in individual carbon nanotubes by Rayleigh scattering," *Science,* vol. 306, pp. 1540-1543, Nov 26 2004.

[57] L. M. Malard, M. A. Pimenta, G. Dresselhaus, and M. S. Dresselhaus, "Raman spectroscopy in graphene," *Physics Reports-Review Section of Physics Letters,* vol. 473, pp. 51-87, Apr 2009.

[58] Y. K. Koh, M. H. Bae, D. G. Cahill, and E. Pop, "Reliably Counting Atomic Planes of Few-Layer Graphene (n > 4)," *ACS Nano,* vol. 5, pp. 269-274, Jan 2011.

[59] A. Jorio, A. G. Souza, G. Dresselhaus, M. S. Dresselhaus, A. K. Swan, M. S. Unlu, B. B. Goldberg, M. A. Pimenta, J. H. Hafner, C. M. Lieber, and R. Saito, "G-band resonant Raman study of 62 isolated single-wall carbon nanotubes," *Physical Review B,* vol. 65, p. 155412, Apr 15 2002.

[60] H. Farhat, H. Son, G. G. Samsonidze, S. Reich, M. S. Dresselhaus, and J. Kong, "Phonon softening in individual metallic carbon nanotubes due to the Kohn anomaly," *Physical Review Letters,* vol. 99, p. 145506, Oct 5 2007.

[61] W. Lu, Y. Xiong, A. Hassanien, W. Zhao, M. Zheng, and L. W. Chen, "A Scanning Probe Microscopy Based Assay for Single-Walled Carbon Nanotube Metallicity," *Nano Letters,* vol. 9, pp. 1668-1672, Apr 2009.

[62] S. B. Cronin, A. K. Swan, M. S. Unlu, B. B. Goldberg, M. S. Dresselhaus, and M. Tinkham, "Measuring the uniaxial strain of individual single-wall carbon nanotubes: Resonance Raman spectra of atomic-force-microscope modified single-wall nanotubes," *Physical Review Letters,* vol. 93, p. 167401, Oct 15 2004.

CHAPTER 2

TRANSPORT AND ENERGY DISSIPATION IN NANOSCALE DEVICES

2.1 Introduction

A material's electrical and thermal conductivity are strongly affected both by their surrounding environment and physical dimensions. The latter has played a key role in electronic devices as they have been aggressively scaled well below 100 nm. For instance, surfaces and interfaces begin to play a bigger role in restricting current flow. Furthermore, each added interface limits the number of pathways which heat has to escape. As a result local hotspots may form, leading to thermal runaway. Heating can degrade performance and, even worse, cause physical failure in devices. It is important to understand the interplay between electrons and phonons within a material to understand energy dissipation. However, to get the whole power dissipation picture, transmission and scattering at boundaries and interfaces should be included as well. As a result of studying dissipation through surfaces, boundaries, and interfaces, a new engineering design space is created since these can all be controlled to a degree through fabrication. For example, changing the material or geometry of an inactive material (e.g. a gate dielectric) may have a significant influence on the device behavior, without even altering the active materials (e.g. interconnects or channel in a transistor).

2.2 Transport Regimes

It becomes harder to apply classical concepts of conduction as device dimensions decrease. At approximately 100 nm, even simple equations such as Ohm's law require revision. How a material conducts can be categorized into three transport regimes depending on the size of the system in relation to the mean free path (MFP) and wavelength of the transport carrier (electron or phonon) [1, 2]. The MFP is an average of the distance a carrier travels before scattering. The size of the system in relation to the carrier wavelength will determine the extent of quantum confinement. These three transport regimes going from smallest to largest dimensions are ballistic, quasi-ballistic, and diffusive transport

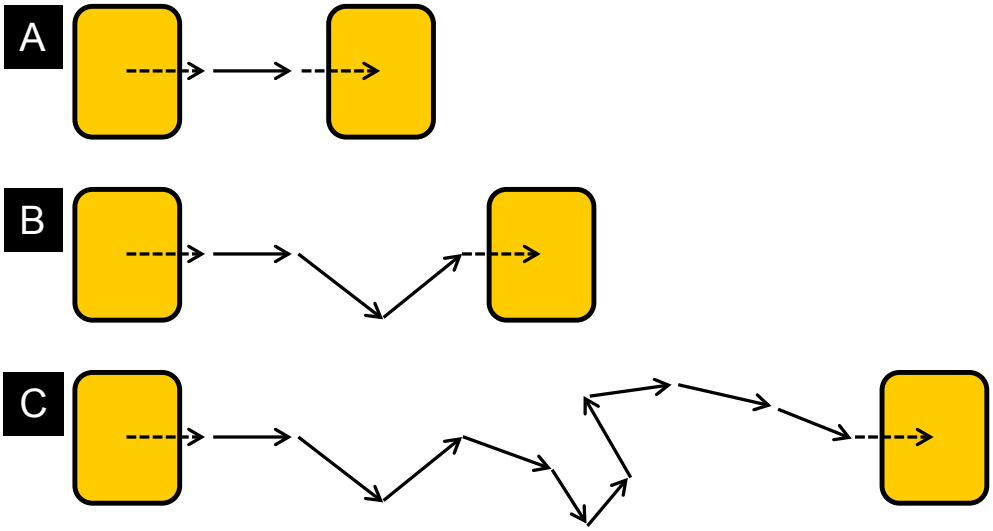

Fig. 2.1 Illustration of scattering in different transport regimes between two contacts: (A) ballistic (B) quasi-ballistic (C) diffusive.

(see Fig. 2.1). Because of the differences in conduction, the way power dissipates at these regimes will also be affected [3].

2.2.1 Ballistic Transport

When the dimensions of the system are smaller than the carrier wavelength and the MFP, transport is considered to be ballistic. If the material is free of defects, then there will be no scattering in the channel. Thus, the conduction limit of carriers will be determined by the contact resistance. These limits are known as the quantum conduction limits and represent the highest achievable values of conductance. These limits can be calculated using Landauer-Buttiker Formalism [4]. The current density flow from one terminal to another is written as

$$J = \int xD(k)f(k)v(k)\alpha(k)dk \tag{2.1}$$

where $D(k)$ is the density of states (DOS), $f(k)$ is the distributions function, $v(k)$ is the group velocity, $\alpha(k)$ is the transmission coefficient, and x is the medium being transported by the carrier. In the case of electrons, D will be the electron DOS, f will be the Fermi-Dirac distribution, and x will be elemental charge ($\pm e$). In addition, spin degeneracy must be considered by multiplying equation (2.1) by two. In the case of phonons, D will be the phonon DOS, f will be the Bose-Einstein distribution, and x will be energy ($E = \hbar\omega$). The transmission coefficient is equal to one since there are no scattering events. The quantum

conductance for electrons turns out to be $G_{q,e} = Me^2/h$, where M represents the number of transport modes and h is Planck's constant. The thermal quantum conductance for phonons turns out to be $\pi^2 k_B T/3h$, where k_B is the Boltzmann constant and T is the temperature.

Ballistic transport has been observed experimentally for both electron and phonon transport. Special quantum point contact devices were fabricated to measure the electronic quantum conductance at low temperatures [5]. By performing measurements at cryogenic temperatures, the MFP is increased, allowing ballistic transport between the contacts. In order to measure ballistic conduction at room temperature, carbon nanotubes (CNTs) have been used because of their long MFP [1, 2, 6]. Measurement of thermal ballistic conduction has proven to be more difficult. All previous measurements of quantum thermal conductance have been made by suspending 1-D constrictions to thermally isolate the transport channel [7-9].

The difficulty across all these experiments remains at the contacts. While the conducting channel might be ballistic, there is always a drop in conduction at the contacts. This means that the power dissipated in a ballistic device will be limited at the contacts. How much power is dissipated at these contacts depends on the ohmic or Schottky nature of the contact. Schottky barrirer (SB) contacts very strongly limit the conduction through a channel [10, 11]. Ohmic contacts allow for much higher transmission into the channel [12]. Therefore, power dissipation will be much higher at SB contacts.

2.2.2 Quasi-Ballistic Transport

When the dimensions of the system are on the same order of the MFP, but larger than the carrier wavelength, then transport is considered to be quasi-ballistic. Here a significant number of scattering events occur to raise the resistance in the channel. Now both the contacts, quantum limited resistance, and channel resistance must be taken into account. To model quasi-ballistic transport, the Boltzmann transport equation (BTE) or Monte Carlo (MC) simulations may be employed [13]. The BTE is a statistical treatment of carriers. It keeps track of how a distribution of carriers $f(\mathbf{r}, \mathbf{k}, t)$ evolves in space, momentum, and time within a small volume $d\mathbf{r}d\mathbf{k}$. Because it assumes that particles have a specific space and momentum at a specific time, it violates the uncertainty principle.

Therefore the BTE should not be used to model quantized systems (i.e. the ballistic regime). The BTE is written as:

$$\frac{\partial f}{\partial t} + v\nabla_{\mathrm{r}} f + F\nabla_{\mathrm{k}} f = \left.\frac{\partial f}{\partial t}\right|_{collision} \tag{2.2}$$

where v is the velocity and F is the force acting on the particle (e.g. an electric field upon an electron). The first term moving from left to right represents the time rate of change in the distribution function. The second term represents the change in the distribution due to the motion of particles in free space. The third term accounts for the change in the distribution caused by an external force altering the momentum of particles. Finally, the term on the right takes scattering into account. This equation cannot be solved analytically but can be solved numerically. One such numerical method is MC where the distributions can be calculated by finding the probability that a carrier is scattered during a certain time interval.

As mentioned above, the contact resistance and the channel resistance both contribute similarly in a quasi-ballistic system. This can be observed experimentally when comparing the conduction between CNTs that are hundreds of nanometers long to ones that are tens of nanometers long [1, 2]. Previous work has shown that the channel conductance can be modeled by plugging a transmission coefficient, $\alpha = \lambda/(L+\lambda)$, where λ is the MFP and L is the channel length, into equation (2.1) [14, 15]. The quality of the contact will still have a significant impact in limiting the power dissipation within the channel [16]. The overall resistance of a two terminal device will have the following form [14]:

$$R(V,T) = R_C + \frac{h}{Mq^2}\left\{1 + \int_{-L/2}^{L/2} \frac{dx}{\lambda[V, T(x)]}\right\} \tag{2.3}$$

where R_C represents the overall contact resistance and the integral is taken along the length of the channel (x direction).

2.2.3 Diffusive Transport

When the dimensions of the system are much larger than the MFP, then transport is considered to be diffusive. To model diffusive transport, continuum models are used, such as the drift-diffusion equation for electronic current and Fourier's law for heat flow. The approximation that is made in diffusive models is that there are so many scattering

events that the frequency at which they occur can be well described by a net average. As a result, diffusive models can be derived directly from the BTE using the relaxation time approximation. In this case equation (2.2) becomes

$$\frac{\partial f}{\partial t} + v\nabla_{\mathrm{r}} f + F\nabla_{\mathrm{k}} f = \frac{f_0 - f}{\tau} \tag{2.4}$$

where τ is the average time between scattering events and f_0 is the equilibrium distribution. If the system is in equilibrium, then the first term on the left-hand side can be ignored. For electrons in a semiconductor, assuming a parabolic band structure leads to the well known semiconductor drift-diffusion equation. For phonons, assuming no external forces eliminates the third term on the left side of equation (2.4) ultimately recovers Fourier's equation.

A common attribute in all diffusive models is the negligence of the contact resistance. Since there are so many scattering events, the channel resistance will dwarf the contact resistance. Therefore, the first term in equation (2.3) can now be dropped when calculating the overall resistance in a two-terminal device. The total power dissipated in a diffusively conducting device can be calculated using Ohm's law, $P = I^2R$.

2.3 Scattering

In the previous section, the MFP was shown to have a direct impact on the transport and power dissipation in a material. The MFP is determined by the average length the carrier travels before undergoing a scattering event. These events include scattering with impurities, defects, surface and edges, electrons, and phonons. The frequency that these events occur will vary, which will cause the MFP to vary. A simple approximation to average the effects of all the scattering mechanisms is to add them like parallel resistors. This is known as Matthiessen's rule and is written as follows:

$$\frac{1}{\lambda} = \sum_i \frac{1}{\lambda_i} \tag{2.5}$$

where λ_i represents the MFP of a different scattering mechanism. The assumption in equation (2.5) is that the scattering rates for each independent mechanism have the same energy dependence [17]. This is actually not often the case and there are certainly instances where this approximation is not valid. For example, Matthiessen's rule breaks

down when considering systems such as thin films and nanowires where surface scattering contributes strongly [18, 19]. Nevertheless, it is a helpful tool because it is easier to consider different scattering mechanisms separately.

Impurity, defect, grain boundary, and surface scattering depend on the physical structure of the material. These scattering processes are typically elastic in nature (i.e. momentum is conserved). The MFP in this case depends on how rough the surface is, how heavily doped it is, how defective it is, and what the average grain sizes are. Since these processes depend on the physical structure of the material, there is little temperature dependence on the scattering rates. Their MFP can be estimated as the average distance between each feature. In nanoscale systems, these mechanisms have a much stronger impact and cause lower conduction properties than bulk systems [20-26].

Another scattering mechanism is between electrons and phonons. Electrons can either gain energy from absorbing present phonons or lose energy through emitting phonons. There are two types of phonons for electrons to scatter with, acoustic (AC) and optical (OP) [13]. Acoustic phonons are low energy phonons which are primarily responsible for transporting heat in the lattice. They have much higher group velocity, which is given as the derivative with respect to wave-vector in the dispersion, than optical phonons. This is illustrated through a schematic of phonon dispersion for a diatomic chain of atoms in Fig. 2.2. The typical MFP of an acoustic phonon is usually in the hundreds of nanometers range.

Optical phonons are much higher in energy and thus are only considered to be inter-

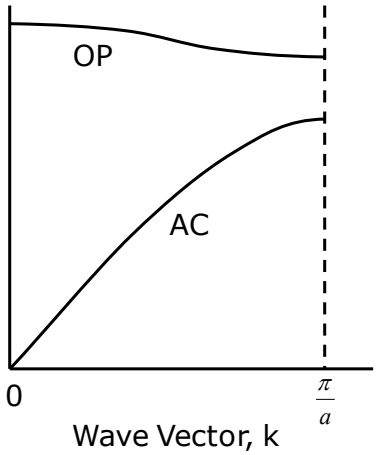

Fig. 2.2 Generic phonon dispersion showing low energy acoustic phonons and higher energy optical phonons.

acting with carriers of high energy. These phonons have a very small MFP, typically around tens of nanometers. Thus, they have a significant impact in lowering the conduction in a device. Optical phonons do not contribute directly very much to heat transport because they possess low group velocity, as evidenced by the phonon dispersion (see Fig. 2.2). Instead they must dissipate energy into acoustic phonons in order for their energy to be transferred through the lattice [27]. During this process, energy carried by electrons will ultimately be dissipated through heat. This is known as Joule self-heating.

2.4 Energy Dissipation

As the strength of the accelerating field increases, carriers gain more energy. This increase in energy also raises the OP scattering rate. As more OPs are generated, they will continue to dissipate energy into the lattice and thus generate a significant amount of heat (i.e. Joule heating). As the temperature increases, phonon occupation will further increase, thus increasing the probability of scattering. The ultimate result is a decrease in the OP emission MFP. In CNTs this has been shown to be the primary scattering mechanism at high bias [27, 28] and is thought to limit current carrying capacity [29]. Even in more mature technology such as silicon-on insulator (SOI) transistors, Joule heat generation has been shown to be problematic [30]. Therefore, it would be beneficial to maximize energy dissipation to retard heat generation. This can be done by choosing and engineering the environment around the channel. This section will review the process by which heat flows across interfaces.

2.4.1 Phonon Transport Across Interfaces

As mentioned at the beginning of the chapter, an increasing variety of materials continue to be integrated into devices, which cause more interfaces to be formed. While these interfaces usually serve an important role electronically, such as electrical insulation in ultra thin body silicon or silicon on insulator, they interfere with heat transfer as they introduce additional thermal resistances that did not previously exist [30]. If thermal resistances become too high, then heat can get trapped, degrading device performance and posing a severe reliability risk.

To characterize heat flow across interfaces, experiments are set up to solve the heat diffusion equation where the thermal boundary resistance or conductance (TBR or TBC)

across an interface is the independent variable. The heat diffusion equation is defined generally by

$$\nabla(\kappa\nabla T)+q'''-g(T-T_0)=\rho C_p\frac{\partial T}{\partial t} \tag{2.6}$$

where κ is the thermal conductivity of the medium, q''' is the volumetric heat generation, T is temperature, t is time, ρ is the density of the medium, g is the TBC, and C_p is the heat capacity at constant pressure. The TBC includes all interfaces and heat flow out of the channel. The power that is generated is done through Joule self-heating in a device (e.g. wire or transistor). By correlating the input power with the known temperature the TBC can be extracted [31-34]. When the channel is one-dimensional, as is the case for a CNT, a resistance associated with the spreading heat (part of R_{OX} in Fig 2.2) into other materials must be taken account. This can be done by using a shape factor to adjust the thermal conductivity. Of course a device is not required to measure heat transport across interfaces as stacks of films can be used in the three-omega [35] or pump-probe laser [36-38] measurement.

There are several ways of modeling the TBC. One way of modeling TBR is through molecular dynamics (MD) simulations [39]. MD simulations employ classical calculations to study the motion and energy of interacting atoms in a system. Because it is a classical simulation, MD can over-predict the heat capacity when the Debye temperature is much higher than room temperature. Also, the results are very dependent upon what inter-atomic potential is input in the simulation. Finally, because the computational burden grows as more atoms are added, MD is generally limited to nanometer size systems.

Simpler analytical models exist for calculating TBR. While these are not always accurate, they are much faster than MD simulations and can still offer some physical insights. To calculate TBC, the heat current flowing from material one to material two is given as

$$\dot{Q}_{1\to 2}(T)=\frac{1}{2}\sum_j\int_0^{\pi/2}\int_0^{\omega_1^{\max}} f_{1,j}^{BE}(\omega,T)D_{1,j}(\omega)\hbar\omega v_{1,j}\alpha(\theta,j,\omega)\cos\theta\sin\theta d\theta d\omega \tag{2.7}$$

where f^{BE} is the Bose-Einstein distribution, D is the phonon density of states, j refers to the each phonon mode, α is the transmission coefficient, and θ is the angle of incidence as diagramed in Fig. 2.3A. The thermal boundary conductivity is thus calculated as

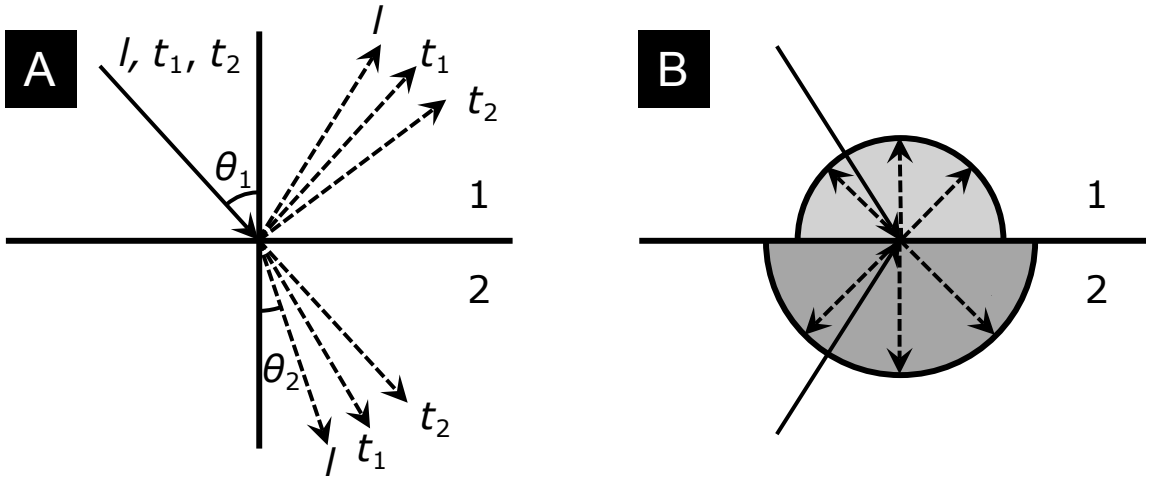

Fig. 2.3 (A) Illustration of the AMM. An incident phonon (solid arrow) will reflect or transmit (dashed arrows) into either longitudinal (l) or transverse (t_1, t_2) modes. (B) In the case of the DMM, incident phonons can scatter diffusely into either material as long as there are states available.

$$h = \frac{1}{A}\frac{d\dot{Q}_{1\to 2}}{dT} \tag{2.8}$$

where A refers to area of the interface.

There are two prevalent models for calculating the transmission coefficient, each rooted in different physical assumptions. These are the acoustic mismatch model (AMM) and the diffuse mismatch model (DMM) [40]. The AMM considers the wavelength and direction of the incoming phonon. The assumption is that the interface is a flat plane and that there is no lattice such that the phonons move through a continuum. An incoming phonon can reflect or transmit, and can change polarization as diagramed in Fig. 2.3A. The transmission coefficient can be calculated similarly to Fresnel equations.

The DMM makes the assumption that any incoming phonon can be reflected or transmitted based on the available states, as shown in Fig. 2.3B. Each incoming phonon loses memory of which material it comes from since scattering at the interface is diffuse. Thus the only requirement for transmission is that there is a state available. Therefore, transmission is ultimately limited by the mismatch in the phonon density of states (PDOS). Thus the transmission coefficient no longer depends upon the angle of incidence and we may take it out of the angle integral in equation (2.7). From a detailed balance argument, the transmission coefficient is given as

$$\alpha(\omega) = \frac{\sum_{j} v_{3-i,j} f^{BE}_{3-i,j}(\omega, T) D_{3-i,j}(\omega)}{\sum_{i,j} v_{i,j} f^{BE}_{i,j}(\omega, T) D_{i,j}(\omega)} \tag{2.9}$$

where *i* refers to the material (i.e. material 1 or 2).

2.4.2 Remote Phonon Interactions

An additional pathway for power dissipation is possible through coupling between carriers in the channel and the surface polar phonon (SPP) modes from a dielectric [41-43]. These surface modes come about from the dipole nature of atoms in materials. They are present in many oxides. These polar modes create an evanescent field which can interact with carriers. So as long as carriers are physically close to the surface, there is a chance that these near field interactions will cause energy to be exchanged with SPPs. Not all modes will interact strongly with carriers; therefore it is good enough to consider the dominant mode [44]. Since these interactions are mediated by evanescent fields, the strength of the interaction is strongly affected by the distance between the carrier and the surface of the substrate. Changes in separation from surface roughness are enough to cause significant variance in strength. While this mechanism does provide an additional pathway for heat dissipation, it also introduces another scattering mechanism. Therefore this near field effect does not always improve conduction.

2.5 High-Field Transport

As the field is increased, several other mechanisms will start to take effect. Higher subbands will start to come into play. For semiconductors, the band bending will thin down the energy barrier between valence and conduction band. Schottky contacts may start to become more transparent for tunneling. In extreme cases, atoms themselves start to drift. Some of these mechanisms will lower conduction, but some will increase it. In the following section, a review is provided for mechanisms that serve to increase conduction.

2.5.1 Impact Ionization

Sometimes carriers can gain so much kinetic energy that their temperature, given by $k_B T_e$, can be much higher than the actual lattice temperature. These "hot" carriers can de-

grade conductance and decrease reliability. However, hot carriers can also lead to impact ionization (II), which increases conduction. Impact ionization is considered to be a soft (reversible) breakdown. It causes the current to increase rapidly through carrier multiplication. Impact ionization occurs when carriers gain enough energy to create an electron-hole pair (EHP), as diagramed in Fig. 2.4A. The newly created carriers then continue to gain energy and may undergo II themselves, creating an avalanche current. While momentum should be conserved, the threshold field for II, E_{TH}, predominantly depends on the bandgap. Figure 2.4B shows how as the band-gap decreases, E_{TH} does as well. The probability for undergoing II depends on the MFP as well. If the carrier undergoes a scattering event, then it will lose energy and will thus be unable to undergo II. Carriers must gain sufficient energy over a distance that is comparable to the scattering MFP. This can be done by increasing the field, although doing so may give rise to other high-field effects or could cause irreversible breakdown through Joule heating before the conditions for II are satisfied. Assuming that no other high-field effects are significant, the dependence between II and scattering can be exploited to extract the MFP [45].

In general II is seen as a reliability concern as it can cause currents to increase uncontrollably, inducing irreversible breakdown. However in recent years there has been an attempt to make a device that takes advantage of II. This device is known as the I-MOS (impact ionization metal-oxide-semiconductor transistor). It aims to lower the

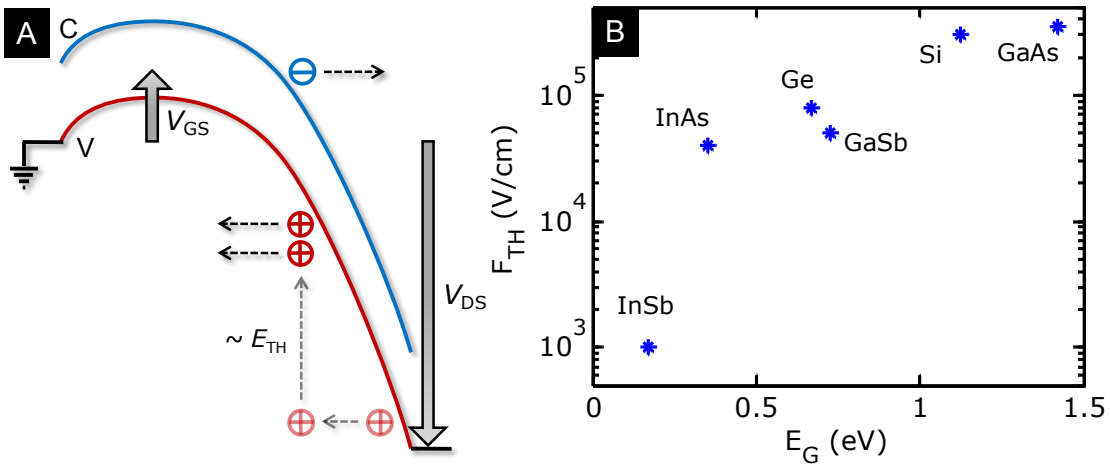

Fig. 2.4(A) Schematic band diagram of a CNT undergoing II shown for hole transport [45]. (B) II threshold field as a function of the bandgap of various materials.

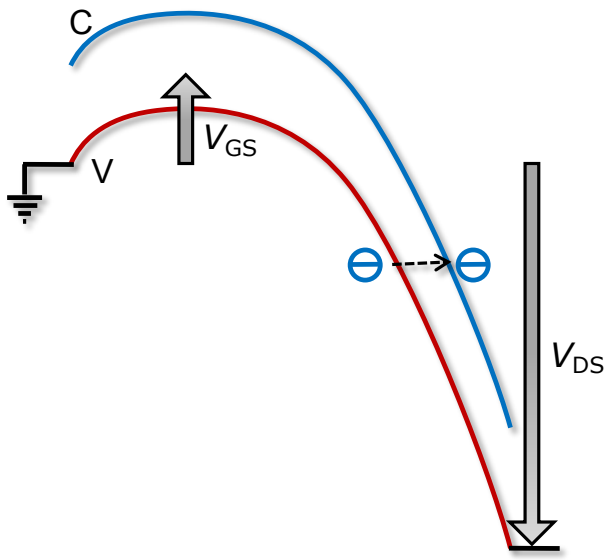

Fig. 2.5 Schematic band-diagram of the Zener band-to-band tunneling process. An electron tunnels from conduction band to valence band.

subthreshold slope in transistors below the thermal limit of ~60 mV/dec by using the avalanche current to switch the transistor on and off. While subthreshold switching < 60 mV/dec has been achieved, it was done at impractically high biases [46].

2.5.2 Zener Tunneling

Zener tunneling (ZT), also known as band-to-band tunneling, occurs when a high field induces band-bending such that the barrier between the conduction and valence band is thin enough to allow carriers to tunnel between the two bands. This process is diagramed in Fig. 2.5 showing an electron in the valence band tunneling through to the conduction band. Like II, the onset of ZT is marked by an increase in current. The tunneling current depends on the strength of the applied field and the magnitude of the bandgap. For a semiconductor with parabolic bands, the tunneling probability is given as

$$P = \exp\left(-\frac{4\sqrt{2m}}{3eF\hbar}E_G^{3/2}\right) \tag{2.10}$$

where m is the carrier mass, F is the field, and E_G is the energy gap. If instead the bands are hyperbolic, like in the case of a CNT or GNR, the equation is [47]:

$$P = \exp\left(-\frac{\pi E_G^2}{4\hbar v_F eF}\right) \tag{2.11}$$

Just as the I-MOS has been proposed as a new switch, so have devices based on ZT, called tunneling field effect transistors (TFETs). The TFET instead takes advantage of band offset created by a difference in doping to promote ZT [48]. Using the ZT, like II, would allow devices to be built with subthreshold swings of < 60 mV/dec. It should be noted that one of the first experimental observations of sub-60 mV/dec switching was done with a CNT [49].

2.6 References

[1] A. Javey, J. Guo, M. Paulsson, Q. Wang, D. Mann, M. Lundstrom, and H. J. Dai, "High-field quasiballistic transport in short carbon nanotubes," *Physical Review Letters,* vol. 92, p. 106804, 2004.

[2] A. D. Franklin and Z. H. Chen, "Length scaling of carbon nanotube transistors," *Nature Nanotechnology,* vol. 5, pp. 858-862, Dec 2010.

[3] E. Pop, "Energy Dissipation and Transport in Nanoscale Devices," *Nano Research,* vol. 3, pp. 147-169, Mar 2010.

[4] S. Datta, *Electronic Transport in Mesoscopic Systems* Cambridge, United Kingdom: Cambridge University Press, 1997.

[5] B. J. Van Wees, H. Van Houten, C. W. J. Beenakker, J. G. Williamson, L. P. Kouwenhoven, D. Van der Marel, and C. T. Foxon, "Quantized Conductance of Point Contacts in a Two-Dimensional Electron-Gas," *Physical Review Letters,* vol. 60, pp. 848-850, Feb 29 1988.

[6] A. Javey, J. Guo, Q. Wang, M. Lundstrom, and H. J. Dai, "Ballistic carbon nanotube field-effect transistors," *Nature,* vol. 424, pp. 654-657, Aug 7 2003.

[7] K. Schwab, E. A. Henriksen, J. M. Worlock, and M. L. Roukes, "Measurement of the quantum of thermal conductance," *Nature,* vol. 404, pp. 974-977, Apr 27 2000.

[8] H. Y. Chiu, V. V. Deshpande, H. W. C. Postma, C. N. Lau, C. Miko, L. Forro, and M. Bockrath, "Ballistic phonon thermal transport in multiwalled carbon nanotubes," *Physical Review Letters,* vol. 95, p. 226101, Nov 25 2005.

[9] E. Pop, D. Mann, Q. Wang, K. Goodson, and H. J. Dai, "Thermal conductance of an individual single-wall carbon nanotube above room temperature," *Nano Letters,* vol. 6, pp. 96-100, Jan 2006.

[10] J. Appenzeller, J. Knoch, V. Derycke, R. Martel, S. Wind, and P. Avouris, "Field-modulated carrier transport in carbon nanotube transistors," *Physical Review Letters,* vol. 89, p. 126801, Sep 16 2002.

[11] S. Heinze, J. Tersoff, R. Martel, V. Derycke, J. Appenzeller, and P. Avouris, "Carbon nanotubes as Schottky barrier transistors," *Physical Review Letters,* vol. 89, p. 106801, Sep 2 2002.

[12] D. Mann, A. Javey, J. Kong, Q. Wang, and H. J. Dai, "Ballistic transport in metallic nanotubes with reliable Pd ohmic contacts," *Nano Letters,* vol. 3, pp. 1541-1544, Nov 2003.

[13] K. Hess, *Advanced Theory of Semiconductor Devices*. Piscataway, NJ: IEEE Press, 2000.

[14] E. Pop, D. A. Mann, K. E. Goodson, and H. J. Dai, "Electrical and thermal transport in metallic single-wall carbon nanotubes on insulating substrates," *Journal of Applied Physics,* vol. 101, p. 093710, May 1 2007.

[15] Y. Zhao, A. Liao, and E. Pop, "Multiband Mobility in Semiconducting Carbon Nanotubes," *IEEE Electron Device Letters,* vol. 30, pp. 1078-1080, Oct 2009.

[16] Y. Ouyang and J. Guo, "Heat dissipation in carbon nanotube transistors," *Applied Physics Letters,* vol. 89, p. 183122, Oct 30 2006.

[17] M. Lundstrom, *Fundamentals of Carrier Transport*, 2nd ed. Cambridge: Cambridge University Press, 2000.

[18] B. Feldman, R. Deng, and S. T. Dunham, "Dependence of resistivity on surface profile in nanoscale metal films and wires," *Journal of Applied Physics,* vol. 103, Jun 1 2008.

[19] R. C. Munoz, C. Arenas, G. Kremer, and L. Moraga, "Surface-induced resistivity of $CoSi_2$ films and violations of Mathiessen's rule," *Journal of Physics-Condensed Matter,* vol. 15, pp. L177-L184, Mar 19 2003.

[20] A. Behnam, A. S. Lyons, M.-H. Bae, E. K. Chow, S. Islam, C. M. Neumann, and E. Pop, "Transport in Nanoribbon Interconnects Obtained from Graphene Grown by Chemical Vapor Deposition," *Nano Letters,* 2012/08/17 2012.

[21] A. I. Hochbaum, R. K. Chen, R. D. Delgado, W. J. Liang, E. C. Garnett, M. Najarian, A. Majumdar, and P. D. Yang, "Enhanced thermoelectric performance of rough silicon nanowires," *Nature,* vol. 451, pp. 163-U5, Jan 10 2008.

[22] A. Cresti, N. Nemec, B. Biel, G. Niebler, F. Triozon, G. Cuniberti, and S. Roche, "Charge Transport in Disordered Graphene-Based Low Dimensional Materials," *Nano Research,* vol. 1, pp. 361-394, Nov 2008.

[23] W. J. Evans, L. Hu, and P. Keblinski, "Thermal conductivity of graphene ribbons from equilibrium molecular dynamics: Effect of ribbon width, edge roughness, and hydrogen termination," *Applied Physics Letters,* vol. 96, p. 203112, May 17 2010.

[24] M. Y. Han, J. C. Brant, and P. Kim, "Electron Transport in Disordered Graphene Nanoribbons," *Physical Review Letters,* vol. 104, p. 056801, Feb 5 2010.

[25] A. V. Savin, Y. S. Kivshar, and B. Hu, "Suppression of thermal conductivity in graphene nanoribbons with rough edges," *Physical Review B,* vol. 82, Nov 10 2010.

[26] A. I. Boukai, Y. Bunimovich, J. Tahir-Kheli, J. K. Yu, W. A. Goddard, and J. R. Heath, "Silicon nanowires as efficient thermoelectric materials," *Nature,* vol. 451, pp. 168-171, Jan 10 2008.

[27] E. Pop, D. Mann, J. Cao, Q. Wang, K. Goodson, and H. J. Dai, "Negative differential conductance and hot phonons in suspended nanotube molecular wires," *Physical Review Letters,* vol. 95, p. 155505, Oct 7 2005.

[28] M. A. Kuroda, A. Cangellaris, and J. P. Leburton, "Nonlinear transport and heat dissipation in metallic carbon nanotubes," *Physical Review Letters,* vol. 95, p. 266803, Dec 31 2005.

[29] Z. Yao, C. L. Kane, and C. Dekker, "High-field electrical transport in single-wall carbon nanotubes," *Physical Review Letters,* vol. 84, pp. 2941-2944, Mar 27 2000.

[30] L. T. Su, J. E. Chung, D. A. Antoniadis, K. E. Goodson, and M. I. Flik, "Measurement and Modeling of Self-Heating in SOI nMOSFET's," *IEEE Transactions on Electron Devices,* vol. 41, pp. 69-75, Jan 1994.

[31] A. Liao, R. Alizadegan, Z. Y. Ong, S. Dutta, F. Xiong, K. J. Hsia, and E. Pop, "Thermal dissipation and variability in electrical breakdown of carbon nanotube devices," *Physical Review B,* vol. 82, p. 205406, Nov 5 2010.

[32] A. D. Liao, J. Z. Wu, X. R. Wang, K. Tahy, D. Jena, H. J. Dai, and E. Pop, "Thermally Limited Current Carrying Ability of Graphene Nanoribbons," *Physical Review Letters,* vol. 106, p. 256801, Jun 20 2011.

[33] K. H. Baloch, N. Voskanian, M. Bronsgeest, and J. Cumings, "Remote Joule heating by a carbon nanotube," *Nature Nanotechnology,* vol. 7, pp. 315-318, May 2012.

[34] H. Maune, H. Y. Chiu, and M. Bockrath, "Thermal resistance of the nanoscale constrictions between carbon nanotubes and solid substrates," *Applied Physics Letters,* vol. 89, p. 013109, Jul 3 2006.

[35] D. G. Cahill, "Thermal-Conductivity Measurement from 30-K to 750-K - the 3-Omega Method," *Review of Scientific Instruments,* vol. 61, pp. 802-808, Feb 1990.

[36] R. M. Costescu, M. A. Wall, and D. G. Cahill, "Thermal conductance of epitaxial interfaces," *Physical Review B,* vol. 67, p. 054302, Feb 1 2003.

[37] S. T. Huxtable, D. G. Cahill, S. Shenogin, L. Xue, R. Ozisik, P. Barone, M. Usrey, M. S. Strano, G. Siddons, M. Shim, and P. Keblinski, "Interfacial heat flow in carbon nanotube suspensions," *Nature Materials,* vol. 2, pp. 731-734, 2003.

[38] H. K. Lyeo and D. G. Cahill, "Thermal conductance of interfaces between highly dissimilar materials," *Physical Review B,* vol. 73, pp. 144301-1-6, Apr 2006.

[39] Z.-Y. Ong and E. Pop, "Molecular Dynamics Simulation of Thermal Boundary Conductance Between Carbon Nanotubes and SiO_2," *Physical Review B,* vol. 81, p. 155408, 2010.

[40] E. T. Swartz and R. O. Pohl, "Thermal boundary resistance," *Reviews of Modern Physics,* vol. 61, p. 605, 1989.

[41] K. Hess and P. Vogl, "Remote Polar Phonon-Scattering in Silicon Inversion Layers," *Solid State Communications,* vol. 30, pp. 807-809, 1979.

[42] V. Perebeinos, S. V. Rotkin, A. G. Petrov, and P. Avouris, "The Effects of Substrate Phonon Mode Scattering on Transport in Carbon Nanotubes," *Nano Letters,* vol. 9, pp. 312-316 2009.

[43] S. V. Rotkin, V. Perebeinos, A. G. Petrov, and P. Avouris, "An Essential Mechanism of Heat Dissipation in Carbon Nanotube Electronics," *Nano Letters,* vol. 9, pp. 1850-1855, May 2009.

[44] M. V. Fischetti, D. A. Neumayer, and E. A. Cartier, "Effective electron mobility in Si inversion layers in metal-oxide-semiconductor systems with a high-kappa insulator: The role of remote phonon scattering," *Journal of Applied Physics,* vol. 90, pp. 4587-4608, Nov 1 2001.

[45] A. Liao, Y. Zhao, and E. Pop, "Avalanche-Induced Current Enhancement in Semiconducting Carbon Nanotubes," *Physical Review Letters,* vol. 101, p. 256804, Dec 19 2008.

[46] K. Gopalakrishnan, R. Woo, C. Jungemann, P. B. Griffin, and J. D. Plummer, "Impact ionization MOS (I-MOS) - Part II: Experimental results," *IEEE Transactions on Electron Devices,* vol. 52, pp. 77-84, Jan 2005.

[47] D. Jena, T. Fang, Q. Zhang, and H. L. Xing, "Zener tunneling in semiconducting nanotube and graphene nanoribbon p-n junctions," *Applied Physics Letters,* vol. 93, Sep 15 2008.

[48] Q. Zhang, W. Zhao, and A. Seabaugh, "Low-subthreshold-swing tunnel transistors," *IEEE Electron Device Letters,* vol. 27, pp. 297-300, Apr 2006.

[49] J. Appenzeller, Y. M. Lin, J. Knoch, and P. Avouris, "Band-to-band tunneling in carbon nanotube field-effect transistors," *Physical Review Letters,* vol. 93, p. 196805, Nov 5 2004.

CHAPTER 3

THERMAL DISSIPATION AND VARIABILITY IN ELECTRICAL BREAKDOWN OF CARBON NANOTUBE DEVICES

3.1 Introduction

While Joule heating in carbon nanotubes (CNTs) can degrade electrical performance, posing reliability concerns as in other electronics, electrical Joule breakdown has also been used for fabrication purposes. One such application is to remove metallic CNTs in integrated circuits [1-3]; however the technique is not precise, owing to the lack of fine control over CNT heat dissipation. It can also be used to fabricate narrow break gaps that allow the formation of nanoscale contacts [4]. It is presently understood that the thermal boundary conductance (TBC) at CNT interfaces with the environment, substrate, or contacts plays the limiting role in thermal dissipation [5-7]. In addition, the interaction of CNTs with the environment may also change their effective thermal conductivity [8, 9]. However, little is currently known about the details of the thermal interaction between CNTs and common dielectrics, including the roles of dielectric surface roughness or of CNT diameter and chirality (e.g. metallic vs. semiconducting).

In this study, we examine electrical breakdown and thermal dissipation of CNT devices with the most common interface used in integrated circuit experiments, that of SiO_2 as shown in Fig. 3.1A. We employ electrical breakdown thermometry [6, 10] to extract the TBC between CNTs and SiO_2 for metallic (m-CNT) and semiconducting nanotubes (s-CNT) of diameters $1 < d < 4$ nm. We find the TBC per unit length scales proportionally with CNT diameter, confirming recent simulation work [11]. We also find that m-CNTs appear to have better and more consistent thermal coupling with SiO_2 than s-CNTs, indicating a fundamental challenge for complete m-CNT removal in circuits via electrical breakdowns. We compare our results to both a diffuse mismatch model (DMM) and to molecular dynamics (MD) simulations. The latter reveal the role played by the

---

This chapter is reprinted from A. Liao, R. Alizadegan, Z. Y. Ong, S. Dutta, F. Xiong, K. J. Hsia, and E. Pop, "Thermal dissipation and variability in electrical breakdown of carbon nanotube devices," *Physical Review B,* vol. 82, p. 205406, Nov 5 2010. Copyright 2010, American Physical Society.

thermal "footprint" of a deformable CNT on such dielectric substrates. Finally, we uncover the significant role of variability in threshold voltage (for s-CNTs) and of SiO_2 surface roughness (for both m- and s-CNTs) in heat dissipation and electrical breakdown.

3.2 Experiments and Data Extraction

We fabricated and conducted experiments on carbon nanotube devices in the same back-gated configuration as our previous work, using semi-circular electrodes for better CNT length control [12-14] (here, $2 \leq L \leq 5.6$ μm) as shown in Figs. 3.1 and 3.2. The SiO_2 is thermally grown dry oxide, approximately 90 nm thick. We focused on nanotubes that showed high-bias current near ~25 μA [15] and had diameters $d < 4$ nm as measured by atomic force microscopy (AFM), to ensure devices were single-walled. In addition, only electrical breakdowns with a single, clean drop to zero current were selected, which are typical of single-wall single-connection devices, as shown in Fig. 3.1B; by contrast, multiwall CNTs and CNT bundles exhibit higher currents and break down with multiple current steps [16]. Joule heating was achieved by increasing the source-drain voltage ($V_{SD} > 0$) while maintaining a negative gate bias ($V_{GD} \approx$ -15 V). In semiconducting CNTs this leads to hole-only conduction [12], deliberately avoiding ambipolar behavior [17] which would complicate the analysis. Metallic CNTs show no gate voltage dependence in room

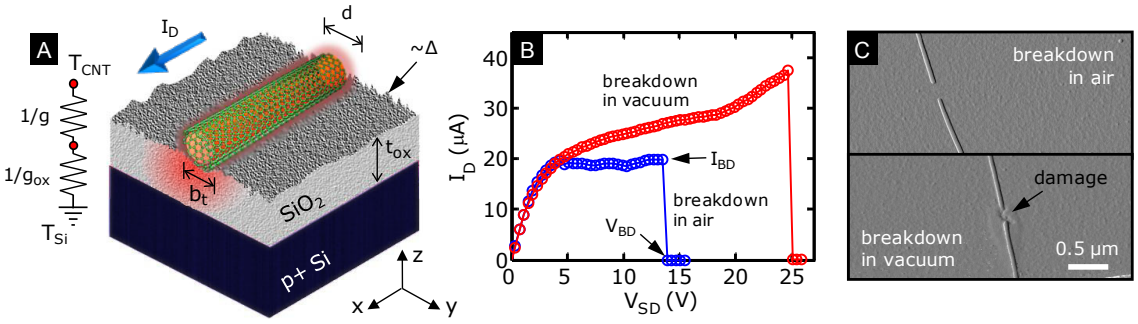

Fig. 3.1(A) Schematic cross-section of typical CNT device with diameter d and thermal footprint b_t (also see Fig. 3.5) on SiO_2 substrate with thickness t_{ox} and surface roughness Δ. The p+ silicon is used as a back-gate. The device layout with source and drain terminals is shown in Fig. 3.2(A). As current (I_D) passes in the CNT, the generated Joule heat dissipates through the substrate. The equivalent thermal circuit includes CNT-SiO_2 interface thermal resistance ($1/g$) and spreading resistance in the SiO_2 ($1/g_{ox}$). (B) Typical electrical breakdown of similar CNTs shows higher breakdown power in vacuum (~10^{-5} torr) than in ambient air. This illustrates the role of oxygen for CNT breakdown in air. (C) Atomic force microscopy (AFM) images of CNTs broken in air (top) and vacuum (bottom). Breakdowns in vacuum can lead to SiO_2 surface damage, which is not observed for air breakdowns.

temperature, ambient conditions. Increasing V_{SD} leads to increasing the power input, which causes the CNT temperature to rise through Joule heating and leads to physical breakdown. We note that in this work the drain is always grounded and the source is the positive terminal, referring to the source of carriers and current flow.

The breakdown voltage, $V_{SD} = V_{BD}$, is taken to be the voltage at which the drain current (I_D) irreversibly drops to zero, as shown in Fig. 3.1B. We assume that during the breakdown process the CNT stays on the surface and that no buckling or delamination from the surface occurs as a result of the small thermal expansion coefficient of CNTs [18]. Typical broken devices under AFM imaging are shown in Figs. 3.1C and 3.2A The power dissipated within the CNT at breakdown is $P_{BD} = I_D(V_{BD}–I_DR_C)$. The combined resistance of the source and drain contacts, R_C, is estimated from the inverse slope of the low-bias I_D-V_{SD} plot [6, 19], $R_C \approx (dI_D/dV_{DS})^{-1}$, which includes the quantum contact resistance (R_0 = 6.5 kΩ). The experiments in this study were performed in air where nanotubes are known to break from self-heating and oxidation at a relatively well-known temperature [20], $T_{BD} \approx 600$°C. By comparison, device breakdowns performed in ~10^{-5} Torr vacuum showed CNTs of similar lengths and diameters breaking at higher power and thus higher temperatures, as in Fig. 3.1B. This suggests that CNT device breakdowns in vacuum occur by a mechanism other than oxidation, e.g. at nanotube defects [21] or by failure of the underlying SiO_2. The latter is supported by the observation of damage to the SiO_2 substrate in some samples, as seen in Fig. 3.1C, which is never seen for breakdowns in air.

We now return to discuss the temperature profile of CNTs during Joule heating, and restrict ourselves to in-air breakdowns for the rest of the chapter. Figure 3.2A displays the breakdown location (L_{BD}) along a CNT, as extracted from scanning electron microscope (SEM) imaging. Figure 3.2B shows a histogram of the normalized breakdown locations for ~40 CNTs in this study, distinguishing between m-CNT and s-CNTs. The majority of m-CNTs break at their hottest point near the middle while most s-CNTs break closer to the grounded drain, where the field is higher and the carrier density is lower. Both of these observations are indicative of diffusive heat [6] and charge [22] transport, and of relatively negligible contact resistance. At high field the electron or hole scattering mean free path (MFP) with optical phonons (OP) approaches the minimum value $\lambda_{OP,ems} \sim 15d$

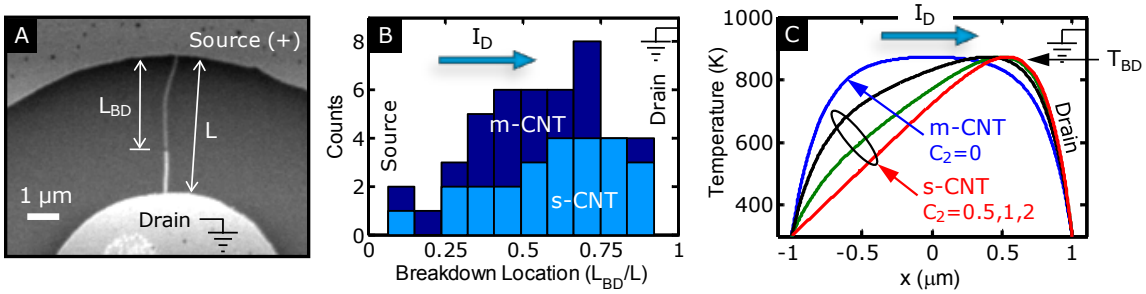

Fig. 3.2 (A) Scanning electron microscope (SEM) image of CNT device showing breakdown location (L_{BD}). (B) Histogram of breakdown location normalized by CNT length (L_{BD}/L) indicating the majority of m-CNTs break near the middle and s-CNTs break closer to the drain. Break point is always observed along the CNT, suggesting good contacts with negligible heating. (C) Computed temperature distribution along a 2 µm long CNT (typical in our study) with Eq. (3.2) using $C_1 = 1$ and varying C_2. The maximum temperature is shown at the breakdown condition (T_{BD}). $C_2 = 0$ corresponds to m-CNTs (uniform heat dissipation) and $C_2 > 0$ corresponds to s-CNTs. For s-CNTs biased under hole conduction the heat generation and temperature profile are skewed towards the ground (drain) terminal. Block arrows in (B) and (C) show direction of hole flow.

where d is the diameter in nm [12, 19]. This MFP is significantly shorter than the CNT lengths used in this work (several microns).

To understand the temperature profiles of m-CNTs and s-CNTs, and to extract the interfacial thermal conductance per unit length (g) between CNT and SiO_2 from the breakdown data, we solve the heat diffusion equation along the CNT [6]. The heat generation per unit length can be captured both as uniform (for m-CNTs) and asymmetric (for s-CNTs), by expressing it as:

$$p(x) = p_0\left(C_1 + \frac{C_2 x}{L}\right) \tag{3.1}$$

where $-L/2 \le x \le L/2$, L is the length of the CNT, C_1 and C_2 are unitless parameters and p_0 is a constant term. We note that to a good approximation the heat generation in CNTs is independent of temperature, as the optical phonon emission length (the strongest inelastic scattering mechanism responsible for Joule heating) has very weak temperature dependence [6, 12].

Because the heat generation is uniform along m-CNTs from the constant electric field and charge density (barring significant and asymmetric contact resistance [23, 24]), we simply set $C_1 = 1$ and $C_2 = 0$. This implies $p_0 = P_{BD}/L$ at breakdown in m-CNTs. For s-CNTs, a linear heat generation profile captures the asymmetry caused by non-uniform

electric field and charge density [25]. The general expression for the temperature along the CNT at breakdown is:

$$T(x) = T_0 + \frac{P_{BD}}{g_{tot} L}\left[C_1 + \frac{C_2 x}{L} - \frac{C_1 \cosh\left(\frac{x}{L_H}\right)}{\cosh\left(\frac{L}{2L_H}\right)} - \frac{C_2 \sinh\left(\frac{x}{L_H}\right)}{2\sinh\left(\frac{L}{2L_H}\right)} \right] \tag{3.2}$$

where $L_H = (kA/g)^{1/2}$ is the thermal healing length (of the order ~0.2 μm) [6, 26], k is the thermal conductivity of the CNT [22], g_{tot} is the thermal conductance per unit length from CNT to ambient (see Section 3.3 below), and $A = \pi ad$ is the cross-sectional area assuming a CNT wall thickness a = 0.34 nm.

The typical "inverted U" shape of the temperature profile under uniform heat generation in m-CNTs is shown in Fig. 3.2C with $C_2 = 0$. This has previously been observed experimentally in nanotubes under high bias operation, both by scanning thermal microscopy (SThM) [27] and by coating the CNTs with a phase-change material which changes volume as it heats up [26].

On the other hand, s-CNTs have non-uniform electric field and charge density along their length, leading to off-center heat dissipation [25]. This is captured by changing the value of the parameter $C_2 > 0$ above, as shown in Fig. 3.2C. We take this simple approach because uncertainties in threshold voltage, contact resistance, and contributions made by infrequent defects make it difficult to provide a more exact solution of the temperature profile in every s-CNT measured (by contrast, m-CNTs are immune to threshold voltage variations). More specifically, in our analysis below we choose $C_1 = 1$ and $C_2 = 0.65$ for s-CNTs, such that the hot spot location corresponds to $L_{BD}/L \approx 0.7$ as noted in the breakdown histogram, Fig. 3.2B.

3.3 Modeling

To understand the dependence of thermal coupling g on CNT diameter and substrate properties, we use a diffuse mismatch model (DMM) [28] similar to that previously applied to multiwall carbon nanotubes [29] and graphene [30]. The DMM is used to establish an upper bound for heat transport across an interface, as limited by the phonon density of states (PDOS). This approach also presents an advantage of speed and flexibility

Table 3.1 Simulation parameters

Parameter	Value
v_{CNT}	932 m/s
v_{ox}	4.1 km/s
N_{CNT}	16.3 atoms/Å
N_{ox}	0.0227 molecules/Å^3
T_{BD}	873 K

over full MD methods [11]. The model calculates the transmission probability, α, for heat transfer across an interface while assuming all phonons scatter diffusely at the interface. By equating the phonon energy flux from the CNT to the SiO_2 with that from the SiO_2 to the CNT and using a detailed balance argument for all frequencies [30, 31], α is given as:

$$\alpha = \frac{\frac{1}{4}\int \omega N_{OX} f_{BE,OX} D_{OX} v_{ox} d\omega}{\frac{\int \omega N_{CNT} f_{BE,CNT} D_{CNT} \langle v_{CNT} \rangle d\omega}{ad} + \frac{1}{4}\int \omega N_{OX} f_{BE,OX} D_{OX} v_{ox} d\omega} \tag{3.3}$$

where N refers to the atomic density (in atoms/cm^3 for SiO_2 and atoms/cm for nanotubes), v is the phonon velocity, ω is the phonon frequency, f_{BE} is the Bose-Einstein (BE) distribution, and D is the PDOS per atom as calculated by MD simulations [11]. We use the realistic PDOS rather than a Debye approximation because the latter has been previously found to cause large discrepancies with experimental data at high temperature [32]. In addition, the linear Debye approximation would not account for the quadratic CNT flexure modes [33]. The PDOS for a (10,10) nanotube with 1.37 nm diameter is calculated and shown in Fig. 3.3. Using the PDOS from CNTs of other diameters did not change our results significantly (presumably because the proportion of phonon modes remains approximately the same [11]); hence, we used the PDOS shown in Fig. 3.3 as the phonon weighing function throughout the remainder of this work.

The phonon velocity in the amorphous SiO_2 is assumed to be isotropic and fitted with a single value [34], as shown in Table 3.1. However, the CNT phonon velocity includes contributions from both the transverse and longitudinal polarizations along the c-axis (out-of-plane direction) of graphite, v_c [30, 35]. Not included are the a-axis (in-plane) modes which contribute minimally to thermal coupling in the geometry of interest, and

are more relevant to vertical CNTs on a surface [36]. We note, however, that even for vertical CNTs some degree of tip bending must always exist; thus, the geometry examined here and in Ref. [11] is likely to be most relevant. The value of $<v_{CNT}>$ is derived from a geometrical averaging of v_c over the shape of the CNT, described later in more detail. The list of parameters is shown in Table 3.1.

Knowing the transmission probability, we can now calculate the flux of phonons through the interface. This gives the thermal conductance per unit length from the CNT to SiO_2 as:

$$g = \frac{N_{CNT} \cdot b_t}{ad} \int \hbar\omega \frac{\partial f_{BE,CNT}}{\partial T} D_{CNT} \langle v_{CNT} \rangle \alpha d\omega \tag{3.4}$$

where b_t is the effective thermal contact width or footprint between the CNT and the substrate, to be determined by MD simulations (Fig. 3.1 and Fig. 3.5). This footprint is the effective width between CNT and the substrate over which heat is being transferred. Finally, to calculate a thermal boundary conductance that is comparable to experimental data, we must also include the effect of heat spreading into the oxide, given as [37]:

$$g_{ox} = \frac{\pi\kappa_{ox}}{\ln\left(\frac{8t_{ox}}{\pi b_t}\right)} \tag{3.5}$$

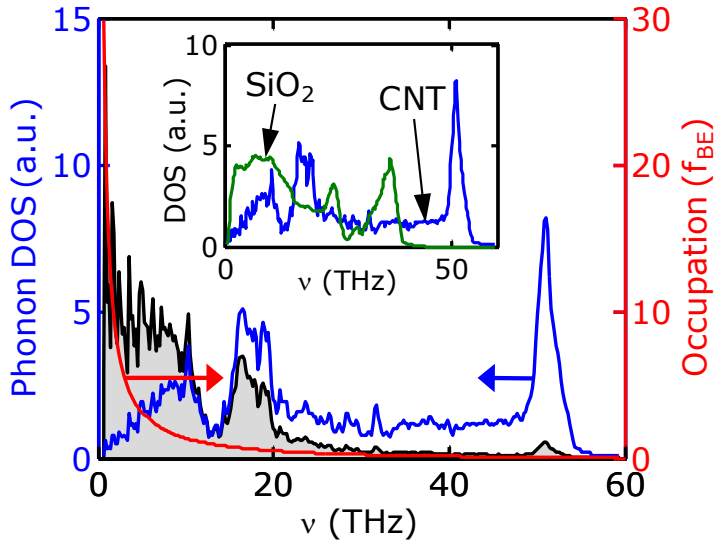

Fig. 3.3 The phonon density of states (PDOS) for a (10,10) nanotube from MD simulations [10]. The Bose-Einstein occupation (f_{BE}) at room temperature is plotted in red against the right axis. Shaded in gray is the product of the PDOS with f_{BE}, showing diminished contribution from higher frequency phonon modes. The inset shows the PDOS of the CNT and that of SiO_2, the latter displaying a lower cutoff near 40 THz.

where $\kappa_{ox} \approx 1.4$ $Wm^{-1}K^{-1}$ is the SiO_2 thermal conductivity and $t_{ox} \approx 90$ nm is the SiO_2 layer thickness. This simple expression is appropriate when $t_{ox} \gg b_t$ as in our work, and the thermal spreading resistance contribution of the SiO_2 accounts for approximately 10-30% of the total thermal resistance. The total thermal conductance per unit length from CNT to ambient, as used in equation (3.2), is given by the simple thermal series network shown in Fig. 3.1:

$$g_{tot} = \left(\frac{1}{g} + \frac{1}{g_{ox}} \right)^{-1} \tag{3.6}$$

We note that any additional thermal spreading resistance into the Si wafer is negligible, and thus the Si wafer is assumed to be isothermal at $T_{Si} = 293$ K. Similarly, heat loss to ambient air can be neglected, where $g_{air} \sim 4 \times 10^{-4}$ $WK^{-1}m^{-1}$ has been previously estimated as an upper limit at one atmosphere [38], three orders of magnitude lower than the heat loss to substrate.

3.4 Derivation of CNT Shape and Footprint

3.4.1 Equilibrium Shape of a CNT

Nanotubes interact with the SiO_2 substrate through van der Waals (vdW) forces. In addition, our previous MD simulations [11] have shown that such CNTs do not remain rigid cylinders, but instead deform to minimize their overall vdW and curvature energy. Beyond a certain diameter CNTs relax to a compressed shape [39, 40], which changes both their geometrical and equivalent thermal footprint on the substrate. To accurately calculate the shape and thermal footprint of the CNT, we employ MD simulations with a simplified Lennard-Jones (LJ) 6-12 potential:

$$V = 4\varepsilon \left[\left(\frac{\sigma}{r} \right)^{12} - \left(\frac{\sigma}{r} \right)^{6} \right]. \tag{3.7}$$

Here, we simplify the SiO_2 substrate as a continuum plane. Therefore the collective vdW interaction per carbon atom situated at a height h above an infinite half-space of SiO_2 can be approximated by the triple integral

$$V_{vdW} = \sum_{i=Si,O} \int_0^\infty \int_{-\infty}^\infty \int_{-\infty}^\infty 4\varepsilon_i n_i \left[\left(\frac{\sigma_i}{r} \right)^{12} - \left(\frac{\sigma_i}{r} \right)^{6} \right] dxdydz \tag{3.8}$$

in which

$$r = \sqrt{x^2 + y^2 + (z+h)^2} \tag{3.9}$$

and

$$\begin{aligned} \varepsilon_{Si} &= 8.909 \text{ meV}, \sigma_{Si} = 3.326 \text{ Å}, n_{Si} = 0.0227 \text{ Å}^{-3} \\ \varepsilon_O &= 3.442 \text{ meV}, \sigma_O = 3.001 \text{ Å}, n_O = 0.0454 \text{ Å}^{-3} \end{aligned}. \tag{3.10}$$

The values here are based on the Universal Force Field (UFF) model by Rappe et al. [41] and were used in our previous MD simulations as well [11]. The integral in equation (3.8) can be evaluated analytically. It should be noted that this integral tends to give a lower bound estimate of the total interaction potential because it ignores the effects of local spikes of closely positioned atoms. The estimation error is reduced by assuming a relaxed configuration for the nearby silica molecules. Such an analysis gives

$$V_{vdW} = \sum_{i=Si,O} \frac{2\pi\varepsilon_i \sigma_i^3 n_i}{45} [2(\sigma_i / h)^9 - 15(\sigma_i / h)^3] \tag{3.11}$$

which has a similar form as the original LJ potential – except with different exponents and pre-factors. This effectively alludes to an h^{-3} dependence of the vdW interaction potential. A plot of both the calculated potential and its second derivative (which is proportional to the interaction spring constant) is shown in Fig. 3.4.

For the covalent C-C interaction we used the empirical bond order Tersoff-Brenner potential [42]. In addition to this potential, we used an intra-molecular LJ vdW potential with the following parameters for graphite [43]:

$$\varepsilon_C = 3.02 \text{ meV}, \sigma_C = 3.39 \text{ Å} \tag{3.12}$$

All MD simulations were carried out until the transient motions died off and a final steady-state solution was reached.

3.4.2 Thermal Footprint of a CNT

To determine the thermal footprint of the CNT on SiO_2, we consider the square root of the second derivative of the vdW potential with respect to h as heat transfer depends on this effective "spring constant" between the substrate and CNT. For example, the phonon velocities are expected to be proportional to the square root of this spring constant. Thus, to find the effective thermal footprint we used the square root of the spring constant to weigh the horizontal change in position, Δx.

The thermal footprint (b_t) should not to be confused with the geometric footprint, b_g, the physical contact region between the CNT and substrate. In the case of small diameter CNTs, the effective thermal footprint can even be greater than the lateral width of the CNTs, i.e. their diameter. This occurs because in addition to the bottom half of the CNT conducting heat to the substrate, there is also thermal coupling from the top half of the CNT. The results of these simulations are shown in Fig. 3.5. Because MD simulations can be carried out for only one CNT of a particular diameter at a time, several were conducted for CNTs over a range of diameters 5–49 Å. We found the following quadratic function fit the simulation results of the thermal footprint for any diameter within the simulated range (Fig. 3.5A):

$$b_t = 0.037d^2 + 1.1d \tag{3.13}$$

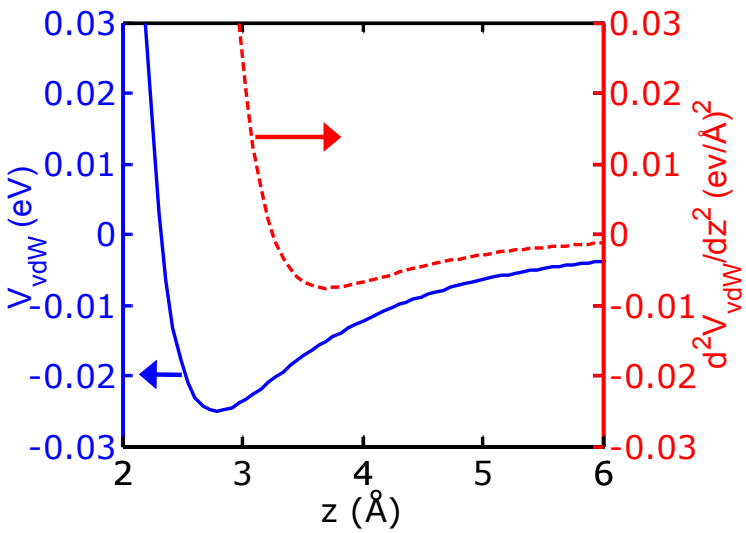

Fig. 3.4 Van der Waals potential (blue solid line) interaction between CNT and SiO_2, as used in calculations to derive the thermal footprint (Fig. 3.5). The second derivative of the potential (red dashed line) with respect to distance from the surface (z) is used to weigh the contribution of each atom to the effective thermal footprint (b_t) of the CNT.

where both b_t and d are both in nanometers.

Our simulations further suggest that there are two different regimes represented by different equilibrium shapes of CNTs, as shown in Fig. 3.5. In the first regime (labeled "I"), the diameter of the CNT is $d < 2.1$ nm and the curvature energy of the CNT is stronger than the vdW energy with the substrate. Thus in the first regime the cross-section of the nanotube more closely resembles a perfect circle, as shown on the left of Fig. 3.5B for a (7,7) CNT. In addition, the geometrical footprint (calculated by finding the furthest distance between the lowest points on the CNT) in this regime remains nearly constant at ~1.4 Å, the chemical bond length, as can be seen in Fig. 3.5A.

In the second regime (labeled "II") the diameter $d > 2.1$ nm, and the vdW energy with

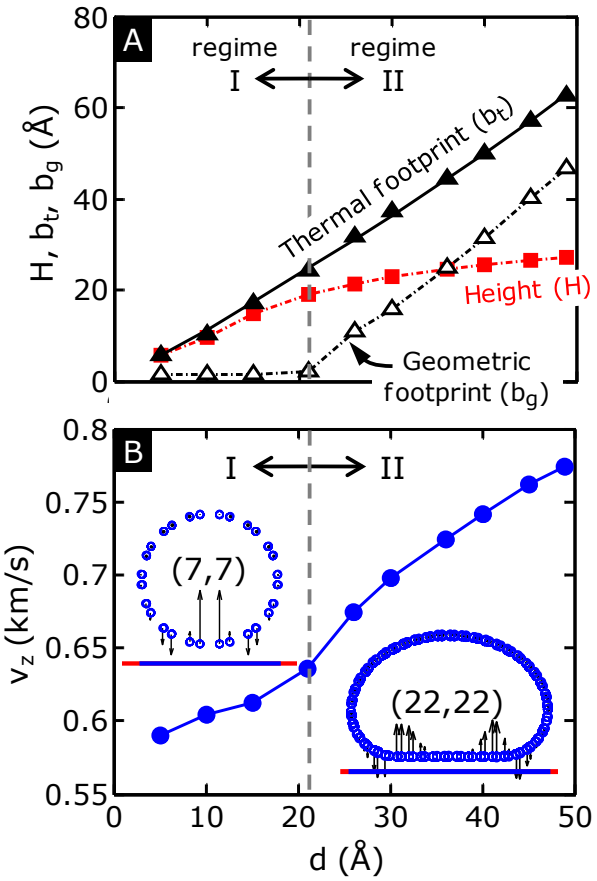

Fig. 3.5 (A) Nanotube height (■), geometrical footprint (Δ), and thermal footprint (▲) on the SiO_2 substrate as a function of CNT diameter, obtained from MD simulations. A fit to the thermal footprint is shown as a solid line from Eq. (13). (B) Calculations reveal two distinct regimes: in regime I (left, $d < 2.1$ nm) the CNT shape is nearly circular, dominated by the curvature energy; in regime II (right, $d > 2.1$ nm) the CNT shape becomes flattened, with a stronger influence of the surface vdW interaction. Small vertical arrows indicate the relative magnitude of vdW forces with the substrate at each atomic position.

the substrate is stronger than the curvature energy of the CNT. Hence the final minimum energy shape for the CNT will be that of a deformed circle, as shown for a (22,22) CNT on the right of Fig. 3.5B. It is in this regime where the geometrical footprint starts to increase approximately linearly with diameter, as shown in Fig. 3.5A. Another interesting observation is noted due to the repulsive nature of the vdW forces at very close distances, whose relative magnitudes are illustrated with arrows in Fig. 3.5B. In this case, the bottom of the CNT is not perfectly flat. Instead the middle of the bottom region buckles up slightly, such that the force at the center is nearly zero. All these effects are captured in the thermal footprint calculation (b_t) fitted by equation (3.12) above, and used in the DMM thermal coupling simulations.

3.5 Discussion

Figure 3.6A shows the directly measured power at breakdown (P_{BD}), and Fig. 3.6B displays the extracted TBC (g) vs. diameter d for 29 metallic and semiconducting CNT devices. Fig 3.6B also includes modeling using the DMM described above (solid line) and the dashed lines fitted to MD simulations with vdW coupling strengths $\chi = 1$ and $\chi = 2$, as described in Ref. [11]. Both data and modeling trends in Fig. 3.6B suggest that the TBC increases with diameter. The range of extracted g corresponds to approximately the same order of magnitude previously extracted from thermal breakdowns [6, 44]. A representative set of vertical error bars on one of the m-CNTs corresponds to a ±50 °C uncertainty in breakdown temperature. Horizontal error bars represent ±0.4 nm uncertainty in diameter from AFM measurements. Vertical error bars on the s-CNTs are derived as follows. The upper limit is set by assuming $L_{BD}/L = 0.75$ and the lower limit is set in the limit of uniform heat generation. It is interesting to note that that non-uniform heat generation plays a larger role in large diameter s-CNTs than in small diameter s-CNTs.

3.5.1 Dependence of Thermal Coupling on Diameter

We observe that g increases with diameter up to ~0.7 $WK^{-1}m^{-1}$ per unit length for the largest single-wall CNTs considered ($d \sim 4$ nm). The diameter dependence of g is primarily a result of the increase in thermal footprint, as shown in Fig 3.5A. Also plotted in Fig. 3.6B are our previous MD simulations results [11]. The results from the MD simulations

do give lower values of g because the DMM assumes, by definition, that all phonons are scattered diffusely at the interface [28] whereas this does not necessarily happen in MD simulations.

We also obtain the thermal contact conductance per unit area, $h = g/b_t$, as plotted in Fig. 3.6C and showing almost no dependence on diameter. From the breakdown experiments this value is in the range $h \approx 20$–200 $MWK^{-1}m^{-2}$ which is slightly larger than that recently obtained for graphene on SiO_2 [45]. The DMM simulation predicts an upper limit for $h \approx 220$ $MWK^{-1}m^{-2}$ with almost no diameter dependence. This appears to suggest

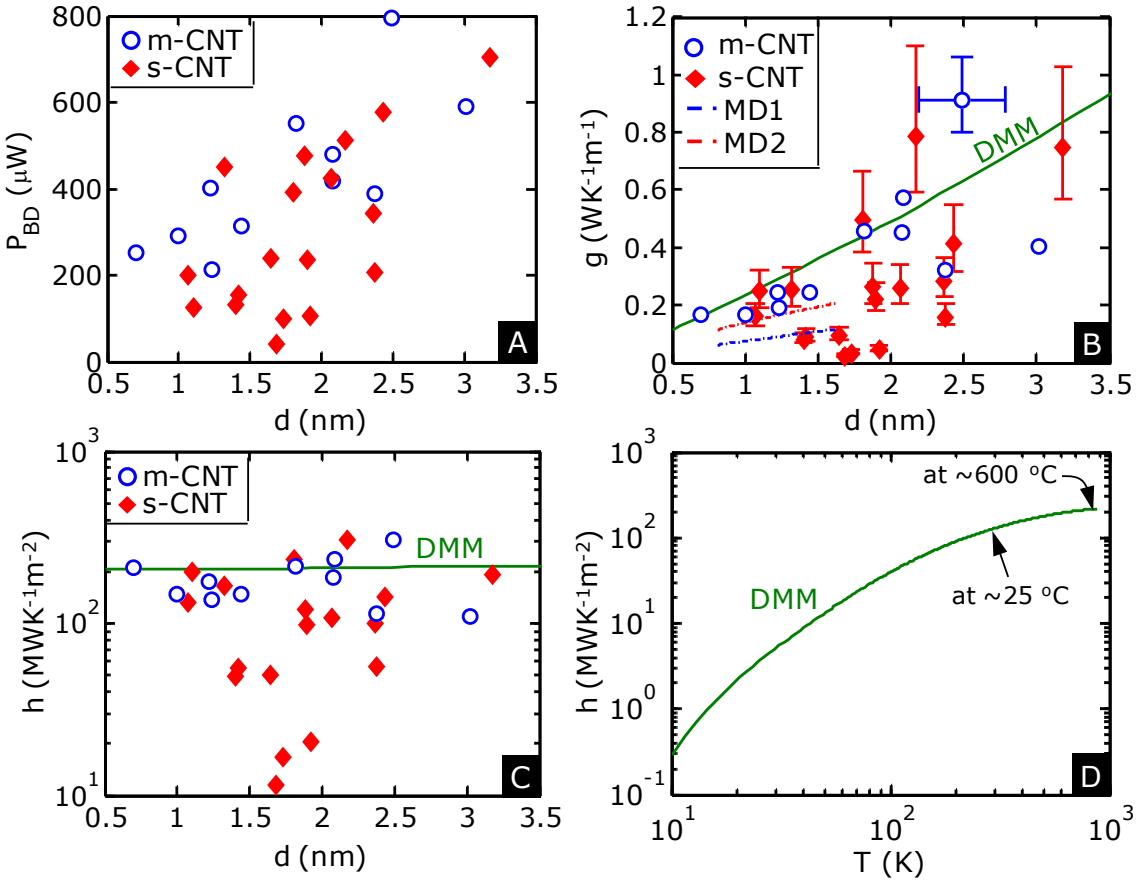

Fig. 3.6 (A) Electrical breakdown power (in air) of CNTs vs. diameter d, showing proportional scaling. (B) Extracted CNT-SiO_2 thermal coupling g vs. d (see text) for both metallic (m) and semiconducting (s) CNTs. Solid line is the DMM calculation and dash-dotted lines are fitted to MD simulations with different vdW coupling strengths (χ=1 and χ=2 respectively, see Ref. [10]). (C) CNT-SiO_2 thermal coupling per unit area h vs. d, showing the DMM represents an upper-limit scenario of heat dissipation. The spread in the data and lower apparent thermal coupling in practice is attributed to SiO_2 surface roughness, and charge trapping near semiconducting CNTs (see text). (D) Calculated temperature dependence of the upper limit thermal coupling per unit area. Thermal coupling at room temperature (~130 $MWK^{-1}m^{-2}$) is ~40% lower than at the breakdown temperature (~220 $MWK^{-1}m^{-2}$).

the upper range of the h values obtained experimentally. We note that the extracted and simulated TBCs in this study thus far are at an elevated temperature, given approximately by the CNT breakdown condition (~873 K). To understand the effects of temperature on TBC, we plot our DMM model in Fig. 3.6D vs. temperature. This shows an expected increase in TBC with temperature, consistent both with graphene-SiO_2 experiments [45] and with CNT-SiO_2 MD simulations [11]. The thermal coupling per unit area at room temperature is ~130 $MWK^{-1}m^{-2}$, or approximately 40 percent lower than the thermal coupling near the CNT breakdown temperature.

3.5.2 Dependence of TBC on Phonon DOS and Velocity

In addition to the thermal footprint, the PDOS of the SiO_2 as well as the distribution function (f_{BE}) also play a role in heat transport across the interface. We recall that the inset of Fig. 3.3 showed the calculated PDOS for both a (10,10) CNT and the SiO_2 substrate. While the nanotube contains a large PDOS peak at 53 THz, this does not come into play because there are no equivalent high-frequency modes in the SiO_2. Fig. 3.3 also shows the Bose-Einstein distribution function at the CNT breakdown temperature (T_{BD} ~ 600 °C). The distribution suggests very low occupation for all high-frequency CNT modes. Since the Debye temperature for CNTs is very high, we expect that most substrates will serve as a low-pass filter for CNT phonons.

Aside from changing the thermal footprint, the deformed shape of the CNT also affects the average phonon velocity. This is a more subtle effect than that of diameter or surface roughness, but it is included here for completeness. For instance, in the second regime (d > 2.1 nm) the CNT becomes flattened, leading to more atoms vibrating perpendicular to the substrate interface. After numerical MD calculations of the CNT shape (Fig. 3.5) we averaged the angle of CNT atomic vibrations perpendicular to the plane of the surface to adjust accordingly the value of v_c listed in Table 3.1. If a perfect cylinder is assumed, then the average would result in $\langle v_{CNT} \rangle = \pi v_c / 4$.

3.5.3 Dependence of TBC on Surface Roughness

There are several variables contributing to the spread of the experimental data shown in Figs. 3.6 and 3.7. The primary contributor is surface roughness. Since the value of g is directly related to the contact area at the interface, an imperfect surface is roughly equiva-

lent to a decreased thermal contact area. Figure 3.7A replots the calculated TBC vs. diameter for a perfectly smooth surface (100%), for 75% of the maximum contact area, and for 50% of the maximum contact area. To analyze how surface roughness affects the spread directly, we experimentally find the average surface step height, Δ, adjacent to the nanotube via AFM. However, intuitively we expect the *ratio* of diameter to roughness (d/Δ) to be more important. Thus, we expect larger diameter CNTs to be less affected by surface roughness than smaller diameter CNTs. Plotting g versus d/Δ in Fig. 3.6B, we see that the spread is smaller in these plots than in Fig. 3.6A and 3.7A, confirming our hypothesis.

3.5.4 Role of s-CNT vs. m-CNTs

We note that the spread in m-CNTs breakdown data is smaller than in s-CNTs in Figs. 3.6 and 3.7. We believe this is due to threshold voltage (V_{TH}) shifting in s-CNTs during the high-field measurement process, which m-CNTs are essentially immune to. As the devices are swept to high drain bias for breakdown, along with the applied gate bias (-15 V) this can lead to dynamic charge injection into the oxide, as studied in depth by Ref. [13]. To understand the effect of threshold voltage on breakdowns, we plot the extracted P_{BD} vs. initial V_{TH} in Fig. 3.7C, and find a slight but positive relationship. This suggests that in s-CNTs the variation in electronic behavior leads to the larger data spread, in addition to the variation due to surface roughness. Moreover, this also indicates a root cause which renders precisely selective breakdown of m-CNTs (e.g. in CNT net-

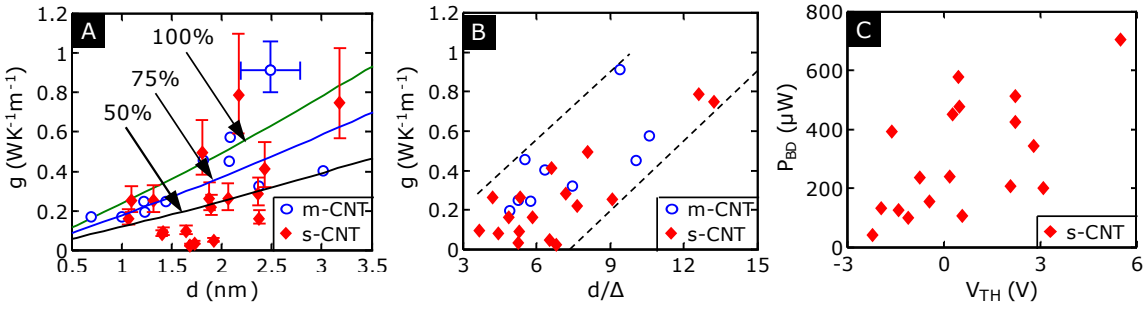

Fig. 3.7 (A) CNT-SiO_2 thermal coupling g vs. diameter d (symbols = data) and DMM simulations (lines) for perfect substrate contact (100%), and for 75% and 50% effective contact area due to SiO_2 surface roughness (also see Fig. 1). (B) Replot of same experimental data vs. diameter scaled by RMS surface roughness (d/Δ) measured by AFM near each CNT. This indicates the roles of SiO_2 surface roughness for thermal dissipation from CNTs. Dashed lines are added to guide the eye. (C) Breakdown power P_{BD} for semiconducting CNTs (s-CNTs) alone plotted with respect to threshold voltage (V_{TH}). The variance in V_{TH} is also a contributing factor to the spread in extracted thermal coupling data for s-CNTs.

works) as a challenging and imperfect approach: on one hand, the change in threshold voltage of s-CNTs can turn them "on" allowing them to break down, on the other hand the variation in surface roughness itself cannot guarantee that all m-CNTs will break down at the same input power, or voltage.

3.5.5 Comments on the Modeling Approach

It is important to note that both the DMM and MD simulations employed in this work only capture the lattice vibration (phonon) contribution to thermal coupling. Nevertheless, the DMM in general appears to represent an upper limit to the spread of the experimental data which is otherwise lowered by effects like surface roughness. However, recent theoretical work has also suggested a possible electronic contribution to heat transport through coupling with surface phonon polaritons (SPPs) from the oxide [46, 47]. The SPP interaction drops off exponentially with the CNT-substrate distance, perhaps leading to a larger electronic contribution to heat transport in regime II of the CNT shape ($d > 2.1$ nm), where more CNT atoms are closer to the SiO_2 surface. However, since the SPP potential is strongly dependent on the interaction distance, it will also be affected by substrate surface roughness. Given these circumstances it is difficult to rule out energy relaxation through SPP scattering in practice, although this appears to be significantly lower than the phonon coupling and any SPP contribution (however small) may become more significant in larger diameter CNTs ($d > 2.1$ nm).

Another mechanism for CNT-SiO_2 energy dissipation is inelastic phonon scattering at the interface, which is not captured by the DMM. Previously Chen et al. [45] had compared an elastic DMM calculated by Duda et al. [30] to the TBC between graphene and SiO_2 and found that the elastic DMM under-predicted the TBC by approximately an order magnitude. Hopkins [31] made a similar argument for inelastic scattering between acoustically mismatched materials. However our simulations do not differ from the data significantly; thus, our calculations suggest that the contribution of inelastic scattering here is small (perhaps a result of the 1-D nature of CNTs).

3.6 Conclusion

In summary, we have examined electrical breakdown and thermal dissipation between CNT devices and their SiO_2 substrate, the most common configuration found in CNT electronics. The breakdown location is invariably found in the middle of the CNT, consistent with the CNT temperature profile. In this context, thermal dissipation from CNT to SiO_2 dominates over dissipation at the CNT contacts. We found evidence of a direct relationship between the CNT-SiO_2 thermal boundary conductance (TBC) and the CNT diameter, in accord with previous MD simulations. To provide a more flexible means of analysis we developed a diffuse mismatch model (DMM) of the TBC using the full phonon density of states (PDOS). This approach appears to predict the upper limit of thermal transmission at the CNT-SiO_2 interface, and could be similarly applied to calculate the TBC of other dimensionally mismatched systems. Our experiments and modeling suggest a maximum TBC of ~0.7 $WK^{-1}m^{-1}$ per unit length for the largest diameter CNTs considered (d = 3–4 nm). The maximum thermal conductance per unit area corresponds to approximately 130 $MWK^{-1}m^{-2}$ at room temperature and 220 $MWK^{-1}m^{-2}$ at 600 ^{o}C.

We have also studied the thermal footprint of a CNT through MD simulations which find the atomic configuration of lowest energy. These reveal two interaction regimes, the first one at smaller diameters (d < 2.1 nm) where the CNT shape is dominated by its curvature energy, the other at larger diameters (d > 2.1 nm) where the CNT shape is dominated by Van der Waals (vdW) coupling with the substrate. Finally, we found that SiO_2 surface roughness strongly affects the TBC of such nanometer-sized interfaces. To improve CNT heat sinking applications, our results suggest the need to engineer ultra-flat surfaces, use large diameter CNTs, and find substrates with larger vdW coupling. To improve selective electrical breakdown of CNTs (e.g. metallic vs. semiconducting) it will also be essential to control the surface roughness of the substrate, as well as the threshold voltage of the semiconducting CNTs.

3.7 References

[1] P. C. Collins, M. S. Arnold, and P. Avouris, "Engineering carbon nanotubes and nanotube circuits using electrical breakdown," *Science,* vol. 292, pp. 706-709, Apr 27 2001.

[2] S. J. Kang, C. Kocabas, T. Ozel, M. Shim, N. Pimparkar, M. A. Alam, S. V. Rotkin, and J. A. Rogers, "High-performance electronics using dense, perfectly aligned arrays of single-walled carbon nanotubes," *Nat Nano,* vol. 2, pp. 230-236, 2007.

[3] N. Patil, A. Lin, Z. Jie, W. Hai, K. Anderson, H. S. P. Wong, and S. Mitra, "VMR: VLSI-compatible metallic carbon nanotube removal for imperfection-immune cascaded multi-stage digital logic circuits using Carbon Nanotube FETs," in *IEEE Intl. Electron Devices Mtg. (IEDM)*, Baltimore, MD, 2009, pp. 573-576.

[4] F. Xiong, A. D. Liao, D. Estrada, and E. Pop, "Low-Power Switching of Phase-Change Materials with Carbon Nanotube Electrodes," *Science,* vol. 332, pp. 568-570, Apr 29 2011.

[5] E. Pop, "The role of electrical and thermal contact resistance for Joule breakdown of single-wall carbon nanotubes," *Nanotechnology,* vol. 19, p. 295202, July 2008.

[6] E. Pop, D. A. Mann, K. E. Goodson, and H. J. Dai, "Electrical and thermal transport in metallic single-wall carbon nanotubes on insulating substrates," *J. Appl. Phys.,* vol. 101, p. 093710, May 2007.

[7] M. Steiner, M. Freitag, V. Perebeinos, J. C. Tsang, J. P. Small, M. Kinoshita, D. N. Yuan, J. Liu, and P. Avouris, "Phonon populations and electrical power dissipation in carbon nanotube transistors," *Nature Nanotechnology,* vol. 4, pp. 320-324, May 2009.

[8] J. Shiomi and S. Maruyama, "Molecular dynamics of diffusive-ballistic heat conduction in single-walled carbon nanotubes," *Japanese Journal of Applied Physics,* vol. 47, pp. 2005-2009, Apr 2008.

[9] R. Prasher, "Thermal conductance of single-walled carbon nanotube embedded in an elastic half-space," *Applied Physics Letters,* vol. 90, p. 143110, Apr 2 2007.

[10] H. Y. Chiu, V. V. Deshpande, H. W. C. Postma, C. N. Lau, C. Miko, L. Forro, and M. Bockrath, "Ballistic phonon thermal transport in multiwalled carbon nanotubes," *Physical Review Letters,* vol. 95, p. 226101, Nov 25 2005.

[11] Z.-Y. Ong and E. Pop, "Molecular Dynamics Simulation of Thermal Boundary Conductance Between Carbon Nanotubes and SiO_2," *Phys. Rev. B,* vol. 81, p. 155408, 2010.

[12] A. Liao, Y. Zhao, and E. Pop, "Avalanche-Induced Current Enhancement in Semiconducting Carbon Nanotubes," *Physical Review Letters,* vol. 101, p. 256804, Dec 19 2008.

[13] D. Estrada, A. Liao, S. Dutta, and E. Pop, "Reduction of Hysteresis for Carbon Nanotube Mobility Measurements Using Pulsed Characterization," *Nanotechnology,* vol. 21, p. 085702, 2010.

[14] J. Lee, A. Liao, E. Pop, and W. P. King, "Electrical and Thermal Coupling to a Single-Wall Carbon Nanotube Device Using an Electrothermal Nanoprobe," *Nano Letters,* vol. 9, pp. 1356-1361, Apr 2009.

[15] Z. Yao, C. L. Kane, and C. Dekker, "High-field electrical transport in single-wall carbon nanotubes," *Physical Review Letters,* vol. 84, pp. 2941-2944, Mar 27 2000.

[16] P. G. Collins, M. Hersam, M. Arnold, R. Martel, and P. Avouris, "Current saturation and electrical breakdown in multiwalled carbon nanotubes," *Phys. Rev. Lett.,* vol. 86, pp. 3128-3131, Apr 2 2001.

[17] Y. F. Chen and M. S. Fuhrer, "Electric-field-dependent charge-carrier velocity in semiconducting carbon nanotubes," *Physical Review Letters,* vol. 95, p. 236803, Dec 2 2005.

[18] P. K. Schelling and R. Keblinski, "Thermal expansion of carbon structures," *Physical Review B,* vol. 68, p. 035425, Jul 15 2003.

[19] Y. Zhao, A. Liao, and E. Pop, "Multiband Mobility in Semiconducting Carbon Nanotubes," *IEEE Electron Device Letters,* vol. 30, pp. 1078-1080, Oct 2009.

[20] K. Hata, D. N. Futaba, K. Mizuno, T. Namai, M. Yumura, and S. Iijima, "Water-assisted highly efficient synthesis of impurity-free single-waited carbon nanotubes," *Science,* vol. 306, pp. 1362-1364, Nov 19 2004.

[21] N. Y. Huang, J. C. She, J. Chen, S. Z. Deng, N. S. Xu, H. Bishop, S. E. Huq, L. Wang, D. Y. Zhong, E. G. Wang, and D. M. Chen, "Mechanism Responsible for Initiating Carbon Nanotube Vacuum Breakdown," *Physical Review Letters,* vol. 93, p. 075501, 2004.

[22] E. Pop, D. Mann, Q. Wang, K. Goodson, and H. J. Dai, "Thermal conductance of an individual single-wall carbon nanotube above room temperature," *Nano Letters,* vol. 6, pp. 96-100, Jan 2006.

[23] I. K. Hsu, R. Kumar, A. Bushmaker, S. B. Cronin, M. T. Pettes, L. Shi, T. Brintlinger, M. S. Fuhrer, and J. Cumings, "Optical measurement of thermal transport in suspended carbon nanotubes," *Applied Physics Letters,* vol. 92, p. 063119, Feb 11 2008.

[24] V. V. Deshpande, S. Hsieh, A. W. Bushmaker, M. Bockrath, and S. B. Cronin, "Spatially Resolved Temperature Measurements of Electrically Heated Carbon Nanotubes," *Physical Review Letters,* vol. 102, pp. 105501-4, 2009.

[25] Y. Ouyang and J. Guo, "Heat dissipation in carbon nanotube transistors," *Applied Physics Letters,* vol. 89, p. 183122, Oct 30 2006.

[26] F. Xiong, A. Liao, and E. Pop, "Inducing chalcogenide phase change with ultranarrow carbon nanotube heaters," *Applied Physics Letters,* vol. 95, p. 243103, 2009.

[27] L. Shi, J. H. Zhou, P. Kim, A. Bachtold, A. Majumdar, and P. L. McEuen, "Thermal probing of energy dissipation in current-carrying carbon nanotubes," *J. Appl. Phys.,* vol. 105, p. 104306, May 15 2009.

[28] E. T. Swartz and R. O. Pohl, "Thermal boundary resistance," *Reviews of Modern Physics,* vol. 61, p. 605, 1989.

[29] R. Prasher, "Thermal boundary resistance and thermal conductivity of multiwalled carbon nanotubes," *Physical Review B,* vol. 77, p. 075424, Feb 2008.

[30] J. C. Duda, J. L. Smoyer, P. M. Norris, and P. E. Hopkins, "Extension of the diffuse mismatch model for thermal boundary conductance between isotropic and anisotropic materials," *Appl. Phys. Lett.,* vol. 95, p. 031912, Jul 20 2009.

[31] P. E. Hopkins, "Multiple phonon processes contributing to inelastic scattering during thermal boundary conductance at solid interfaces," *Journal of Applied Physics,* vol. 106, p. 013528, Jul 1 2009.

[32] P. Reddy, K. Castelino, and A. Majumdar, "Diffuse mismatch model of thermal boundary conductance using exact phonon dispersion," *Applied Physics Letters,* vol. 87, p. 211908, Nov 21 2005.

[33] G. D. Mahan and G. S. Jeon, "Flexure modes in carbon nanotubes," *Physical Review B,* vol. 70, p. 075405, Aug 2004.

[34] P. G. Sverdrup, Y. S. Ju, and K. E. Goodson, "Sub-continuum simulations of heat conduction in silicon-on-insulator transistors," *Journal of Heat Transfer,* vol. 123, pp. 130-137, Feb 2001.

[35] K. Sun, M. A. Stroscio, and M. Dutta, "Graphite C-axis thermal conductivity," *Superlattices and Microstructures,* vol. 45, pp. 60-64, Feb 2009.

[36] R. Prasher, T. Tong, and A. Majumdar, "An acoustic and dimensional mismatch model for thermal boundary conductance between a vertical mesoscopic nanowire/nanotube and a bulk substrate," *Journal of Applied Physics,* vol. 102, p. 104312, Nov 2007.

[37] F. P. Incropera and D. P. DeWitt, *Fundamentals of Heat and Mass Transfer*, 5th ed. New York: Wiley, 2001.

[38] D. Mann, E. Pop, J. Cao, Q. Wang, and K. Goodson, "Thermally and Molecularly Stimulated Relaxation of Hot Phonons in Suspended Carbon Nanotubes," *Journal of Physical Chemistry B,* vol. 110, pp. 1502-1505, 2006.

[39] T. Hertel, R. E. Walkup, and P. Avouris, "Deformation of carbon nanotubes by surface van der Waals forces," *Physical Review B,* vol. 58, pp. 13870-13873, Nov 15 1998.

[40] S. Zhang, R. Khare, T. Belytschko, K. J. Hsia, S. L. Mielke, and G. C. Schatz, "Transition states and minimum energy pathways for the collapse of carbon nanotubes," *Physical Review B,* vol. 73, p. 075423, 2006.

[41] A. K. Rappe, C. J. Casewit, K. S. Colwell, W. A. Goddard, and W. M. Skiff, "Uff, a Full Periodic-Table Force-Field for Molecular Mechanics and Molecular-Dynamics Simulations," *Journal of the American Chemical Society,* vol. 114, pp. 10024-10035, Dec 2 1992.

[42] D. W. Brenner, "Empirical potential for hydrocarbons for use in simulating the chemical vapor deposition of diamond films," *Physical Review B,* vol. 42, p. 9458, 1990.

[43] B. Chen, M. Gao, J. M. Zuo, S. Qu, B. Liu, and Y. Huang, "Binding energy of parallel carbon nanotubes," *Appl. Phys. Lett.,* vol. 83, pp. 3570-3571, Oct 27 2003.

[44] H. Maune, H. Y. Chiu, and M. Bockrath, "Thermal resistance of the nanoscale constrictions between carbon nanotubes and solid substrates," *Applied Physics Letters,* vol. 89, p. 013109, Jul 3 2006.

[45] Z. Chen, W. Jang, W. Bao, C. N. Lau, and C. Dames, "Thermal contact resistance between graphene and silicon dioxide," *Appl. Phys. Lett.,* vol. 95, p. 161910 Oct 19 2009.

[46] A. G. Petrov and S. V. Rotkin, "Energy relaxation of hot carriers in single-wall carbon nanotubes by surface optical phonons of the substrate," *JETP Letters,* vol. 84, pp. 156-160, Oct 2006.

[47] S. V. Rotkin, V. Perebeinos, A. G. Petrov, and P. Avouris, "An Essential Mechanism of Heat Dissipation in Carbon Nanotube Electronics," *Nano Letters,* vol. 9, pp. 1850-1855, May 2009.

CHAPTER 4

THERMALLY-LIMITED CURRENT CARRYING ABILITY OF GRAPHENE NANORIBBONS

4.1 Introduction

Graphene nanoribbons (GNRs) are promising materials for nanoelectronics [1, 2]; however, many unknowns persist about their electrical and thermal properties. Among these, the maximum current density of GNRs is important both for fundamental and practical reasons: it is relevant to know what its limiting mechanisms are, how it compares to carbon nanotubes (CNTs), and to determine the maximum load a GNR transistor could drive within a circuit. By comparison, the current in single-wall CNTs is limited to tens of microamperes in diffusive transport due to self-heating and optical phonon scattering [3, 4], although larger currents can be achieved in short quasi-ballistic samples [5], under ambipolar transport [6], or under avalanche conditions [7]. However, GNRs differ from CNTs in two key aspects: first, they have edges which can cause significant scattering, affecting both electrical and thermal transport [1, 8]. Second, they lie flat on the substrate, which increases their heat dissipation compared to CNTs [9, 10] and can lead to lesser heat-limited current degradation. Nevertheless, to date no studies exist on the maximum current density of GNRs, or their dissipative behavior under high-field transport.

Here, we study the current carrying ability of GNRs on SiO_2 up to breakdown, and uncover key roles of heat dissipation both along and perpendicular to the device. We measure current densities up to ~3 mA/μm in ~15 nm wide GNRs, exceeding those typically available in silicon devices. However, the maximum current of GNRs is limited by the high temperature they achieve through Joule self-heating. The high-field behavior and breakdown of GNRs is also sensitive to their thermal conductivity (TC), which enables an extraction of this key parameter.

This chapter is reprinted from A. D. Liao, J. Z. Wu, X. R. Wang, K. Tahy, D. Jena, H. J. Dai, and E. Pop, "Thermally Limited Current Carrying Ability of Graphene Nanoribbons," *Physical Review Letters,* vol. 106, p. 256801, Jun 20 2011. Copyright 2011, American Physical Society.

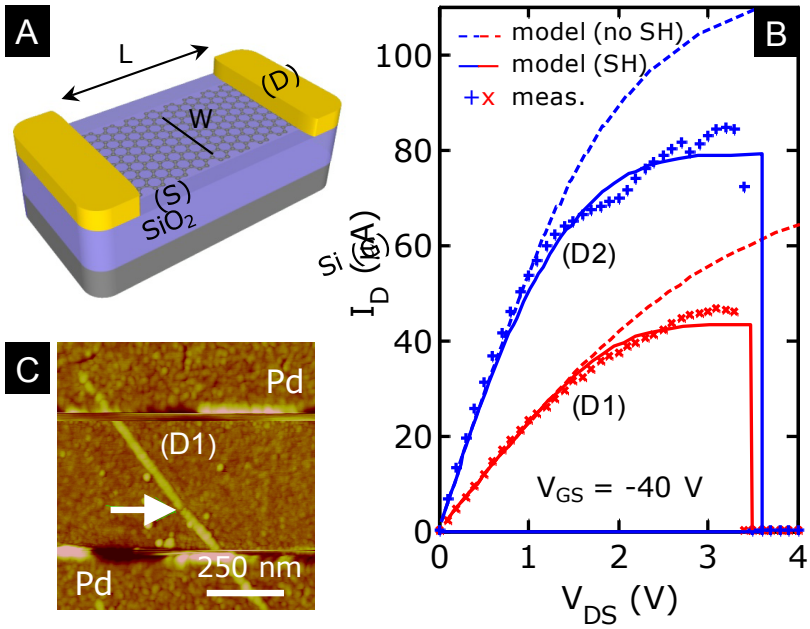

Fig. 4.1 (A) Schematic of graphene devices used in this work. (B) Measured (symbols) and simulated (lines) current-voltage up to breakdown of GNRs in air. Solid lines are model with self-heating (SH) and breakdown when max(T) > T_{BD} = 873 K, dashed lines are isothermal model without SH. Dimensions are L/W = 510/20 nm for D1, and L/W = 390/38 nm for D2. V_{GS} = -40 V to limit hysteresis effects. (C) Atomic force microscopy (AFM) image of D1 after high-current sweep; arrow shows breakdown location.

4.2 Fabrication and Measurements

GNR devices as shown in Fig. 4.1 were fabricated from solution-deposited GNRs [11]. For comparison, larger exfoliated graphene (XG) samples were also created, with dimensions defined by oxygen plasma pattering. Both types of samples were placed on SiO_2 (t_{ox} = 300 nm)/Si substrates, with Si also serving as the back-gate (G). Source (S) and drain (D) electrodes were made with Pd (20 nm) for GNRs and Cr/Au (2/200 nm) for XG devices. GNRs had widths ranging from W = 16-90 nm and lengths L = 0.2-0.7 μm. XG devices had W = 0.1-2.6 μm and lengths L = 3.9-9.7 μm.

Graphene nanoribbon (GNR) devices were obtained from a 1,2-dichloroethane organic solution of poly(m-phenylenevinylene-co-2,5-dioctoxy-p-phenylenevinylene) (PmPV) by sonication of pristine multiwall nanotubes (MWNTs) that had been calcined at 650 °C [11]. An ultracentrifuge step was performed to remove the remaining nanotubes, following the method described by Jiao et al. [11]. The solution was spin coated onto ~300 nm SiO_2 substrates on highly doped silicon wafers. After calcination of the coated substrate at 275 °C for 20 minutes to remove the remaining PmPV, an array of 20 nm thick Pd elec-

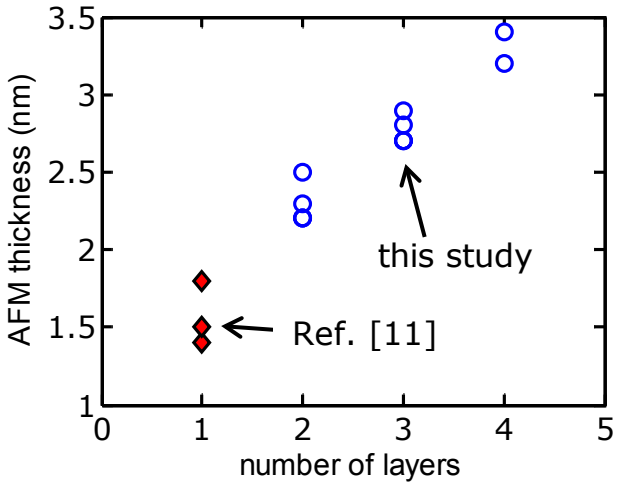

Figure 4.2. Measured AFM thickness of GNR samples vs. number of layers assigned. GNRs that correspond to this study are represented with open circles and ones from Ref. [11] in filled diamonds.

trodes and pads were defined by e-beam evaporation and lift-off. The contacts were annealed in Ar at 200 ^{o}C after which the devices were then annealed electrically. Samples were characterized by atomic force microscopy (AFM) and electrical testing to determine which of electrode pairs correspond to valid devices. Such devices consist primarily of non-AB stacked 2-layer GNRs; however, some layer variation is seen in Fig. 4.2 and is characterized below.

As the GNRs are fabricated from multiwalled carbon nanotubes, the layer stacking orientation is random, unlike that of bulk graphite. Thus we cannot use Raman spectroscopy to count the number of layers. Instead we rely on the measured thickness from AFM scans to distinguish the number of layers of graphene, as shown in Figure 4.2. We note that numerical values from AFM scans are used only for counting layers and not in our calculations, because they are not an accurate measurement of the real thickness. The actual thickness that is used in calculations is the number of layers times the inter-atomic spacing between graphene sheets (0.34 nm). We also note that AFM images of ribbons and sheets show similar heights for similar layer numbers.

For comparison, micron-sized exfoliated graphene (XG) devices from Graphene Industries were deposited on heavily n-type doped silicon wafers, also with ~300 nm thermal oxide. XG devices were identified using optical and Raman microscopy. The wafers were backside-metalized after oxide removal in HF to form back-gate contacts. The graphene flakes were then patterned using an O_2 plasma reactive ion etch with PMMA

masks. E-beam evaporated Cr/Au (2/200 nm) was used to define the drain and source contacts by e-beam lithography. After metal deposition and lift-off, the samples were annealed in forming gas at ~400 °C for ~2 hours to remove the e-beam resist residue.

To study the upper limits of high-field transport, we measure I_D–V_{DS} until devices break from Joule self-heating, as shown in Fig. 4.1B. This is similar to the breakdown thermometry technique previously applied to CNTs [10, 12] and nanowires [13]. Like with CNTs, the current drops sharply to zero, creating a small gap in the GNR as imaged in Fig. 4.1C. Measurements were made in ambient air, where breakdown (BD) occurs by oxidation at $T_{BD} \approx 600\ ^{o}C$ [10]. By comparison, breakdown of control samples in vacuum (~7×10^{-6} Torr) occurred at six times higher power, suggesting other failure mechanisms such as defect formation, SiO_2 damage [10], or even GNR melting (known to occur at ~3600 ^{o}C).

4.3 Modeling and Data Analysis

4.3.1 Current Modeling

An existing graphene model [14, 15] was adapted for GNRs, calculating I_D as a function of applied V_{GS}, V_{DS} and temperature T under diffusive transport conditions:

$$I_D = qWV_{DS}\left[\int_0^L \frac{F_x}{n(V_{Gx},T_x)\cdot v_d(F_x,T_x)}dx\right]^{-1} \tag{4.1}$$

where q is the elementary charge, x is the coordinate along the graphene channel, n is the total carrier density at location x, $V_{Gx} = V_G - V_x$ is the potential between gate and location x, $F_x = -dV_x/dx$ is the electric field, and v_d is the drift velocity including saturation and temperature effects as in Ref. [15]. The current in equation (4.1) is solved self-consistently with the Poisson equation and the heat equation along the GNR [14], both including 3-dimensional (3D) fringing effects in the capacitance and substrate heat dissipation [g in equation (4.3) below].

To obtain the current-voltage calculations displayed in Fig. 4.1B, we extended a previously developed graphene finite-element simulation [14, 15]. Modifications include a lower mobility, as is typical of such GNRs [2], $\mu_{0,1} = 160\ cm^2V^{-1}s^{-1}$ for D1 and

$\mu_{0,2}$ = 280 $cm^2V^{-1}s^{-1}$ for D2. A contact resistance R_CW = 250 Ω·μm was used for both devices.

To model the high-field and temperature-dependent behavior we used the velocity saturation model in [15]. The temperature dependence of mobility used was $\mu(T) = \mu_0(300/T)^{1/2}$, similar to carbon nanotubes [16], but slightly weaker than in 'large' graphene on SiO_2 [15]. We note that decisive temperature-dependent mobility data are not yet available for GNRs, and it is likely these would change from sample to sample due to variation in impurity and edge scattering. However, weaker temperature dependence of mobility in GNRs is reasonably expected, as similarly observed in metal nanowires vs. bulk metals [17]. Regardless, as it turns out, the specific mobility model has less impact on the high-field behavior of GNRs, which is dominated by the high-field saturation velocity, including its carrier density and temperature dependence [15].

To calculate the charge density along the GNR we use the approach in Ref. [15], but here we must include fringing effects in the capacitance of the GNR above the Si backgate. The GNR capacitance per unit area is:

$$C_{ox} = \varepsilon_{ox}\varepsilon_0\left\{\frac{\pi}{\ln\left[6\left(t_{ox}/W+1\right)\right]W}+\frac{1}{t_{ox}}\right\} \tag{4.2}$$

where the first term represents the fringing capacitance and the second term is the parallel plate capacitance of the GNR. The expression reduces to the familiar $C_{ox} = \epsilon_{ox}\epsilon_0/t_{ox}$ (in Farads per unit area) in the limit $W \to \infty$ as expected for large graphene, and is in g ood agreement with finite-element simulations [18].

The temperature along the GNR was computed iteratively with the finite-element method described in Ref. [14], using k_1 = 100 $Wm^{-1}K^{-1}$ and k_2 = 175 $Wm^{-1}K^{-1}$, scaled consistently with the mobility of the two GNRs, and consistent with thermal conductivity values extracted in the overall study.

Simulated I_D–V_{DS} curves and breakdown voltages in Fig. 4.1B are in good agreement with the experimental data when self-heating (SH) is enabled in the model (solid lines). Without SH the simulated currents are much higher and breakdown is not observed as the temperature remains unchanged.

4.3.2 Power Dissipatoin

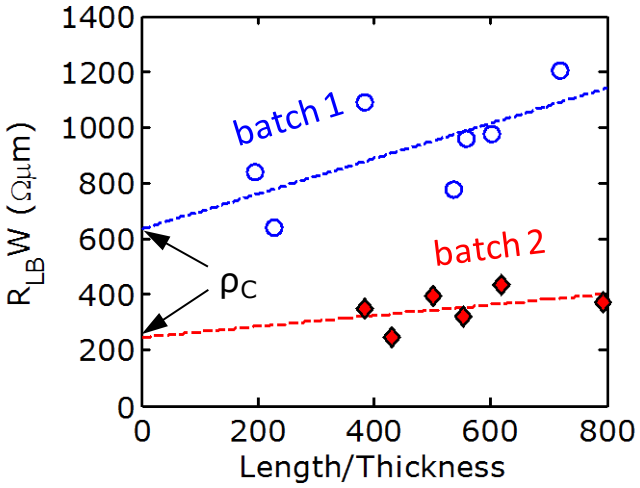

Fig. 4.3. Measured low-bias resistance (R_{LB}) times width vs. length/thickness ratio of the GNRs. The y-intercept is the average contact resistance times width. Two fabrication batches yielded different contacts.

To gain more physical insight into the scaling of SH in such devices, we consider the power dissipation at breakdown, $P_{BD} = I_{BD}(V_{BD} - I_{BD}R_C)$ [10], where R_C is the electrical contact resistance, and I_{BD} and V_{BD} are the current and voltage at breakdown, respectively. We subtract the power dissipated at the contacts (I^2R_C, where R_C is the contact resistance) from the total power measured, to obtain only the power dissipated within the graphene. Because the GNR test structures had two terminals, an indirect method of extracting R_C was employed. Measuring the low bias (LB) resistance, which depends geometrically on the sheet and contact resistance [19], we fit the following expression to our data:

$$R_{LB} = \frac{\rho_C}{W} + \frac{\rho_S L}{Wt} \tag{4.3}$$

Here R_{LB} is the low bias resistance taken from the linear region of the I_D-V_{DS} measurement, ρ_C is the contact resistivity, ρ_S is the sheet resistivity of graphene, L is the length, W is the width, and t is the thickness of the sample. All measurements were performed at V_{GS} = -40 V back-gate bias, which eliminates hysteresis effects. We find that variations arising from fabrication have a notable impact on the values extracted when comparing two different batches of devices shown in Fig. 4.3. A fit to the data from a given batch is made using eq. (4.1) (dashed lines) and an average contact resistance is extracted. The average contact resistivity for batch 1 is $\rho_C = R_C W \sim 630$ Ω·μm and for batch 2 $\rho_C = R_C W \sim 250$ Ω·μm; both values are typical for graphene-Pd contacts, and

within experimental variation observed by us and other groups. From this, we also obtain the sheet resistance (ρ_S/t).

We plot P_{BD} vs. the square root of the device channel area in Fig. 4.4A. To understand the scaling trend observed, we compare the experimental results with the analytic solution of the heat equation along the graphene devices, similar to CNTs [20]:

$$P_{BD} = gL\left(T_{BD} - T_0\right)\left[\frac{\cosh\left(L/2L_H\right) + gL_H R_T \sinh\left(L/2L_H\right)}{\cosh\left(L/2L_H\right) + gL_H R_T \sinh\left(L/2L_H\right) - 1}\right] \tag{4.4}$$

where T_0 is the ambient temperature, L_H is the thermal healing length along the device and g is the thermal conductance to substrate per unit length [equation (4.5) below]. The thermal resistance at the metal contacts is $R_T = L_{Hm}/[k_m t_m(W + 2L_{Hm})]$. Here t_m is the thickness and $k_m \approx 22$ $Wm^{-1}K^{-1}$ is the TC of the metal electrodes (estimated with the Wiedemann-Franz law [21] using their measured resistivity), and L_{Hm} is the thermal healing length of heat spreading into the metal contacts. The two healing lengths are $L_H = (kWt/g)^{1/2}$ and $L_{Hm} = [t_m t_{ox} k_m/k_{ox}]^{1/2}$, both of the order ~0.1 μm here. The TC of SiO_2 $k_{ox} = 1.3$ $Wm^{-1}K^{-1}$, while t is the thickness and k the TC of the graphene.

The heat loss coefficient into the substrate is written as:

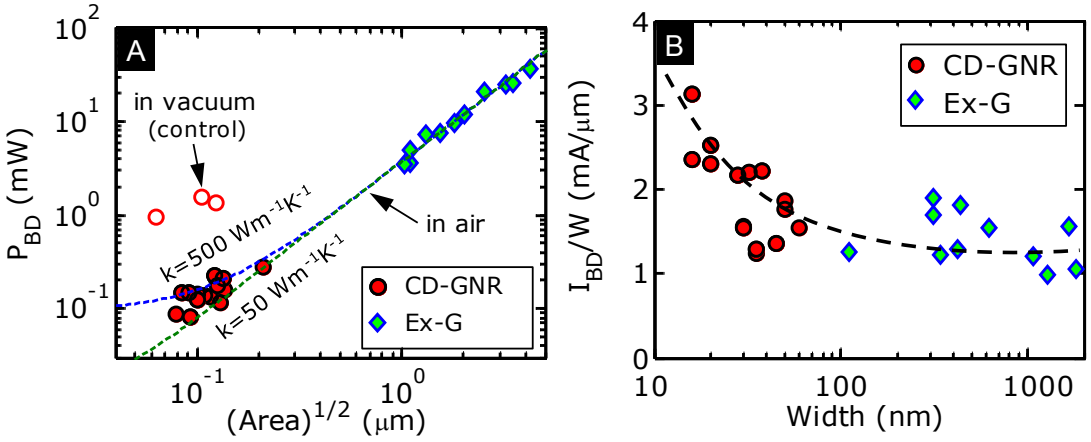

Fig. 4.4 (A) Scaling of GNR and XG breakdown power with square root of device footprint, $(WL)^{1/2}$. Dashed lines are thermal model with $k = 50$ and 500 $Wm^{-1}K^{-1}$, $R_{Cox} = 5\times10^{-8}$ m^2KW^{-1} and $L/W = 15$. Lateral heat sinking and in-plane GNR thermal conductivity begin to play a role in devices < ~0.3 μm (also see Fig. 4.5). A few devices were broken in vacuum as a control group. (B) Scaling of peak current at breakdown vs. device width, demonstrating greater current density in narrower GNRs that benefit from 3D heat spreading and lateral heat flow along the GNR. Dashed line drawn to guide the eye.

$$g^{-1} = \left\{ \frac{\pi k_{ox}}{\ln\left[6\left(t_{ox}/W + 1\right)\right]} + \frac{k_{ox}}{t_{ox}} W \right\}^{-1} + \frac{R_{Cox}}{W} \tag{4.5}$$

and consists of the series combination of the thermal resistance at the graphene/SiO_2 interface, R_{Cox} [9, 22, 23], and the 3D spreading thermal resistance into the SiO_2 written here as an analytic fit to detailed finite element simulations.

The two dashed lines in Fig. 4.4A show the predictions of the model for k = 50 and 500 $Wm^{-1}K^{-1}$. We note that for device dimensions $(WL)^{1/2} \gg 0.3$ μm, or approximately three times the healing length, heat dissipation is essentially independent of heat flow along the graphene, and thus on its TC. As a result, dissipation in larger devices made with exfoliated graphene (XG) in Fig. 4.4 can also be estimated with the simplified approach in Ref. [15]. However for GNRs with dimensions $\leq 3L_H$, heat dissipation occurs in part along the GNR, and this observation is used below to extract their TC. In Fig. 4.4B we plot the maximum current density I_{BD} per width W at the breakdown point (temperature ~T_{BD}), and find it can reach over 3 mA/μm for the narrowest GNRs. This current density appears to scale inversely with width which, at first sight, is a counterintuitive finding compared to silicon devices. This also appears at odds with the present understanding that GNRs have significantly lower mobility than large-area graphene [2].

We suggest that GNRs can dissipate more power and thus carry higher current density *at a given temperature* (here, breakdown temperature T_{BD}), consistent with a significant role of 3D heat spreading [9]. Figures 4.5A and B display the total device thermal conductance per unit area $G'' = P_{BD}/(T_{BD} - T_0)/(WL)$ obtained from the experiments (symbols) and the analytic model from equation (4.4) (solid lines). We note that for a given device the maximum power (and current) at breakdown are proportional to G''. Similar to Fig. 4.4B, we find that both the experimental data and our model scale inversely with the GNR width. To gain a physical understanding of these trends, we consider the heat spreading schematics in Figs. 4.5C-E. For 'large' graphene in Fig. 4.5C, dissipation occurs mainly 'down' into the oxide. Thus, $G'' = 1/(R_{Cox} + t_{ox}/k_{ox})$ is independent of device dimensions when $L,W \rightarrow \infty$ [in practice $(LW)^{1/2} \gg 3L_H$], as shown with dash-dotted line in Figs. 4.5A and B. In general, this expression may include a small heat spreading term into the Si wafer [9, 15], which was negligible here. For large graphene devices the constant expression is also recovered as $G'' = g/W$ when taking the limit $W \rightarrow \infty$ of equa-

tion (4.5).

In contrast, for 'narrow' GNRs the lateral 3D heat spreading into the SiO_2 becomes a significant component of the overall thermal conductance of a device [Fig. 4.5D]. In addition, for 'short' devices some heat is conducted along the graphene and into the contacts as well [Fig.4.5E]. The amount of heat carried out in this manner will depend on the TC and length of the device. The three solid lines in Fig. 4.5A show what the modeled *G"* predicts for $k = 50$, 250, and 500 $Wm^{-1}K^{-1}$. As the TC increases, heat is carried more efficiently along the GNR. The device length also matters for 'short' GNRs with $L \leq 3L_H$, when heat generated within the graphene channel is sunk more effectively into the contacts [20]. As a result, the thermal conductance *G"* increases as *L* decreases in Fig. 4.5B. In both cases, as the heat dissipation increases, we also see an increase in device current density as plotted in Fig. 4.4B, thus confirming that Joule self-heating is a key current

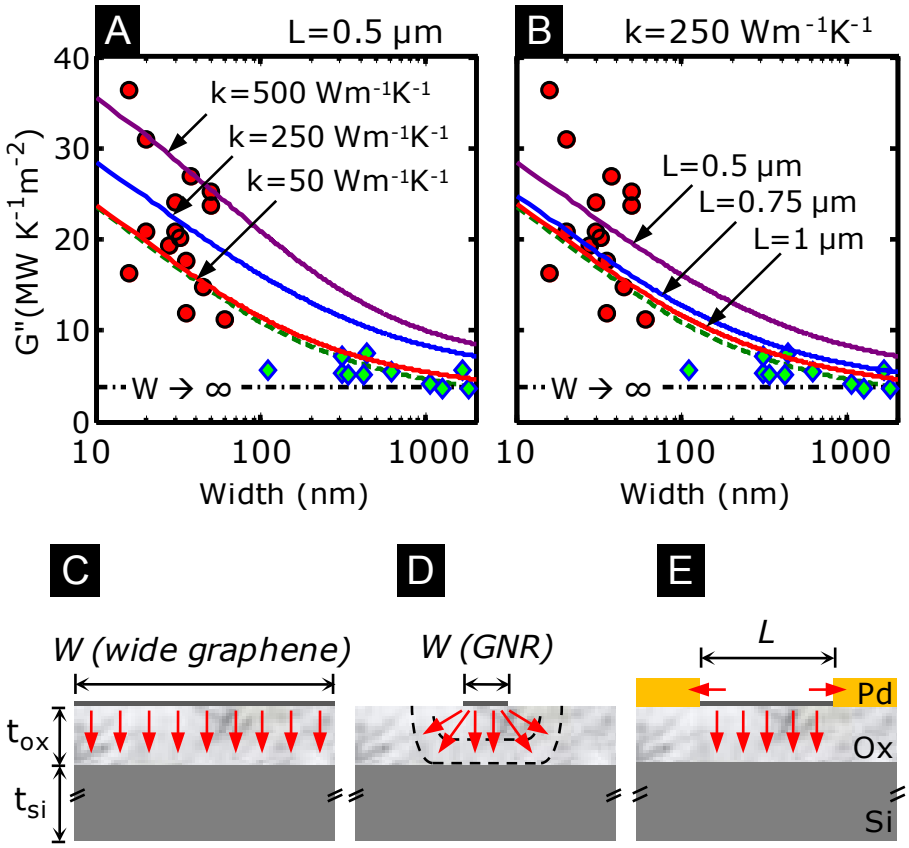

Fig. 4.5 Thermal conductance of device per unit area (*G"*) vs. width for graphene of varying (A) thermal conductivity and (B) length. Both parameters affect heat sinking along GNRs < ~0.3 μm. Symbols follow the notation of Fig. 4.4. Horizontal dash-dotted line is the limit $W \rightarrow \infty$ which applies to the case in (C), only "vertical" heat sinking through the oxide. The significance of lateral heat spreading from GNRs is shown in (D) and (E), both mechanisms partly leading to higher current density in Fig. 4.4.

limiter in GNR devices.

4.3.3 Thermal Conductivity

Since heat dissipation is sensitive to heat flow along 'short' GNRs, it is possible to extract their TC, as shown in Fig. 4.6. To accomplish this, we iteratively vary k within L_H in eq. (2) until the predicted breakdown power matches the measurements, for each device (we assume a unique k for each GNR). To estimate the confidence intervals of extracted TC for our GNRs, we consider a range R_{Cox} = 1–5 × 10^{-8} m^2K/W for the graphene/SiO_2 interface thermal resistance [22-24], and an uncertainty of ±1 layer in the GNR thickness. The extracted TC along with data from the literature on 'large' graphene

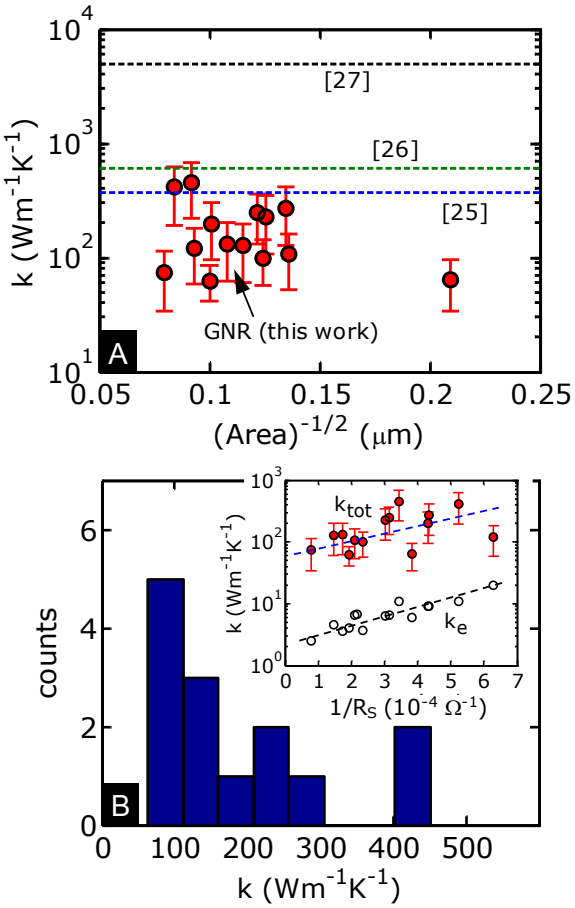

Fig. 4.6 (A) Thermal conductivity (TC) of GNRs from this work, compared to large-area graphene measurements from the literature [25-27]. (B) Histogram of TC for our GNRs shows a range 63–450 $Wm^{-1}K^{-1}$ with a median of 130 $Wm^{-1}K^{-1}$ at the breakdown temperature (600 °C). The median TC at room temperature is ~40% lower, or ~80 $Wm^{-1}K^{-1}$, nearly an order of magnitude lower than 'large' exfoliated graphene (XG) on a substrate [26]. The inset shows approximate scaling between TC and electrical sheet conductance, suggesting scattering mechanisms common to both electrons and phonons. The electronic contribution to thermal conductivity (k_e) is estimated with the Wiedemann-Franz law to be typically <10 $Wm^{-1}K^{-1}$ or <10%. Dashed lines guide the eye.

[25-27] are displayed in Fig. 4.6A. We find a TC range k = 63-450 $Wm^{-1}K^{-1}$ for our GNRs, as summarized in the histogram of Fig. 4.6B, with a median ~130 $Wm^{-1}K^{-1}$ (at the T_{BD} = 600 ^{o}C), or ~80 $Wm^{-1}K^{-1}$ at 20 ^{o}C, nearly an order of magnitude lower than the TC of exfoliated graphene on SiO_2 [26]. The room temperature estimate is done by assuming a mean free path that is independent of temperature (limited by edge or defect scattering), and considering only the temperature variation of graphene heat capacity [10]. Given that we observe no clear dependence of TC on GNR size (i.e. no size effect) in Fig. 4.6A, we surmise that here the TC is limited by edge roughness and defect or impurity scattering. However, the *range* of values extracted can be attributed to *variations* in edge roughness and defect or impurity density between samples. For instance, recent scanning tunneling microscopy (STM) studies [28] have found that edges of such GNRs vary from atomically smooth to ~1 nm edge roughness. Simulations [8, 29] suggest that edge disorder could nearly account for the variation in TC observed in Fig. 4.6, while different impurity or defect density between samples will only serve to broaden the observed distribution.

Before concluding, we examine if the thermal and electrical properties of the GNRs are related, and plot the extracted TC vs. the inverse sheet resistance in the Fig. 4B inset. Also plotted is the electronic contribution to TC (k_e), estimated with the Wiedemann-Franz law [21] to be nearly always an order of magnitude lower (< 10 $Wm^{-1}K^{-1}$). This estimate is likely an upper limit, as the Lorenz number ($L_0 = 2.45\times10^{-8}$ $W\Omega K^{-2}$) in graphite is unchanged [30], but in nanostructures where edge scattering dominates it is slightly lower than the bulk value [31]. This simple analysis suggests that TC of GNRs is dominated by phonons at room temperature and above. However, TC and electrical conductance follow similar trends here, indicating that similar scattering mechanisms limit both phonon and electron transport. These scatterers include edges, impurities and defects in GNRs [2, 8, 29, 32].

4.4 Conclusions

In conclusion, we have shown that high-field transport in GNRs on SiO_2 is limited by self-heating. The maximum current density at a given temperature scales inversely with GNR width and reaches >3 mA/μm in ~15 nm wide devices. Dissipation in 'large' graphene (≫0.3 μm, or three times the thermal healing length) is limited primarily by the SiO_2 thickness, but dissipation in 'small' GNRs improves from 3D heat spreading into the SiO_2 and heat flow along the GNR to the contacts. Taking advantage of this sensitivity we found a median TC ~ 80 $Wm^{-1}K^{-1}$ for GNRs at room temperature, with less than 10% electronic contribution.

4.5 References

[1] A. Cresti, N. Nemec, B. Biel, G. Niebler, F. Triozon, G. Cuniberti, and S. Roche, "Charge transport in disordered graphene-based low dimensional materials," *Nano Research,* vol. 1, pp. 361-394, 2008.

[2] X. Wang, Y. Ouyang, X. Li, H. Wang, J. Guo, and H. Dai, "Room-temperature all-semiconducting sub-10-nm graphene nanoribbon field-effect transistors," *Physical Review Letters,* vol. 100, p. 206803, May 23 2008.

[3] M. Lazzeri and F. Mauri, "Coupled dynamics of electrons and phonons in metallic nanotubes: Current saturation from hot-phonon generation," *Physical Review B,* vol. 73, p. 165419, 2006.

[4] E. Pop, D. A. Mann, K. E. Goodson, and H. J. Dai, "Electrical and thermal transport in metallic single-wall carbon nanotubes on insulating substrates," *Journal of Applied Physics,* vol. 101, p. 093710, May 2007.

[5] A. Javey, J. Guo, M. Paulsson, Q. Wang, D. Mann, M. Lundstrom, and H. J. Dai, "High-field quasiballistic transport in short carbon nanotubes," *Physical Review Letters,* vol. 92, p. 106804, 2004.

[6] Y. F. Chen and M. S. Fuhrer, "Electric-field-dependent charge-carrier velocity in semiconducting carbon nanotubes," *Physical Review Letters,* vol. 95, p. 236803, Dec 2 2005.

[7] A. Liao, Y. Zhao, and E. Pop, "Avalanche-Induced Current Enhancement in Semiconducting Carbon Nanotubes," *Physical Review Letters,* vol. 101, p. 256804, Dec 19 2008.

[8] W. Li, H. Sevincli, G. Cuniberti, and S. Roche, "Phonon transport in large scale carbon-based disordered materials: Implementation of an efficient order- N and real-space Kubo methodology," *Physical Review B,* vol. 82, p. 041410, 2010.

[9] E. Pop, "Energy Dissipation and Transport in Nanoscale Devices," *Nano Research,* vol. 3, pp. 147-169, Mar 2010.

[10] A. Liao, R. Alizadegan, Z.-Y. Ong, S. Dutta, F. Xiong, K. J. Hsia, and E. Pop, "Thermal dissipation and variability in electrical breakdown of carbon nanotube devices," *Physical Review B,* vol. 82, p. 205406, 2010.

[11] L. Jiao, X. Wang, G. Diankov, H. Wang, and H. Dai, "Facile synthesis of high-quality graphene nanoribbons," *Nature Nanotechnology,* vol. 5, pp. 321-325, May 2010.

[12] H. Y. Chiu, V. V. Deshpande, H. W. C. Postma, C. N. Lau, C. Miko, L. Forro, and M. Bockrath, "Ballistic phonon thermal transport in multiwalled carbon nanotubes," *Physical Review Letters,* vol. 95, p. 226101, Nov 25 2005.

[13] A. M. Katzenmeyer, F. Leonard, A. A. Talin, M. E. Toimil-Molares, J. G. Cederberg, J. Y. Huang, and J. L. Lensch-Falk, "Observation of Space-Charge-Limited Transport in InAs Nanowires," *IEEE Transactions on Nanotechnology,* vol. 10, pp. 92-95, 2011.

[14] M.-H. Bae, Z.-Y. Ong, D. Estrada, and E. Pop, "Imaging, Simulation, and Electrostatic Control of Power Dissipation in Graphene Devices," *Nano Letters,* vol. 10, pp. 4787-4793, 2010.

[15] V. E. Dorgan, M.-H. Bae, and E. Pop, "Mobility and saturation velocity in graphene on SiO_2," *Applied Physics Letters,* vol. 97, pp. 082112-3, 2010.

[16] Y. Zhao, A. Liao, and E. Pop, "Multiband Mobility in Semiconducting Carbon Nanotubes," *IEEE Electron Device Letters,* vol. 30, p. 1078, 2009.

[17] W. Steinhögl, G. Schindler, G. Steinlesberger, M. Traving, and M. Engelhardt, "Comprehensive study of the resistivity of copper wires with lateral dimensions of 100 nm and smaller," *Journal of Applied Physics,* vol. 97, pp. 023706-7, 2005.

[18] C. Lian, K. Tahy, T. Fang, G. Li, H. G. Xing, and D. Jena, "Quantum transport in graphene nanoribbons patterned by metal masks," *Applied Physics Letters,* vol. 96, p. 103109, 2010.

[19] A. Venugopal, L. Colombo, and E. M. Vogel, "Contact resistance in few and multilayer graphene devices," *Applied Physics Letters,* vol. 96, pp. 013512-3, Jan 8 2010.

[20] E. Pop, "The role of electrical and thermal contact resistance for Joule breakdown of single-wall carbon nanotubes," *Nanotechnology,* vol. 19, p. 295202, July 2008.

[21] C. Kittel, *Introduction to Solid State Physics*, 8 ed. Hoboken, NJ: John Wiley & Sons, 2005.

[22] Z. Chen, W. Jang, W. Bao, C. N. Lau, and C. Dames, "Thermal contact resistance between graphene and silicon dioxide," *Applied Physics Letters,* vol. 95, p. 161910, Oct 19 2009.

[23] K. F. Mak, C. H. Lui, and T. F. Heinz, "Measurement of the thermal conductance of the graphene/SiO[sub 2] interface," *Applied Physics Letters,* vol. 97, pp. 221904-3, 2010.

[24] Y. K. Koh, M.-H. Bae, D. G. Cahill, and E. Pop, "Heat Conduction across Monolayer and Few-Layer Graphenes," *Nano Letters,* vol. 10, pp. 4363-4368, 2010.

[25] W. Cai, A. L. Moore, Y. Zhu, X. Li, S. Chen, L. Shi, and R. S. Ruoff, "Thermal Transport in Suspended and Supported Monolayer Graphene Grown by Chemical Vapor Deposition," *Nano Letters,* vol. 10, pp. 1645-1651, 2010.

[26] J. H. Seol, I. Jo, A. L. Moore, L. Lindsay, Z. H. Aitken, M. T. Pettes, X. S. Li, Z. Yao, R. Huang, D. Broido, N. Mingo, R. S. Ruoff, and L. Shi, "Two-Dimensional Phonon Transport in Supported Graphene," *Science,* vol. 328, pp. 213-216, Apr 9 2010.

[27] S. Ghosh, W. Z. Bao, D. L. Nika, S. Subrina, E. P. Pokatilov, C. N. Lau, and A. A. Balandin, "Dimensional crossover of thermal transport in few-layer graphene," *Nature Materials,* vol. 9, pp. 555-558, 2010.

[28] C. G. Tao, L. Y. Jiao, O. V. Yazyev, Y. C. Chen, J. J. Feng, X. W. Zhang, R. B. Capaz, J. M. Tour, A. Zettl, S. G. Louie, H. J. Dai, and M. F. Crommie, "Spatially resolving edge states of chiral graphene nanoribbons," *Nature Physics,* vol. 7, pp. 616-620, Aug 2011.

[29] A. V. Savin, Y. S. Kivshar, and B. Hu, "Suppression of thermal conductivity in graphene nanoribbons with rough edges," *Physical Review B,* vol. 82, p. 195422, 2010.

[30] M. G. Holland, C. A. Klein, and W. D. Straub, "The Lorenz number of graphite at very low temperatures," *J. Phys. Chem. Solids,* vol. 27, pp. 903-906, 1966.

[31] F. Völklein, H. Reith, T. W. Cornelius, M. Rauber, and R. Neumann, "The experimental investigation of thermal conductivity and the Wiedemann–Franz law for single metallic nanowires," *Nanotechnology,* vol. 20, p. 325706, 2009.

[32] T. Fang, A. Konar, H. Xing, and D. Jena, "Mobility in semiconducting graphene nanoribbons: Phonon, impurity, and edge roughness scattering," *Physical Review B,* vol. 78, p. 205403, 2008.

CHAPTER 5

AVALANCHE-INDUCED CURRENT ENHANCEMENT IN SEMICONDUCTING CARBON NANOTUBES

5.1 Current Enhancement in Carbon Nanotubes

While quasi-ballistic transport at submicron lengths [1] and low-field mobility in longer, diffusive samples [2] have been studied in great detail in carbon nanotubes, much is still unknown about diffusive transport at high fields (>1 V/μm). This regime sets the peak current-carrying ability, and provides a glimpse into the behavior under extreme electrical stress conditions. For instance, the maximum current of long *metallic* single-wall nanotubes (m-SWNTs) is 20–25 μA when limited by Joule heating and optical phonon scattering [3, 4], which appears to be exceeded only in submicron, quasi-ballistic samples [1]. The maximum current capacity of long *semiconducting* single-wall nanotubes (s-SWNTs) under diffusive transport is less established, although a 25 μA limit has been suggested for single-band conduction [5]. However, experimental data indicates this limit is exceeded under ambipolar transport [6], and theoretical estimates suggest this value can be surpassed when multiple subbands are involved [7].

Current vs. drain-source voltage (V_{DS}) measurements were made in air and vacuum. In air, metallic nanotubes saturate from self-heating and strong electron-phonon scattering [3] up to Joule breakdown, as previously discussed in Chapter 2. By contrast, most semiconducting tubes turned on at large $|V_{GS}|$ exhibit a sudden current increase before Joule breakdown. Additional measurements carried out in vacuum (~10^{-5} Torr) allow further study of the current up-kick without breaking the nanotubes by oxidation. It is important to note that devices were measured in the reverse bias regime, with $V_{GS} < 0 < V_{DS}$ and $|V_{GS}| > |V_{DS}|$ [7]. By contrast, in Schottky mid-gap contacted devices, the ambipolar regime $V_{DS} < V_{GS} < 0$ "splits" the potential drop along the nanotube, resulting in lower longitudinal electric fields [6-8] and transport by both electrons and holes. In the reverse

This chapter is reprinted from A. Liao, Y. Zhao, and E. Pop, "Avalanche-Induced Current Enhancement in Semiconducting Carbon Nanotubes," *Physical Review Letters,* vol. 101, p. 256804, Dec 19 2008. Copyright 2008, American Physical Society.

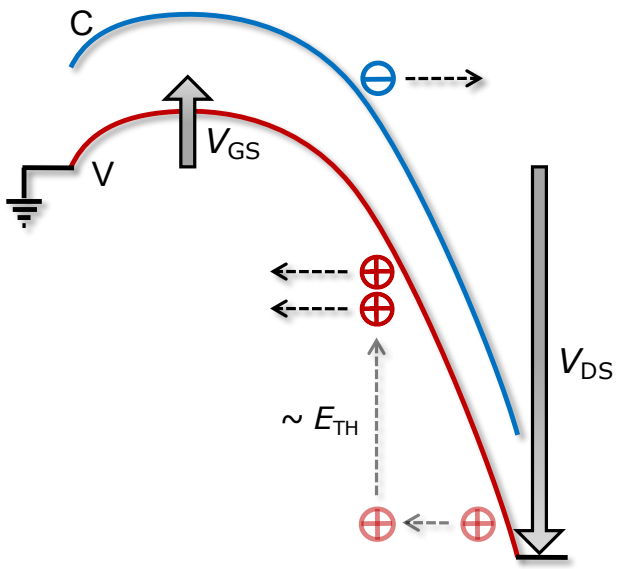

Fig. 5.1 Schematic band diagram of a carbon nanotube of EHP generation under reverse bias conditions.

bias regime, holes are the majority carriers in our s-SWNTs until the avalanche mechanism partially turns on the conduction band (Fig. 5.1).

At first glance, several mechanisms may be responsible for the current increase at very high fields in our s-SWNTs, all various forms of "soft" (reversible) breakdown [9]. These are Zener band-to-band (BB) tunneling, avalanche impact ionization (II), and thermal generation current. Under BB transport, electrons tunnel from the valence to the conduction band. The probability is evaluated as

$$P_{BB} \sim \exp\left(-\frac{E_G^2}{q\hbar v_F F}\right) \tag{5.1}$$

where E_G is the band gap (~0.84/d eV/nm), v_F is the Fermi velocity, and F is the electric field [10]. During avalanche II, holes gain high energy in the valence band, then lose it by creating electron-hole pairs (EHPs) as shown in Fig. 5.1. Inelastic optical phonon (OP) emission is the strongest process competing with II, given the large OP energy ($\hbar\omega_{OP}$ ~ 0.18 eV). The II probability is estimated as [11-13]

$$P_{II} \sim \exp\left(-\frac{E_{TH}}{q\lambda_{OP,ems}F}\right) \tag{5.2}$$

We take $\lambda_{OP,ems}$ ~ 14d nm as the spontaneous OP emission mean free path (MFP) by holes or electrons [13], and E_{TH} is the avalanche energy threshold. Comparing the two

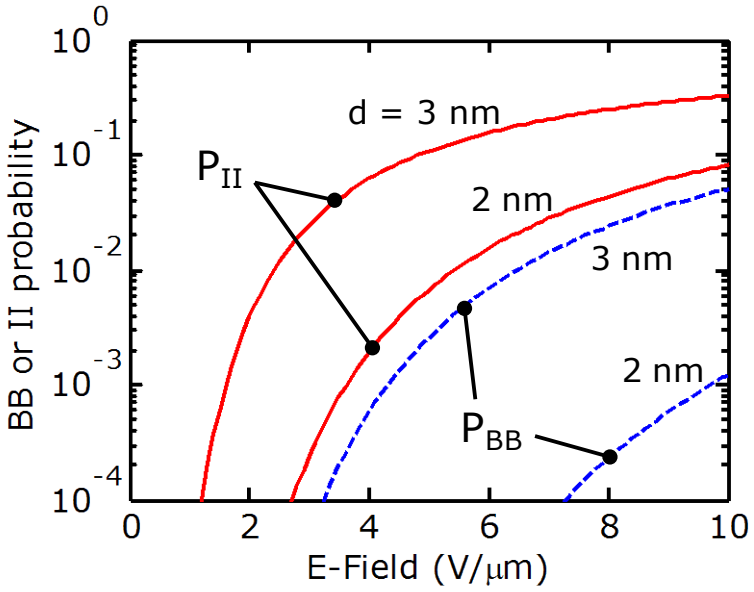

Fig. 5.2 Probability of impact ionization (II) and Zener band-to-band tunneling (BB) vs. electric field along the nanotube, for the diameters and field range of interest.

mechanisms in Fig. 5.2 suggests impact ionization is considerably more likely for the electric field and nanotube diameter range in this study. BB transport becomes important as a result of sudden spatial changes in electrostatic or chemical doping, leading to local fields of the order 100 V/μm (1 MV/cm) or higher [14, 15]. Thermal generation is experimentally investigated, and is also found to make a negligible contribution, as explored in more detail below.

Not all semiconducting nanotubes exhibit current up-kick at high fields. Previous work by Marty et al. has shown no current up-kick at high bias, but has instead detected radiative exiton recombination [16], which is a competing mechanism with II. This was reasonably attributed to direct exciton annihilation, rather than the avalanche generation of free carriers. By contrast, our nanotubes have ~2x larger diameters, thus approximately half the band separations and exciton binding energies, and ohmic Pd contacts rather than Schottky Co contacts. In addition, all our measurements were made in vacuum, allowing repeated study of the current up-kick, which was not always observable in air before Joule breakdown. While excitonic generation and recombination may play a role in our samples, we suggest that the current increase is possible because most free EHPs are generated in the high-field region within a few mean free paths (10-100 nm) of the drain. Thus, generated electrons are swept out into the electrode by the high field within 0.1-1

ps (Fig. 5.2), much faster than the recombination lifetimes (10-100 ps) [17]. In addition, the high temperatures and high fields in these conditions contribute significantly to exciton instability, despite their relatively high binding energy.

5.2 Impact Ionization in Carbon Nanotubes

Previous theoretical work has shown II in s-SWNTs is not possible until the third subband is occupied [13], due to angular momentum conservation as illustrated. Perebeinos et al. have calculated the II rate in a nanotube, clearly showing that there is no II occurring in the first two subbands. The II threshold energy measured from the edge of the first band scales as $E_{TH} \sim 3/2E_G \sim 1.26/d$ (nm), which is greater than the band gap, as is typical in other semiconductors [18, 19]. To determine if the third subband is populated in our experiments, we look at the nanotube density of states (DOS) in Fig. 5.3. Each Van Hove singularity represents the beginning of a subband. As V_{GS} is lowered beyond threshold, the Fermi level inside the nanotube shifts to the right on the DOS plot and the third subband begins to fill at approximately $|V_{GS}\text{-}V_T| \sim 15$ V. The observed V_T for our devices is in the range of -7 to -15 V. Thus, filling the third subband is within reach experimentally, as avalanche is seen at various V_{GS} and further discussed below. In addition, we find that direct injection into higher subbands at the contacts is also possible, as

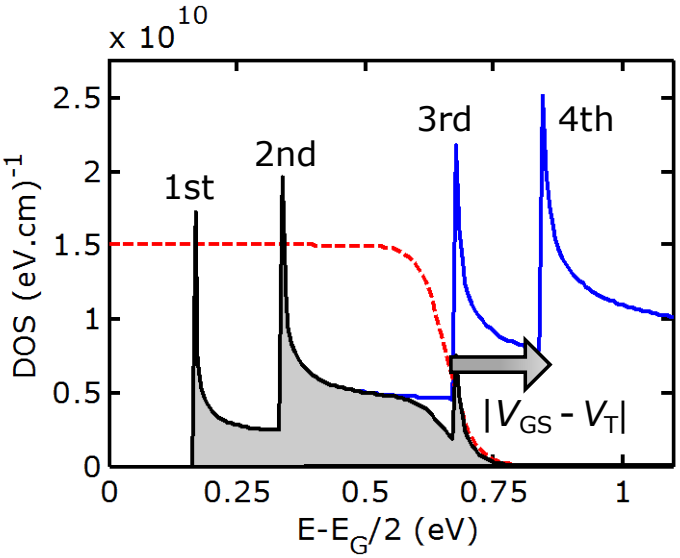

Fig. 5.3 Computed density of states (DOS) showing the first four subbands. The second band begins to fill at $|V_{GS}\text{-}V_T| \sim 5$ V and the third at $|V_{GS}\text{-}V_T| \sim 15$ V, as pictured.

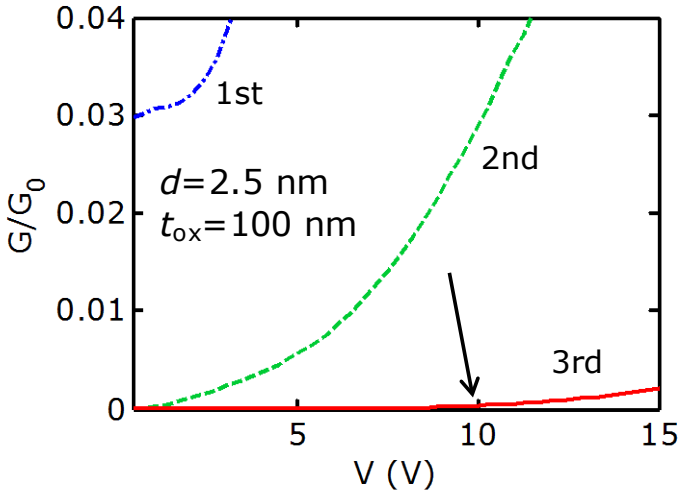

Fig. 5.4 Contact conductance of the first three subbands under direct injection from the Pd electrode. The arrow indicates approximate voltage at which direct injection into the third subband becomes significant.

previously suggested [20]. We estimate this in Fig. 5.4 using a WKB integral to calculate the conductance associated with direct injection into the first three subbands at the Pd electrode. Naturally, injection into higher subbands depends strongly on voltage, and while direct injection into the third band is possible, we expect that high-field intervalley scattering [21, 22] and gate-controlled charge distribution (Fig. 5.3) are primarily responsible for populating the higher subbands.

5.2.1 Experimental Testing

The effects of gate voltage, nanotube length, and temperature on the avalanche current are shown in Fig. 5.5. First, for a given length, a similar current up-kick is observed at high lateral fields at any gate voltage V_{GS} beyond threshold. That is, the four data curves converge on the "up-kick" region at high lateral drain voltage V_{DS} in Figs. 5.5A and 5.5B. Second, for a similar diameter (similar band separations and II threshold E_{TH}), the onset of the avalanche up-kick is seen around the same approximate *field* ($\sim V_{DS}/L$), not the same drain voltage. The two data sets in Figures 5.5A and 5.5B suggest that filling the third subband at large gate voltage is a necessary, but not sufficient, condition to induce current enhancement through hole avalanche. A high lateral electric field set by the drain voltage is also required to create the signature up-kick in the measured *I-V* characteristics.

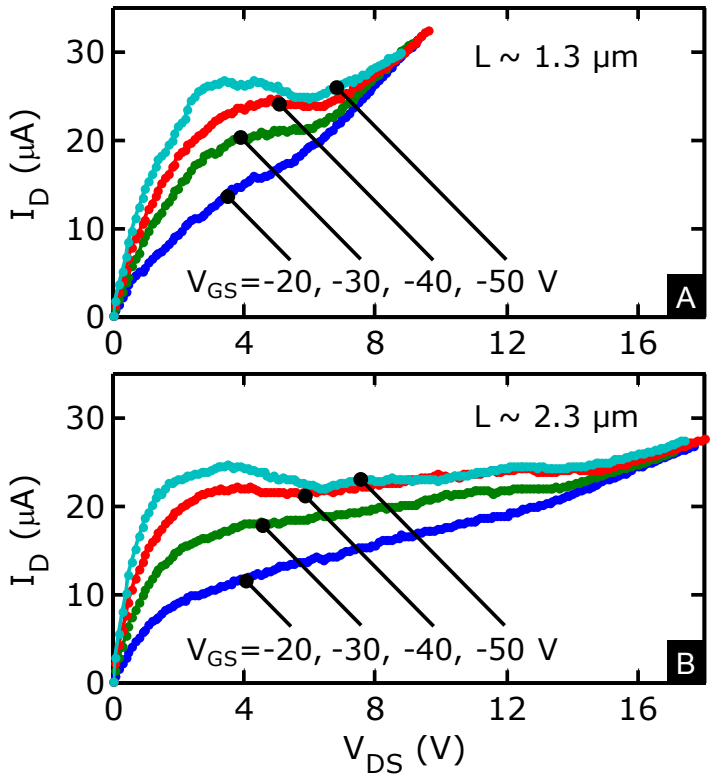

Fig. 5.5 Length dependence of impact ionization tail. Measured reverse bias current vs. drain voltage (V_{DS}) in vacuum with applied back-gate V_{GS} for two s-SWNTs with similar diameter ($d \sim 2.5$ nm) but with device lengths of (A) $L \sim 1.3$ μm and (B) $L \sim 2.3$ μm. The onset voltage for the avalanche "up-kick" scales as the lateral *field* and appears independent of V_{GS}.

An important feature of the avalanche process in many semiconductors such as silicon is the negative temperature dependence of the II coefficient [23]. As the phonon scattering rate increases with temperature, free carriers gain less energy from the field and the II rate decreases at higher temperatures. Here, such trends are examined in Figure 5.6, showing experimental data taken from 150 K to 300 K. Unlike in silicon, we observe negligible temperature dependence of the high-bias impact ionization region. The essential difference lies in that the optical phonon (OP) emission MFP ($\lambda_{OP,ems}$) varies minimally with temperature in SWNTs. As the OP energy is much greater than in other materials, the OP occupation $N_{OP} = 1/[\exp(\hbar\omega_{OP}/k_BT)-1]$ is very small, $\ll 1$, where k_B is the Boltzmann constant. Following [3], the spontaneous OP emission MFP can be written as $\lambda_{OP,ems} = [N_{OP}(300)+1] / [N_{OP}(T)+1]\lambda_{OP,300}$ where $\lambda_{OP,300} \approx 14d$ [13]. This MFP is shown for two diameters in Fig. 5.7, illustrating the negligible temperature variation. The lack of temperature dependence and that of a significant current (Joule heating) dependence of

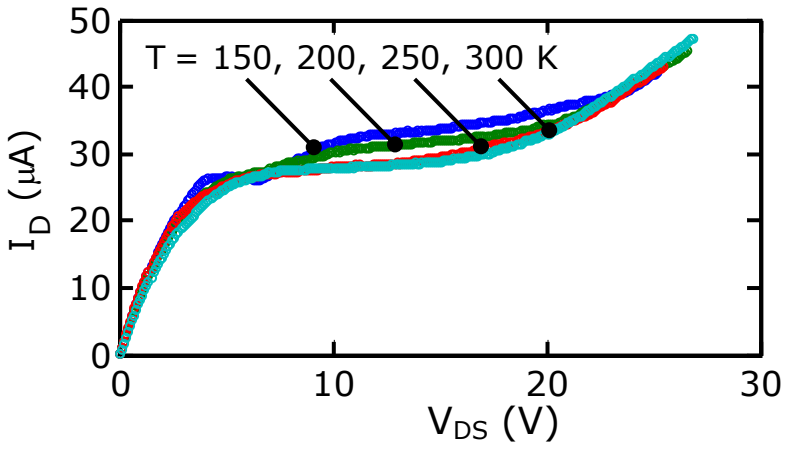

Fig. 5.6 Temperature insensitivity of impact ionization tail. Measured reverse bias I_D-V_{DS} curves for an s-SWNT with $d \sim 2.2$ nm and $L \sim 2.2$ μm, in vacuum.

the up-kick also indicates there is no significant contribution from thermal current generation. Quite the opposite, given the generation of EHPs rather than OPs during II, a lowered Joule heating rate in the highest field region near the drain is expected.

5.2.2 Modeling Avalanche Current in CNTFETs

In order to better understand the field dependence of the avalanche process, an existing SWNT model [3] has been modified by including II as an additional current path through a parallel resistor. The choice is motivated by the physical picture in Fig. 5.1, which shows electron transport in the conduction band "turning on" as an additional channel at fields high enough to induce hole-driven II. The expression for this resistor is given as $R_{II} = R\exp(E_{TH}/q\lambda_{OP,ems}F)$, where R is for single-band transport, computed self-

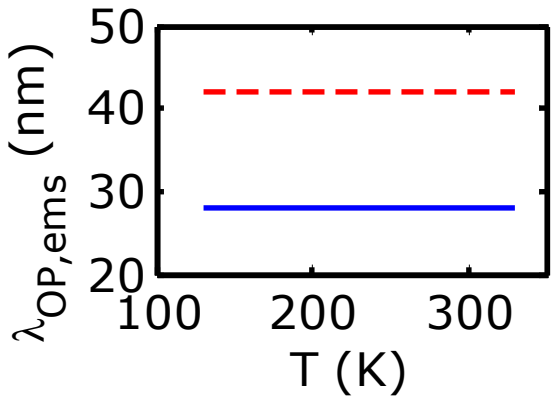

Fig. 5.7 Optical phonon emission mean free path in nanotubes ($\lambda_{OP,ems}$) calculated for two diameters vs. temperature. Unlike other materials, $\lambda_{OP,ems}$ does not vary a lot with temperature.

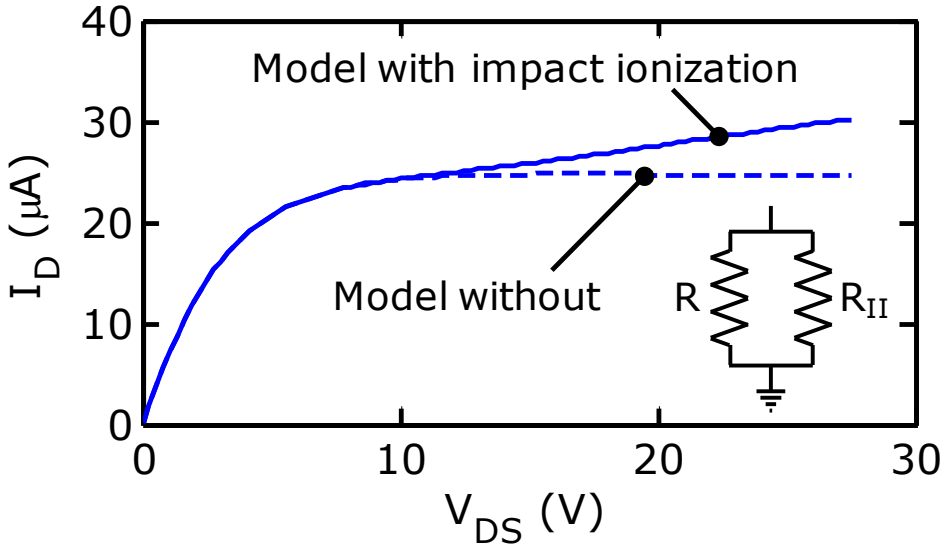

Fig. 5.8 Model including and excluding impact ionization as a second parallel channel which begins to open up at high field.

consistently with the SWNT temperature [3]. The results are shown in Fig.5.8 with $\lambda_{OP,ems}$ included as mentioned above, and without any other adjustable parameters. Despite being an "augmented" single-band model, the simulation correctly captures the experimentally observed current up-kick and its delayed voltage onset. The simple analysis also allows us to gain physical insight into the avalanche process, and to intuitively extract a few more key parameters. More steps in the future, such as inserting multiple subbands, will be taken to more accurately model the current up-kick.

5.2.3 A Novel Method of Extracting Inelastic Optical Phonon Emission Length

In the parallel resistor approach, the resulting avalanche current is derived to be $I_{II} \approx I_S \exp(-E_{TH}/q\lambda_{OP,ems}F)$, where I_S is the saturation current reached before II becomes significant. Inserting the expected diameter dependence $E_{TH} \approx E_1/d$ and $\lambda_{OP,ems} \approx \lambda_1 d$, we obtain $I_{II} \approx I_S \exp(-E_1/q\lambda_1 F d^2)$, where E_1 and λ_1 are the threshold energy and MFP for a nanotube of diameter 1 nm. Consequently, the average field at which $I_{II} = I_S/2$ is given by $\langle F_{TH} \rangle \approx E_1/q\lambda_1 d^2 \ln(2)$. The experimental data in Fig. 5.9A is used to extract this field (but not the peak field) in our devices by extrapolating from the tail region to $\langle F_{TH} \rangle$ at which the current reaches one half the saturation values. These values are plotted against $1/d^2$ for nanotubes of several diameters ($d \sim$ 2.2-3.6 nm) in Fig. 5.9B. The slope of the linear fit thus scales as the ratio between the II threshold energy and the inelastic MFP,

E_1/λ_1. However, the avalanche process is a strong function of the field, and most EHPs are generated at the peak field, $F_{TH,MAX}$. The latter is estimated by noting that the potential near the drain has a dependence $V(x) \approx \ell F_0 \sinh(x/\ell)$, where $F_0 \sim 1$ V/μm is the saturation velocity field [6] and ℓ is an electrostatic length scale comparable to t_{ox} [8, 24, 25]. Fitting this expression to our voltage conditions and nanotube dimensions, we find $F_{TH,MAX}/\langle F_{TH}\rangle \approx 4.5$ for the $L = 1$ μm device, and 3.5 for $L = 2$ μm. Thus, using the peak instead of the average field, the empirically extracted slope gives $E_1/\lambda_1 \sim 0.088$ eV·nm, where we take $E_1 = 1.26$ eV as the bottom of the third subband. Accounting for fit errors, this yields $\lambda_1 = 15 \pm 3$ nm as the inelastic OP emission MFP for $d = 1$ nm, or generally $\lambda_{OP,ems} = \lambda_1 d$. This value is in good agreement with the theoretically predicted $14d$ nm in [13], and our approach demonstrates a novel empirical method for extracting this im-

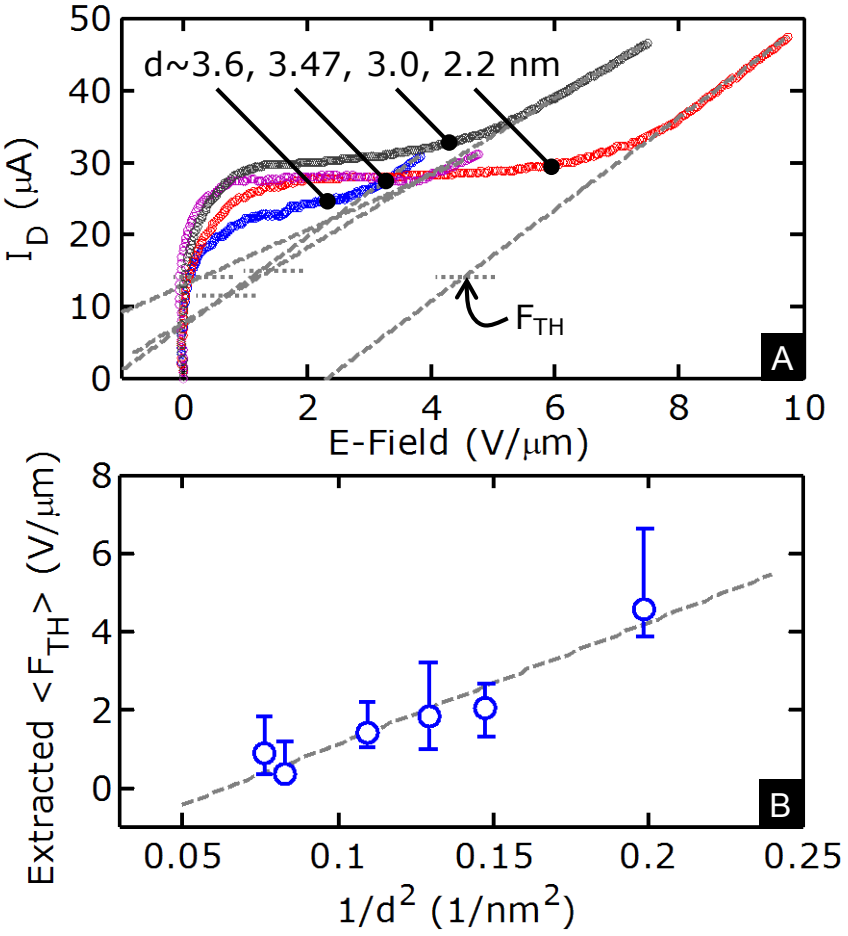

Fig. 5.9 Diameter dependence of avalanche threshold field F_{TH}. (A) Current vs. average channel field $(V_{DS}-I_D R_C)/L$ for several s-SWNT diameters. (B) Extracted average $\langle F_{TH}\rangle$ vs. $1/d^2$. The uncertainty in diameter from AFM measurements is 0.4 nm.

portant transport parameter from high-field electrical measurements.

5.3 Conclusions

In summary, we observe a remarkable current increase in 1-4 μm long semiconducting SWNTs driven into avalanche impact ionization at high fields. Analyzing near-breakdown *I-V* data, we find the avalanche process to be nearly temperature independent, but strongly diameter dependent ~exp(-1/d^2), unlike other materials. In addition, a novel estimate of the inelastic OP scattering length $\lambda_{OP,ems} \approx 15d$ nm is obtained by fitting against a model of the high-field current "tail." We note that upper subband transport must be considered at high bias, and has a significant effect on the current carrying capacity of such nanomaterials. The results also suggest that avalanche-driven devices with highly non-linear characteristics can be fashioned from s-SWNTs.

5.4 References

[1] A. Javey, J. Guo, M. Paulsson, Q. Wang, D. Mann, M. Lundstrom, and H. J. Dai, "High-field quasiballistic transport in short carbon nanotubes," *Physical Review Letters,* vol. 92, p. 106804, March 2004.

[2] X. J. Zhou, J. Y. Park, S. M. Huang, J. Liu, and P. L. McEuen, "Band structure, phonon scattering, and the performance limit of single-walled carbon nanotube transistors," *Physical Review Letters,* vol. 95, p. 146805, September 2005.

[3] E. Pop, D. A. Mann, K. E. Goodson, and H. J. Dai, "Electrical and thermal transport in metallic single-wall carbon nanotubes on insulating substrates," *Journal of Applied Physics,* vol. 101, p. 093710, May 2007.

[4] Z. Yao, C. L. Kane, and C. Dekker, "High-field electrical transport in single-wall carbon nanotubes," *Physical Review Letters,* vol. 84, pp. 2941-2944, March 2000.

[5] D. Jena, "High-field current-carrying capacity of semiconducting carbon nanotubes," pre-print arXiv:0804.3997, June 2008.

[6] Y. F. Chen and M. S. Fuhrer, "Electric-field-dependent charge-carrier velocity in semiconducting carbon nanotubes," *Physical Review Letters,* vol. 95, p. 236803, December 2005.

[7] Y. Ouyang, Y. Yoon, and J. Guo, "On the current delivery limit of semiconducting carbon nanotubes," *Journal of Computer-Aided Materials Design,* vol. 14, pp. 73-78, April 2007.

[8] J. Tersoff, M. Freitag, J. C. Tsang, and P. Avouris, "Device modeling of long-channel nanotube electro-optical emitter," *Applied Physics Letters,* vol. 86, p. 263108, June 2005.

[9] E. A. Amerasekera and C. Duvvury, *ESD in Silicon Integrated Circuits*, 2nd ed. New York, NY: Wiley, 2002.

[10] K. Bosnick, N. Gabor, and P. McEuen, "Transport in carbon nanotube p-i-n diodes," *Applied Physics Letters,* vol. 89, p. 163121, October 2006.

[11] W. Shockley, "Problems related to p-n junctions in silicon," *Solid-State Electronics,* vol. 2, pp. 35-60, January 1961.

[12] F.-C. Hsu, P.-K. Ko, T. Simon, C. Hu, and R. S. Muller, "An analytical breakdown model for short-channel MOSFET's," *IEEE Transactions on Electron Devices,* vol. 29, pp. 1735-1740, November 1982.

[13] V. Perebeinos and P. Avouris, "Impact excitation by hot carriers in carbon nanotubes," *Physical Review B,* vol. 74, p. 121410R, September 2006.

[14] S. O. Koswatta, M. S. Lundstrom, and D. E. Nikonov, "Band-to-band tunneling in a carbon nanotube metal-oxide-semiconductor field-effect transistor is dominated by phonon-assisted tunneling," *Nano Letters,* vol. 7, pp. 1160-1164, May 2007.

[15] D. Jena, T. Fang, Q. Zhang, and H. Xing, "Zener tunneling in semiconducting nanotube and graphene nanoribbon p-n junctions," *Applied Physics Letters,* vol. 93, p. 112106, September 2008.

[16] L. Marty, E. Adam, L. Albert, R. Doyon, D. Menard, and R. Martel, "Exciton formation and annihilation during 1D impact excitation of carbon nanotubes," *Physical Review Letters,* vol. 96, p. 136803, April 2006.

[17] V. Perebeinos and P. Avouris, "Phonon and electronic nonradiative decay mechanisms of excitons in carbon nanotubes," *Physical Review Letters,* vol. 101, p. 057401, August 2008.

[18] J. Allam, "'Universal' dependence of avalanche breakdown on bandstructure: Choosing materials for high-power devices," *Japanese Journal of Applied Physics Part 1-Regular Papers Short Notes & Review Papers,* vol. 36, pp. 1529-1542, March 1997.

[19] C. L. Anderson and C. R. Crowell, "Threshold energies for electron-hole pair production by impact ionization in semiconductors," *Physical Review B,* vol. 5, pp. 2267-2272, March 1972.

[20] J. Guo, M. A. Alam, and Y. Ouyang, "Subband gap impact ionization and excitation in carbon nanotube transistors," *Journal of Applied Physics,* vol. 101, p. 064311, March 2007.

[21] J. Appenzeller, J. Knoch, M. Radosavljevic, and P. Avouris, "Multimode transport in Schottky-barrier carbon-nanotube field-effect transistors," *Physical Review Letters,* vol. 92, p. 226802, June 2004.

[22] G. Pennington, N. Goldsman, A. Akturk, and A. E. Wickenden, "Deformation potential carrier-phonon scattering in semiconducting carbon nanotube transistors," *Applied Physics Letters,* vol. 90, p. 062110, February 2007.

[23] C. R. Crowell and S. M. Sze, "Temperature dependence of avalanche multiplication in semiconductors," *Applied Physics Letters,* vol. 9, pp. 242-244, August 1966.

[24] A. B. Grebene and S. K. Ghandhi, "General theory for pinched operation of the junction-gate FET," *Solid-State Electronics,* vol. 12, pp. 573-589, July 1969.

[25] P. K. Ko, "Approaches to scaling," in *Advanced MOS Device Physics*, N. G. Einspruch and G. Gildenblat, Eds. San Diego: Academic Press, 1989, pp. 1-35.

CHAPTER 6

PROBING THE UPPER LIMITS OF CURRENT DENSITY IN ONE-DIMENSIONAL CARBON INTERCONNECTS

6.1 Introduction

As Cu interconnects for integrated circuits are downscaled, they become susceptible to electromigration and their performance degrades from increased grain boundary and surface scattering [1]. To combat these problems, metallic single-wall carbon nanotubes (m-CNTs) and graphene nanoribbons (GNRs) have been studied as potential Cu replacements [2, 3]. These one-dimensional (1-D) interconnects have strong sp^2 bonds which suppress electromigration and allow for current densities two to three orders of magnitude higher than Cu. However, an understanding of the fundamental limits of current flow is still lacking. Exploring m-CNTs, measurements demonstrate currents up to ~30–35 μA , approximately 50% higher than previously thought possible, corresponding to current densities of ~3×10^9 A/cm^2 or ~9 mA/μm for diameters of ~1.2 nm. Such high currents are enabled by carrier injection into upper m-CNT subbands, while cooling through remote substrate

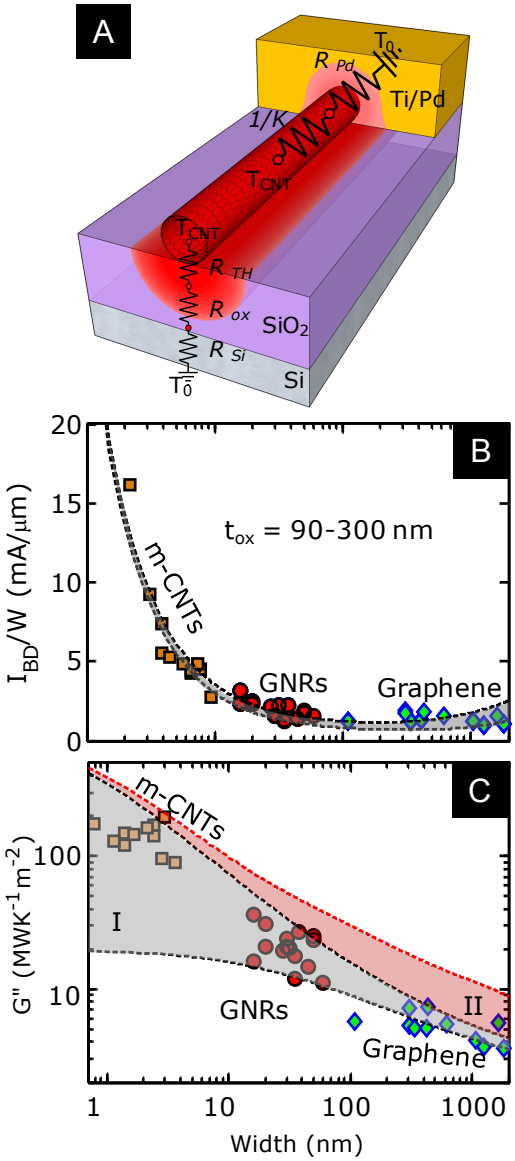

Fig. 6.1 (A) Cross section of CNT device showing heat dissipation pathways. (B) Breakdown current density versus width (diameter for CNT) for various 1-D carbon allotropes. Lines represent model calculated over the range of oxide thickness t_{ox} = 90-300 nm. (C) Total thermal conductance versus width (footprint for CNTs) for various 1-D carbon allotropes. Region I (gray shading) represents a thermal boundary resistance range R_{cox} = 0.1 – 5×10^{-8} m^{2}K/W and region II (red shading) represents t_{ox} = 90-300 nm.

phonons is negligible because they increase scattering.

Previous measurement of the current carrying capacity of one-dimensional carbon interconnects was conducted in air up to breakdown or at fields < 5 V/μm. In Fig. 6.1B and 6.1C, measurements from literature are compiled to compare power dissipation between m-CNTs [4], GNRs, and graphene [5]. All of the devices were fabricated in a typical back-gated three-terminal structure (see Fig. 6.2a and 6.2c) for which the power dissipation pathways are shown in Fig. 6.1A. Ultimately, heat dissipates into the underlying substrate and into the contacts. Figure 6.1B shows the current density dependence on the cross-sectional width (the actual width of the GNR and the circumference of the m-CNT) from references [4, 5]. As the width decreases, the breakdown current density increases (up to ~3 mA/μm for a 15 nm wide GNR and ~16 mA/μm for a 0.7 nm diameter m-CNT). This trend comes from the fact that m-CNTs dissipate energy more efficiently than GNRs, as can be seen by the way the total heat dissipation out of the channel scales with width in Fig. 6.1C. So m-CNTs are selected for further investigation to explore the highest current carrying potential for one-dimensional conductors.

6.2 Fabrication and Measurements

To examine m-CNTs, three-terminal back-gated devices are fabricated [4, 6]. Carbon nanotubes are grown on top of 90 nm of SiO_2. Source and drain metal contacts are Ti/Pd and patterned by photolithography (see chapter 1). Fabricated channel lengths vary from 0.2 μm to 3.8 μm, putting these devices in the quasi-ballistic to diffusive transport regime (see chapter 2). A device schematic along with a scanning electron microscope (SEM) image is displayed in Fig. 6.2A. Careful characterization using atomic force microscopy (AFM) and Raman spectroscopy distinguishes single-wall CNTs from multi-walled CNTs [7-9]. First, AFM measurements (Fig. 6.2B) establish an approximate diameter of the m-CNT. These measurements are then cross-checked with G-peak splitting [10] and the radial breathing mode (RBM) [11] peaks from Raman spectroscopy. Displayed in Fig 6.2C is the full spectrum of peaks used in this study (RBM, D, and G peaks). While the RBM is the more accurate measurement of CNT diameter, only three samples had RBM that were resonant with our laser line (633 nm). Thus the G-peak splitting was used to increase our sample size to 20 devices. The range of diameters measured was 1.2 –

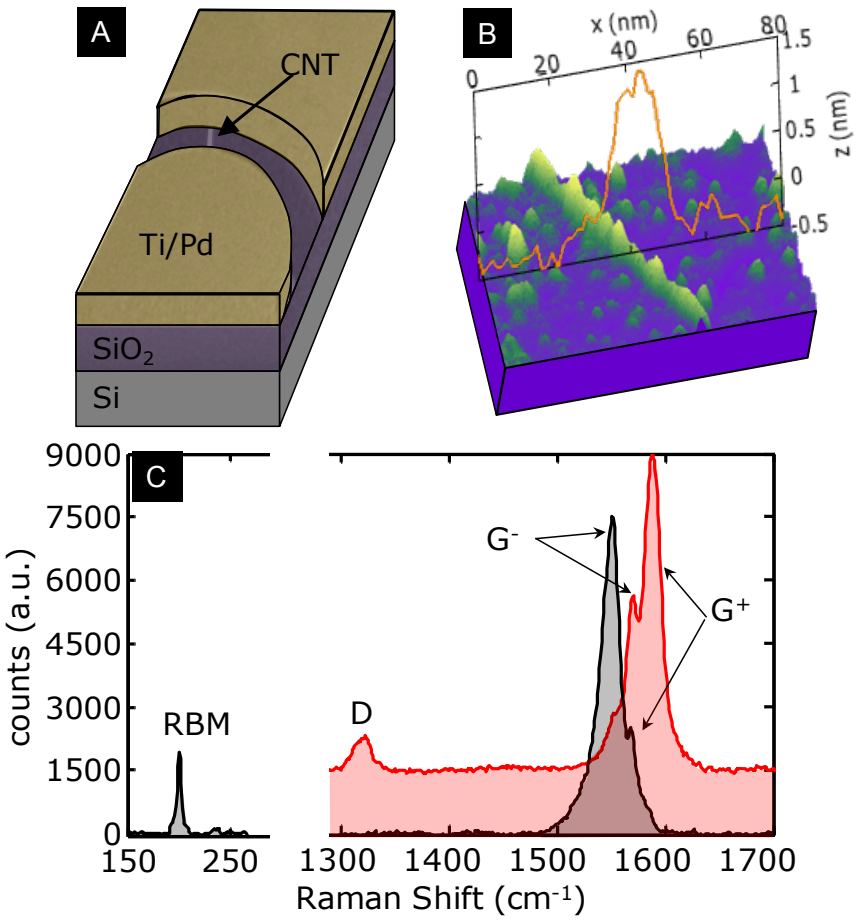

Fig. 6.2. (A) Three-dimensional projection of a SEM of CNT device. (B) Three-dimensional rendering of an AFM image showing a cross section cut of the CNT on top. (C) Raman Spectrum of peaks studied. The G band is very sensitive to changes in doping. The RBM has a FWHM ~ 10 cm^{-1}, characteristic of single-walled CNTs.

2.5 nm. Other possible methods for counting the number of walls or gathering diameter information of metallic nanotubes include transmission electron microscopy (TEM) [12], scanning tunneling microscopy (STM) [13], and Rayleigh scattering [14, 15]. These alternative methods were, however, either not available or were not compatible with the given device configuration.

Measurements were made in vacuum (~10^{-5} Torr) to prevent breakdown through oxidation. The resulting I_D-V_{DS} curves (Fig. 6.3A) display currents at high bias that continue to increase with a slope of ~0.5–1 μA/V, up to currents as high as 35 μA (~9 mA/μm for diameters of ~1.2 nm) at a field of 10 V/μm for pristine CNTs. The slope of the I_D-V_{DS} plot at high fields does not depend on diameter (Fig. 6.4A). Although the diameter sets the upper subband energy difference, threshold voltage shifts and changing contacts in vacuum coupled with diameter uncertainty make it difficult to observe a trend. When

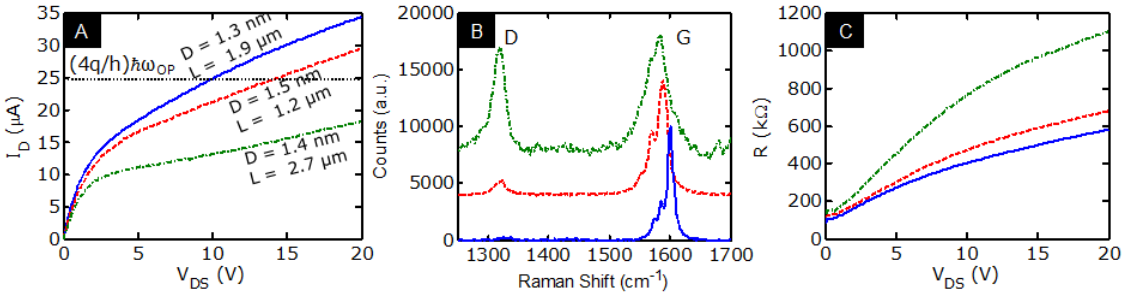

Fig. 6.3 (A) Typical I_D-V_{DS} vacuum measurements. The dotted line is the previously predicted current limit of ~ 25 μA. (B) Comparative Raman line scans for the three measurements in (A) showing that lower currents are a result of defects. (C) Device resistance versus V_{DS}.

plotting the slope as a function of length, there appears to be a small trend wherein the currents increase slower for longer m-CNTs (Fig. 6.4B). The length dependence may point to the strong field dependence of tunneling from contacts to upper subbands.

The maximum achievable current is limited by sample quality as the current levels drop as the D-peak increases (Fig. 6.3B). Despite this trend, m-CNTs can still exceed 25 μA even when the D-peak intensity is ~ 30% that of the G-peak intensity. The rest of the data presented in this paper will be for pristine m-CNTs having no discernible D-peak. These results contradict earlier findings, which state current should saturate at high bias from optical phonon emission [16]. Given an optical phonon emission energy of $\hbar\omega_{OP} \sim 0.16$ eV, this would limit current to $(4q/h)\times\hbar\omega_{OP} \sim 25$ μA. Still, the effects of heating are present as the resistance continues to increase with V_{DS} (Fig. 6.3C).

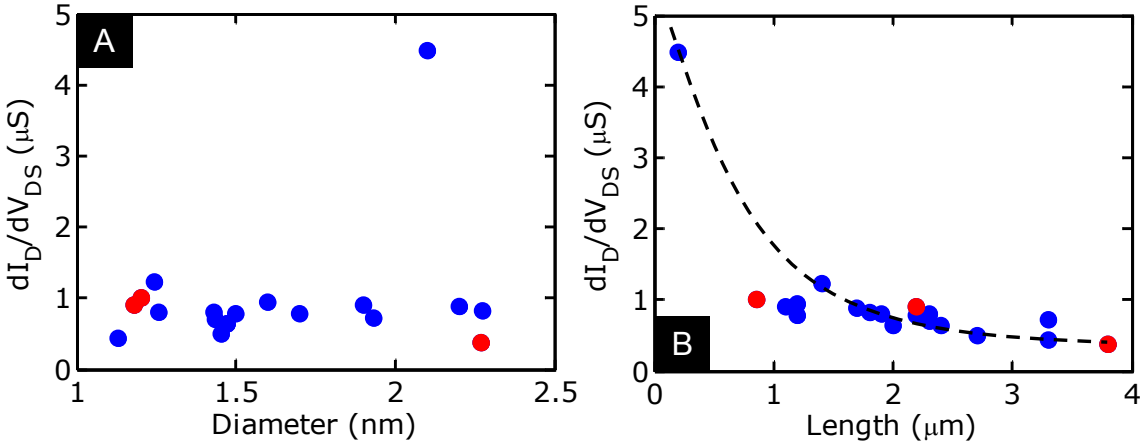

Fig. 6.4 (A) Slope of I_D-V_{DS} plots at high bias as a function of diameter. Red dots indicate m-CNTs which have diameters confirmed by their radial breathing mode. (B) Slope of I_D-V_{DS} plots at high bias as a function of length. The dashed line is drawn to guide the eye.

6.3 High-Field Current Behavior

It is possible for CNTs conducting diffusively to exceed 25 μA. Semiconducting CNTs can do so through ambipolar conduction [17] or impact ionization [6]. Potential sources for this increase in current could include parasitic leakage paths, defect assisted interband tunneling[18], ambipolar conduction [17], or remote Joule heating [19]. Monitoring the gate and source current did not detect an appreciable leakage current. Previous theory predicted that defects could lead to enhanced currents at high fields through inter-sub-band tunneling [18]. However, this phenomenon is not observed given that lower currents are measured for m-CNTs having a larger D-peak.

Ambipolar conduction [17, 20, 21] requires biasing devices in a manner such that both electrons and holes may enter the channel. However, it is uncommon to observe a ratio that is larger than 3, as displayed in Fig. 6.5A. This small ratio leads to small gate dependences in the I_D-V_{DS} sweeps. Unlike previous measurements on ambipolar devices [17, 20, 21], changing the gate bias does not alter the high bias behavior of the device, seen in Fig. 6.5B. Furthermore, the I_D-V_{DS} curves are the same regardless of the polarity. The I_D-V_{DS} curves are symmetric between positive and negative sweeps.

Since self-heating has been shown to limit current in m-CNTs and other 1-D conductors [5, 22, 23], a power dissipation mechanism that lessens the impact of Joule heating could lead to higher currents., Modeling both the m-CNT current and temperature in a

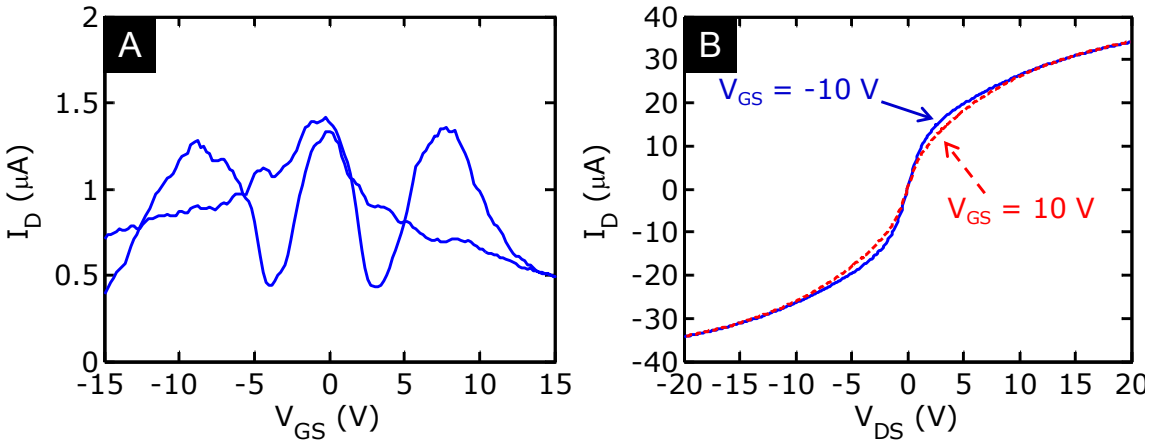

Fig. 6.5 (A) Typical I_D-V_{GS} sweep of an m-CNT that has a diameter of 2.3 nm and is 1.8 μm long. (B) I_D-V_{DS} sweeps for the same device for negative (solid blue) and positive (dashed red) gate bias. At lower bias there is some change in current but the curves merge at high bias.

self-consistent manner explores the impact of self-heating [24]. The m-CNT temperature was calculated using the one-dimensional heat diffusion equation.

$$A\kappa\frac{\partial^2 T}{\partial x^2} + p' = g\left(T - T_0\right) \tag{6.1}$$

Here A is the m-CNT cross sectional area, κ is the m-CNT thermal conductivity, p' is the power generation per unit length, g is the thermal boundary conductance (TBC), and T_0 is the background temperature. The TBC value is calculated based on phonon transmission through the m-CNT interface [4] and near-field energy transfer through SiO_2 surface phonon polaritons (SPP) [25] as seen in Fig. 6.6A. The diffuse mismatch model [4] is used to calculate the phonon contribution to heat transport across the interface. An analytical expression for a quantum electrodynamic (QED) conductance accounts for the near-field energy exchange between carriers and surface polar phonon (SPP) modes [25, 26]. At high fields where the m-CNT can reach temperatures upwards of 1000 K, the TBC is very high ~0.4 $WK^{-1}m^{-1}$ for a 2 nm diameter CNT.

The QED contribution can be expressed through the expression [27]

$$g_{QED} = \sum_{\nu}\frac{4\omega_\nu}{\pi\upsilon_F}2e^2\omega_\nu\delta_\nu I_0\left(\frac{R\omega_\nu}{\upsilon_F}\right)^2 K_0\left(\frac{2\left(y+R\right)}{\upsilon_F/\omega_\nu}\right)\frac{k_B\Theta_1}{\hbar\upsilon_F} \tag{6.2}$$

where

$$\Theta_1\left(T_{OX},T_{CNT}\right) = \frac{\hbar\omega_\nu}{2k_B\left(T_{CNT}-T_{OX}\right)}\left[\coth\left(\frac{\hbar\omega_\nu}{2k_BT_{CNT}}\right) - \coth\left(\frac{\hbar\omega_\nu}{2k_BT_{OX}}\right)\right] \tag{6.3}$$

and v_F is the Fermi velocity (10^8 cm/s), $\hbar\omega_\nu$ are the SPP mode energies, δ_ν is the oscillation strength of each mode ν, y is the distance between the bottom of the CNT and the underlying substrate (0.34 nm), R is the radius of the CNT, and I_0 and K_0 are imaginary Bessel functions. Table 6.1 contains all the constants that relate specifically to the SPP modes. The individual contributions of each mechanism to the overall TBC are plotted in Fig. 6.6B. It should be noted that the spreading thermal resistance in the substrate still makes up an appreciable portion of the total TBC and a thinner oxide would result in even better heat dissipation.

Table 6.1 SPP mode energies and oscillation strength

ν	$\hbar\omega_\nu$ (meV)	δ_ν
1	50	0.004
2	63	0.038
3	100	0.005
4	153	0.089

The mean free paths (MFPs) of different electron-phonon scattering mechanisms can now be calculated since the temperature is known. The MFP in turn is used to calculate the resistance profile.

$$R(V,T) = R_C + \frac{h}{4q^2}\left\{1 + \int_{-L/2}^{L/2} \frac{dx}{\lambda_{eff}\left[V, T(x)\right]}\right\} \tag{6.4}$$

where R_C is the contact resistance, L is the length of the CNT (defined as oriented along the x axis), and λ_{eff} is the effective mean free path calculated through Matthiessen's rule. Adding in contact resistance in series with R_{CNT}, the current given a specific bias can be calculated. Using equation (6.4), multiplying the current squared generates a power profile which is input into equation (6.1).

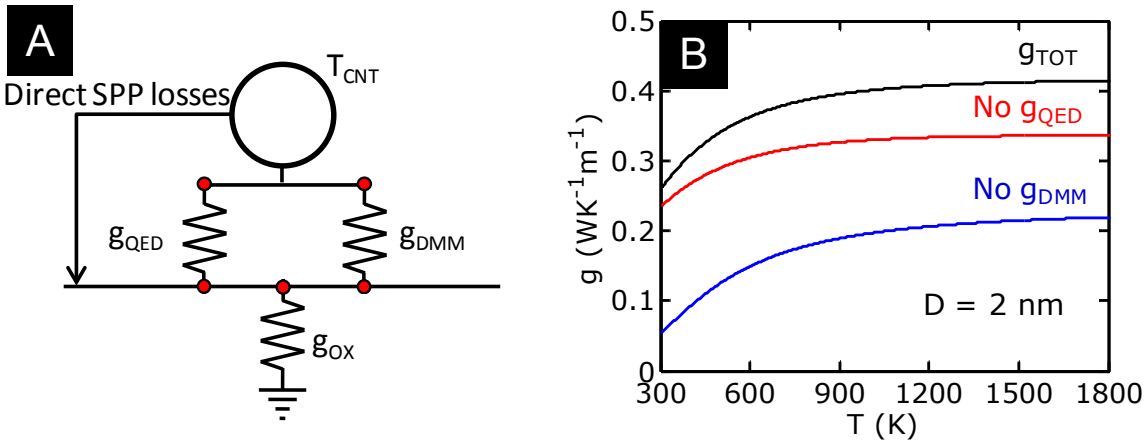

Fig. 6.6 (A) Thermal resistive network showing energy dissipation mechanisms into the substrate. (B), g_{TOT} vs. temperature for a 2 nm diameter CNT showing the contribution when the QED component or DMM component is removed.

Direct power dissipation through remote phonon scattering, in addition to optical and acoustic phonon scattering, is considered in calculating the effective MFP. The SPP mode having energy of $\hbar\omega_{SPP} \sim 60$ meV for SiO_2 has been previously shown to interact with carriers [26, 28]. When calculating the power input into the temperature simulation, SPP scattering is not included in equation (6.4) as it does not contribute to the lattice heating. While this mechanism does serve to cool m-CNTs during bias, it reduces the current by lowering the effective MFP, increasing the total resistance of the device. Since there is no extraction of the SPP scattering MFP to date, fitting values to data gives an MFP of ~80-100×d nm. The value of each MFP as a function of drain bias is shown in Fig. 6.7B for a

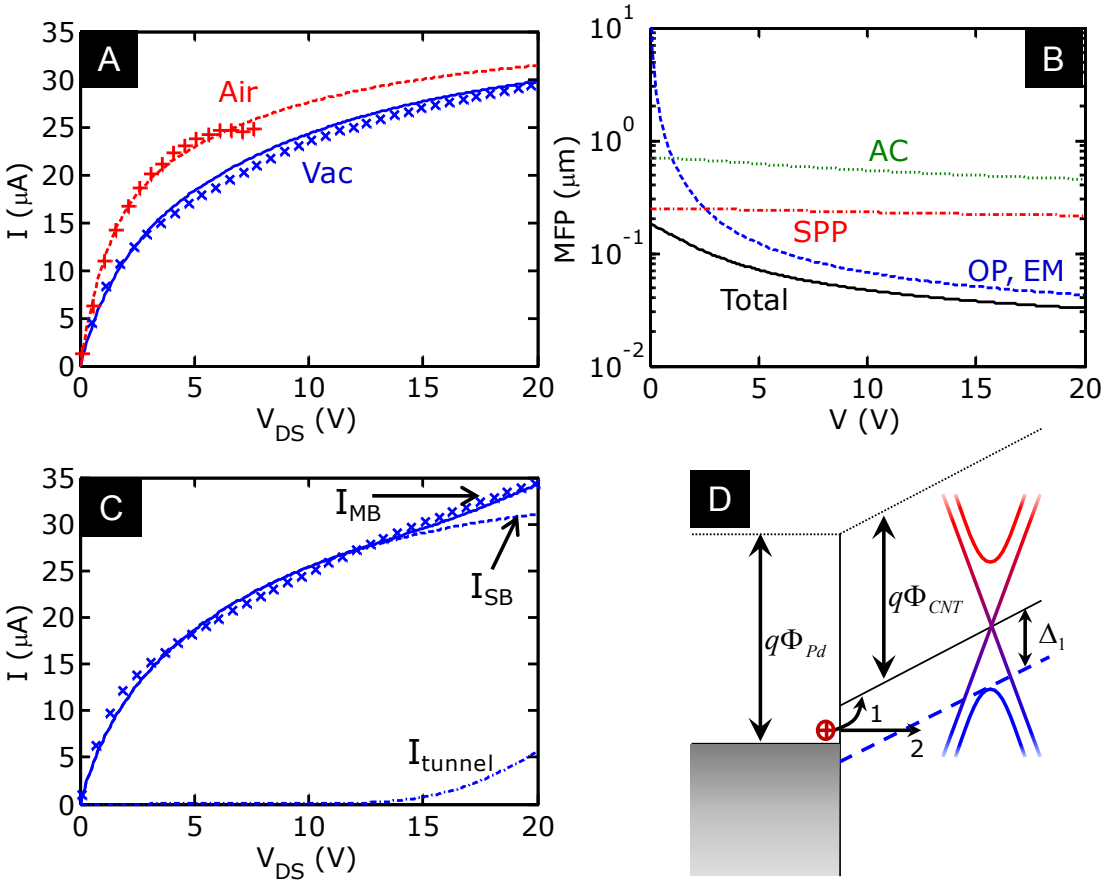

Fig. 6.7 (A) Air (red dashed line) versus vacuum (blue solid line) I_D-V_{DS} for the same CNT. Symbols = Data, Lines = model. L = 2.5 μm, D = 2.5 nm. Air model does not include SPP scattering and vacuum model includes SPP scattering. (B) MFP versus V_{DS} showing the contribution from each different scattering mechanism. (C) I_D-V_{DS} plot showing difference between model with and without tunneling into higher subbands. Dashed blue line indicates model without tunneling into higher subband (I_{SB}). Dashed-dot blue line indicates current in higher subband. L = 1.9 μm, D = 1.3 nm. (D) Band diagram showing normal single band conduction (1) and tunneling into higher subbands (2).

2.5 μm long m-CNT having a diameter of 2.5 nm. At low and medium fields (< 3 V/μm), SPP scattering contributes significantly into the total MFP. However at higher fields, optical phonon emission is dominant because it has much higher occupation.

Interestingly, SPP scattering only seems to be needed to model data taken in vacuum. When modeling data taken in air for the same m-CNT, a better match is achieved when no SPP interactions are considered, as shown in Fig. 6.7A. One explanation for this difference could be that in air, the presence of water vapor, oxygen, or other contaminants serve to screen SPP phonons, thus preventing the near-field interactions between substrate and m-CNT. It should be noted that the first I_D-V_{DS} sweep taken in vacuum replicates the same sweep taken in air. All subsequent scans, even those made several hours later, show lower currents (Fig. 6.7A). It can thus be assumed that what was serving to screen SPP phonons has now been removed. Upon removal from vacuum to air, the original behavior in air is recovered. This could explain why breakdown measurements performed in air have never shown evidence of SPP scattering [4], while measurements in vacuum have [19].

Even with the inclusion of SPP interactions, at fields approaching ~10 V/μm, the model predicts current saturation from optical phonon scattering [16]. Up to this point, only single-band conduction has been considered (I_{SB} in Fig. 6.6C), as is often the case in m-CNT transport models. However, it has been shown that conduction in semiconducting CNTs can happen in higher subbands (one of the conditions for impact ionization) [6]. One way of achieving higher subband conduction would be for carriers to be directly injected from the contacts. A tunneling transmission coefficient, τ, from the contacts across a triangular barrier [29] into the second subband is given as

$$\tau = \exp\left[-\frac{\pi\left(\Delta_i + \Phi_{CNT} - \Phi_{Pd}\right)}{4q\hbar v_F F}\right] \tag{6.5}$$

where Δ_i is the distance between the i-th subband and Dirac point, F is the lateral electric field, v_F is the Fermi velocity, Φ_{CNT} and Φ_{Pd} are the work functions of the m-CNT and Pd respectively. The band diagram for this process is shown in Fig 6.7D. The work function of the m-CNT from 4.3 eV to 4.7 eV can fit the data. Such a large change in work function can come about from the lack of oxygen and change in doping in vacuum [30]. The

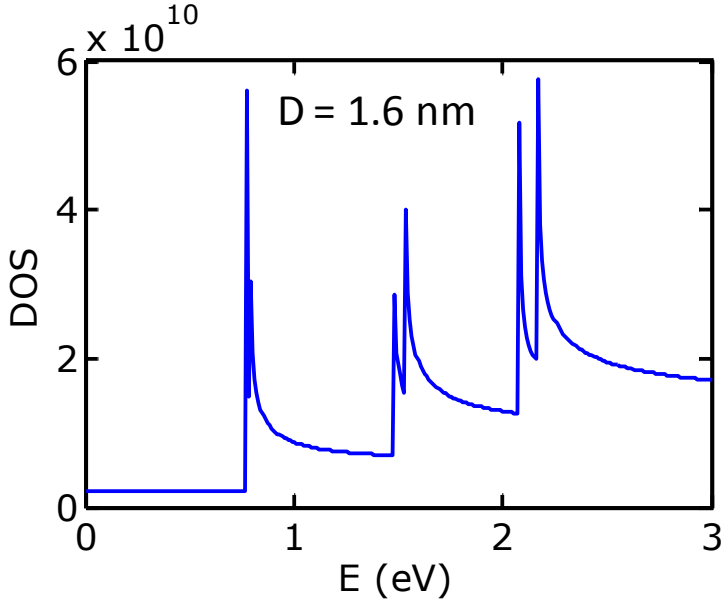

Fig. 6.8. Electron density of states for an m-CNT having a diameter of 1.6 nm.

dashed-dotted line in Fig 6.7C shows the current contribution I_{tunnel} from this tunneling process.

When considering higher subband conduction, the change in band structure must be accounted for [31]. Since the bands are changed, so too is the density of states (DOS). When a single band is considered the DOS for an m-CNT is $D_M = 2/\pi\hbar v_F$. When considering higher subbands the DOS is given as

$$D(E) = D_M \sum_i \left(1 - \frac{\Delta_i}{E}\right)^{-1/2} u(E - \Delta_i) \tag{6.6}$$

where Δ_i is the energy separation from the first subband to the i-th band and $u(E)$ is the Heaviside step function, displayed in Fig. 6.8. As the DOS changes, the effective mass and subsequently the carrier velocity will change as well.

$$v_i(E) = \frac{\hbar v_F^2 k}{\sqrt{\Delta_i^2 + (\hbar v_F k)^2}} \tag{6.7}$$

Given these changes, the mean free path (MFP) in the model should be adjusted to account for higher subband transport. The optical phonon MFP is adjusted in the following way:

$$\lambda_{OP}(E,T) = \lambda_{OP,300} \frac{N_{OP}(T = 300K) + 1}{N_{OP}(T) + \frac{1}{2} \pm \frac{1}{2}} \frac{D_M}{D(E \mp \hbar\omega_{OP})} \frac{v_i(E)}{v_F} \tag{6.8}$$

where N_{OP} is the optical phonon occupation given by the Bose-Einstein distribution and $\lambda_{OP,300}$ ~ 10-15×d nm is the optical phonon MFP at 300 K and $\hbar\omega_{OP}$ ~180 eV. In the case of $\pm(\mp)$ the top sign refers to emission and the bottom sign refers to absorption. The SPP MFP is calculated using the exact same expression, except that the MFP at 300 K (λ_{SPP} ~ 80-100×d) and SPP energy ($\hbar\omega_{SPP}$ ~60 meV) values is different. The acoustic phonon MFP is given as

$$\lambda_{AP}(E,T) = \lambda_{AP,300} \frac{300}{T} \frac{D_M}{D(E)} \frac{v_i(E)}{v_F} \tag{6.9}$$

where $\lambda_{AP,300}$ ~ 280×d nm is the acoustic phonon MFP at 300 K. When included, the model accurately reproduces currents (I_{MB} in Fig. 6.6C) up to 10 V/μm. It should be noted that this process requires very high fields and the onset of tunneling does not start until ~ 6-7 V/μm. In air, it is very likely that the m-CNT would break before these fields are reached.

6.4 Conclusions

In conclusion, single-walled m-CNTs can carry upwards of 35 μA, which corresponds to a current density of up to ~ 9 mA/μm or 3×10^9 A/cm^2. These measured values represent the highest known to date for any 1-D diffusive conductor. Such high currents are a result of direct injection of carriers into higher subbands from the contacts. Furthermore, the currents do not show saturation, indicating that the absolute maximum current has not been achieved. Comparing m-CNTs to GNRs also shows that m-CNTs are more energy efficient and can carry the highest possible current densities of any diffusive conductor.

6.5 References

[1] J. J. Plombon, E. Andideh, V. M. Dubin, and J. Maiz, "Influence of phonon, geometry, impurity, and grain size on Copper line resistivity," *Applied Physics Letters,* vol. 89, Sep 11 2006.

[2] G. F. Close, S. Yasuda, B. Paul, S. Fujita, and H. S. P. Wong, "A 1 GHz integrated circuit with carbon nanotube interconnects and silicon transistors," *Nano Letters,* vol. 8, pp. 706-709, Feb 2008.

[3] H. Li, C. Xu, N. Srivastava, and K. Banerjee, "Carbon Nanomaterials for Next-Generation Interconnects and Passives: Physics, Status, and Prospects," *IEEE Transactions on Electron Devices,* vol. 56, pp. 1799-1821, Sep 2009.

[4] A. Liao, R. Alizadegan, Z.-Y. Ong, S. Dutta, F. Xiong, K. J. Hsia, and E. Pop, "Thermal dissipation and variability in electrical breakdown of carbon nanotube devices," *Physical Review B,* vol. 82, p. 205406, 2010.

[5] A. D. Liao, J. Z. Wu, X. R. Wang, K. Tahy, D. Jena, H. J. Dai, and E. Pop, "Thermally Limited Current Carrying Ability of Graphene Nanoribbons," *Physical Review Letters,* vol. 106, p. 256801, Jun 20 2011.

[6] A. Liao, Y. Zhao, and E. Pop, "Avalanche-Induced Current Enhancement in Semiconducting Carbon Nanotubes," *Physical Review Letters,* vol. 101, p. 256804, Dec 19 2008.

[7] R. Alizadegan, A. D. Liao, F. Xiong, E. Pop, and K. J. Hsia, "Effects of tip-nanotube interactions on atomic force microscopy imaging of carbon nanotubes," *Nano Research,* vol. 5, pp. 235-247, Apr 2012.

[8] A. Jorio, M. S. Dresselhaus, R. Saito, and G. Dresselhaus, *Raman Spectroscopy in Graphene Related Systems*. Weinheim, Germany: WILEY-VCH, 2011.

[9] M. S. Dresselhaus, G. Dresselhaus, R. Saito, and A. Jorio, "Raman spectroscopy of carbon nanotubes," *Physics Reports,* vol. 409, pp. 47-99, Mar 2005.

[10] A. Jorio, A. G. Souza, G. Dresselhaus, M. S. Dresselhaus, A. K. Swan, M. S. Unlu, B. B. Goldberg, M. A. Pimenta, J. H. Hafner, C. M. Lieber, and R. Saito, "G-band resonant Raman study of 62 isolated single-wall carbon nanotubes," *Physical Review B,* vol. 65, p. 155412, Apr 15 2002.

[11] A. Jorio, R. Saito, J. H. Hafner, C. M. Lieber, M. Hunter, T. McClure, G. Dresselhaus, and M. S. Dresselhaus, "Structural (n, m) determination of isolated sin-

gle-wall carbon nanotubes by resonant Raman scattering," *Physical Review Letters,* vol. 86, pp. 1118-1121, Feb 5 2001.

[12] S. Iijima, "Helical Microtubules of Graphitic Carbon," *Nature,* vol. 354, pp. 56-58, Nov 7 1991.

[13] J. W. G. Wildoer, L. C. Venema, A. G. Rinzler, R. E. Smalley, and C. Dekker, "Electronic structure of atomically resolved carbon nanotubes," *Nature,* vol. 391, pp. 59-62, Jan 1 1998.

[14] M. Y. Sfeir, F. Wang, L. M. Huang, C. C. Chuang, J. Hone, S. P. O'Brien, T. F. Heinz, and L. E. Brus, "Probing electronic transitions in individual carbon nanotubes by Rayleigh scattering," *Science,* vol. 306, pp. 1540-1543, Nov 26 2004.

[15] D. Y. Joh, L. H. Herman, S. Y. Ju, J. Kinder, M. A. Segal, J. N. Johnson, G. K. L. Chan, and J. Park, "On-Chip Rayleigh Imaging and Spectroscopy of Carbon Nanotubes," *Nano Letters,* vol. 11, pp. 1-7, Jan 2011.

[16] Z. Yao, C. L. Kane, and C. Dekker, "High-field electrical transport in single-wall carbon nanotubes," *Physical Review Letters,* vol. 84, pp. 2941-2944, Mar 27 2000.

[17] Y. F. Chen and M. S. Fuhrer, "Electric-field-dependent charge-carrier velocity in semiconducting carbon nanotubes," *Physical Review Letters,* vol. 95, p. 236803, Dec 2 2005.

[18] M. P. Anantram, "Current-carrying capacity of carbon nanotubes," *Physical Review B,* vol. 62, pp. R4837-R4840, Aug 15 2000.

[19] K. H. Baloch, N. Voskanian, M. Bronsgeest, and J. Cumings, "Remote Joule heating by a carbon nanotube," *Nature Nanotechnology,* vol. 7, pp. 315-318, May 2012.

[20] I. Meric, M. Y. Han, A. F. Young, B. Ozyilmaz, P. Kim, and K. L. Shepard, "Current saturation in zero-bandgap, topgated graphene field-effect transistors," *Nature Nanotechnology,* vol. 3, pp. 654-659, Nov 2008.

[21] M. H. Bae, Z. Y. Ong, D. Estrada, and E. Pop, "Imaging, Simulation, and Electrostatic Control of Power Dissipation in Graphene Devices," *Nano Letters,* vol. 10, pp. 4787-4793, Dec 2010.

[22] E. Pop, D. Mann, J. Cao, Q. Wang, K. Goodson, and H. J. Dai, "Negative differential conductance and hot phonons in suspended nanotube molecular wires," *Physical Review Letters,* vol. 95, p. 155505, Oct 7 2005.

[23] M. A. Kuroda, A. Cangellaris, and J. P. Leburton, "Nonlinear transport and heat dissipation in metallic carbon nanotubes," *Physical Review Letters,* vol. 95, p. 266803, Dec 31 2005.

[24] E. Pop, D. A. Mann, K. E. Goodson, and H. J. Dai, "Electrical and thermal transport in metallic single-wall carbon nanotubes on insulating substrates," *Journal of Applied Physics,* vol. 101, p. 093710, May 2007.

[25] S. V. Rotkin, V. Perebeinos, A. G. Petrov, and P. Avouris, "An Essential Mechanism of Heat Dissipation in Carbon Nanotube Electronics," *Nano Letters,* vol. 9, pp. 1850-1855, May 2009.

[26] V. Perebeinos, S. V. Rotkin, A. G. Petrov, and P. Avouris, "The Effects of Substrate Phonon Mode Scattering on Transport in Carbon Nanotubes," *Nano Letters,* vol. 9, pp. 312-316, Jan 2009.

[27] S. V. Rotkin and A. G. Petrov, "Surface polariton scattering for charge transport and heat management in carbon-based heterogeneous electronics: Problem or solution?" in *Nanotechnology (IEEE-NANO), 2010 10th IEEE Conference on*, pp. 66-71.

[28] M. V. Fischetti, D. A. Neumayer, and E. A. Cartier, "Effective electron mobility in Si inversion layers in metal-oxide-semiconductor systems with a high-kappa insulator: The role of remote phonon scattering," *Journal of Applied Physics,* vol. 90, pp. 4587-4608, Nov 1 2001.

[29] D. Jena, T. Fang, Q. Zhang, and H. L. Xing, "Zener tunneling in semiconducting nanotube and graphene nanoribbon p-n junctions," *Applied Physics Letters,* vol. 93, Sep 15 2008.

[30] M. Shim, J. H. Back, T. Ozel, and K. W. Kwon, "Effects of oxygen on the electron transport properties of carbon nanotubes: Ultraviolet desorption and thermally induced processes," *Physical Review B,* vol. 71, May 2005.

[31] Y. Zhao, A. Liao, and E. Pop, "Multiband Mobility in Semiconducting Carbon Nanotubes," *IEEE Electron Device Letters,* vol. 30, pp. 1078-1080, Oct 2009.

CHAPTER 7
CONCLUSIONS AND FUTURE WORK

7.1 Conclusions

This work demonstrates the great advantages of one-dimensional materials, even as they are scaled. The results have furthered understanding of energy dissipation in carbon nanotubes (CNTs) and graphene nanoribbons (GNRs), as well as revised understanding of reliability and current carrying limits. Through in-air breakdown thermometry experiments [1, 2], a greater understanding was developed about the roles that environmental factors play in power dissipation. The thermal boundary conductance was measured and modeled in CNTs and was found to be as high as ~0.7 $WK^{-1}m^{-1}$ for the larger diameter CNTs. The thermal "footprint" on a dielectric was shown to have a large impact on the total power dissipation. As materials transition from two-dimensional planar devices to one-dimensional ones, the small size of these nanostructures improves energy efficiency from increased heat spreading. As a result, high current densities have been measured up to ~16 mA/μm for a CNT with a diameter of ~0.7 nm [1] and ~3 mA/μm for a GNR having a width of ~15 nm [2]. Such current densities are the highest possible in any diffusive conductor.

Further experiments performed in vacuum helped to investigate the current carrying potential in CNTs. Taking CNTs to such high fields produced higher currents than previously thought possible [3]. In semiconducting CNTs, impact ionization leads to an avalanche current, which was found to be strongly diameter dependent (~$\exp(-1/d^2)$) [4]. This diameter dependence allowed for an estimate of the inelastic optical phonon scattering length, $\lambda_{OP,ems} \approx 15d$ nm, obtained by fitting against a model of the high-field current "tail." In metallic CNTs, at very high fields not previously probed before (>10 V/μm), the current continues to increase with a slope ~0.5–1 μA/V, allowing m-CNTs to reach currents well in excess of 25 μA. From modeling, it is theorized that this excess current comes into play as a result of direct tunneling of carriers from the contacts into higher conducting subbands. Finally, the measurements in vacuum provided an opportunity to observe the impact of surface phonon polaritons (SPPs) [5, 6].

7.2 Future Work

While the performance of CNTs and GNRs shows great potential for integration into nanoelectronics, their maximum potential has not been achieved yet. Defects, edges, and surface roughness have been shown to degrade current drive. Even the smallest change in structure for these nanomaterials is enough to limit performance. Therefore, it will be important in the future to work on synthesis and fabrication techniques that allow for the production of pristine materials to better understand ultimate performance limits. Better methods of quantifying and measuring defects are also needed to establish clearer trends with defect density.

The quality of the CNT or GNR is not the only important issue. The choice of materials interfacing with the carbon allotrope will be just as important in maximizing performance and energy efficiency. A smoother dielectric than SiO_2 would provide better heat sinking (e.g. hexagonal boron nitride [7]). A better contact material might lower both electrical and thermal contact resistance. Furthermore, the geometry of the device will play a significant role as well. For example, a thinner dielectric would limit heat spreading and allow for better heat sinking into a bottom-gate. Top-gate dielectrics could help prevent breakdown by oxidation, leading to the observation of high field effects outside of vacuum.

Finally, it is hoped that this work will lead to new and exciting nanoelectronic devices. Already, the results of this research have been applied to engineer phase change memory utilizing CNTs as nanoscale electrodes [8]. To limit the application of this work to carbon based electronics, however, would be too shortsighted. The basic underlying principles of this research are not specific to carbon and can be applied to other one-dimensional systems. The benefits of being "nano" [9] will continue to drive innovation and motivate engineers and researchers to develop ways of fabricating other materials where they are comparable in size to CNTs or GNRs. Therefore, it is imperative to advance knowledge of transport at low dimensions.

7.3 References

[1] A. Liao, R. Alizadegan, Z. Y. Ong, S. Dutta, F. Xiong, K. J. Hsia, and E. Pop, "Thermal dissipation and variability in electrical breakdown of carbon nanotube devices," *Physical Review B,* vol. 82, p. 205406, Nov 5 2010.

[2] A. D. Liao, J. Z. Wu, X. R. Wang, K. Tahy, D. Jena, H. J. Dai, and E. Pop, "Thermally Limited Current Carrying Ability of Graphene Nanoribbons," *Physical Review Letters,* vol. 106, p. 256801, Jun 20 2011.

[3] Z. Yao, C. L. Kane, and C. Dekker, "High-field electrical transport in single-wall carbon nanotubes," *Physical Review Letters,* vol. 84, pp. 2941-2944, Mar 27 2000.

[4] A. Liao, Y. Zhao, and E. Pop, "Avalanche-Induced Current Enhancement in Semiconducting Carbon Nanotubes," *Physical Review Letters,* vol. 101, p. 256804, Dec 19 2008.

[5] V. Perebeinos, S. V. Rotkin, A. G. Petrov, and P. Avouris, "The Effects of Substrate Phonon Mode Scattering on Transport in Carbon Nanotubes," *Nano Letters,* vol. 9, pp. 312-316 2009.

[6] S. V. Rotkin, V. Perebeinos, A. G. Petrov, and P. Avouris, "An Essential Mechanism of Heat Dissipation in Carbon Nanotube Electronics," *Nano Letters,* vol. 9, pp. 1850-1855, May 2009.

[7] C. R. Dean, A. F. Young, I. Meric, C. Lee, L. Wang, S. Sorgenfrei, K. Watanabe, T. Taniguchi, P. Kim, K. L. Shepard, and J. Hone, "Boron nitride substrates for high-quality graphene electronics," *Nature Nanotechnology,* vol. 5, pp. 722-726, Oct 2010.

[8] F. Xiong, A. D. Liao, D. Estrada, and E. Pop, "Low-Power Switching of Phase-Change Materials with Carbon Nanotube Electrodes," *Science,* vol. 332, pp. 568-570, Apr 29 2011.

[9] R. P. Feynman, "There's Plenty of Room at the Bottom," *Engineering and Science,* pp. 22-36, 1960.

APPENDIX A

PROCEDURES FOR MAKING CNTFETS

A.1 Cleaning

1. Degrease wafer (Acetone → Methanol → Isopropyl Alchohol).
2. Perform a quick (~5-10 sec) buffered oxide etch (BOE) 10:1 HF.
3. Perform SC2 (~1:1:6 HCl:H_2O_2:H_2O) at ~70-8 °C.

A.2 Etch Alignment marks

Note: Alignment marks should be etched into SiO_2. Metallic alignment marks are not used so as to not affect CNT growth.

1. Degrease wafer.
2. Bakeoff at 125 °C for at least 120 sec.
3. Spin on HMDS and then PR S1813 at around 3000 RPM for 30 sec.
4. Prebake at 110 °C for 75-90 sec.
5. Expose wafer using contact aligner and mask Popalign. Expose with a dose of ~60 mJ.
6. Develop off PR with MF319.
7. Postbake at 110 °C for at 120-135 sec.
5. Use CHF3 in the plasma freon RIE to etch. Make sure there is about 500A of oxide left otherwise the PR might lift off during step 6. Alternatively, skip step 5 and perform wet etch the whole way.
6. Etch down to Si with a BOE etch.
7. Remove PR in acetone.

A.3 Catalyst Deposition

1. Bakeoff at 200C for at least 120 sec.
2. Spin on PMGI SF6 at 5000 RPM for 30 sec.
3. Postbake at 175 °C for 5 min exactly.
4. Spin on PR S1813 at 5500 RPM for 30 sec.
5. Prebake at 110 °C for 75-90 sec.

6. Expose using quintel and Popmetal_catalyst mask. Expose with a dose of ~60 mJ.
8. Develop off PR with MF319. MAKE SURE THAT YOU CAN SEE THE SUBSTRATE THROUGH THE CATLYST HOLES.
9. Postbake at110 °C for 120-135 sec.
10. Deposit 2 Å of Fe using the CHA electron-beam (e-beam) evaporator. First keep sample out of the deposition pathway while establishing a slow rate ~0.1-0.2 Å/sec. Then rotate in sample.
11. Liftoff in remover PG. Put the remover PG in a crystal dish and put it on the brown hotplate in the solvent hood located in the general chemistry room (~70 °C) for ~30 min.

A.4 CNT Growth

1. Anneal sample under Ar at 900 °C at least for 30 min.
2. (Optional) quickly open split tube furnace to allow for rapid cooling. BE CAREFUL NOT TO BURN YOURSELF.
3. Switch on carbon carrier gas and H_2 while turning off Ar.
4. Lower temperature to 400 °C in Ar environment.
5. Anneal in Ar/H_2 environment at 400 °C for at least 30 min.
6. Cool back to room temperature in Ar environment.
7. Check growth under scanning electron microscope before moving on.

A.5 Metallization

1. Bakeoff at 200 °C for at least 120 sec.
2. Spin on PMGI SF6 at 3500 RPM for 30 sec.
3. Postbake at 165 °C for 5 min exactly.
4. Spin on PR S1813 at 5000 RPM for 30 sec.
5. Prebake at 110 °C for 75-90 sec.
6. Expose using quintel and Popmetal_catalyst2 mask. Expose around ~42-43.5 mJ.
7. Develop off PR with MF319. MAKE SURE THAT ALL PMGI IS REMOVED AND UNDERCUTTING PR (~50-60 sec).
8. Postbake at 125 °C for 30 sec.

9. Develop in MF319 for 5 sec.

10. Postbake at 110 °C for ~90 sec.

11. Deposit metal using the CHA evaporator. Operate CHA in manual mode for better results. If depositing Ti, move sample out of deposition pathway and deposit Ti until pressure starts to drop (~5-6 nm).

12. Liftoff in remover PG. Put the remover PG in a crystal dish and put it on the brown hotplate in the solvent hood located in the general chemistry room. Take 30min to do liftoff. When removing the sample from remover pg you should soak it in IPA for a bit and then degrease it.

APPENDIX B

MATERIALS DEPOSITION ON CARBON NANOTUBES

Depositing materials on top of carbon nanotubes (CNTs) allows for the fabrication of top-gated devices [1] as well as other novel devices such as phase change memory [2]. However, not all of these materials will necessarily be compatible with CNTs. We use electrical measurements and Raman spectroscopy to check the compatibility between CNTs and other materials. We investigate AlO_x and TiO_x as potential top-gate dielectrics and the chalcogenide $Ge_2Sb_2Te_5$ (GST).

B.1 AlO_x

Two nanomemters of Al was evaporated on top of a typical three-terminal CNT device and on top of a random CNT network. Following evaporation, samples were left in air for more than 24 hours and were baked on a hotplate at 200 °C for 5 minutes. Subsequent electrical measurements on devices with no CNTs (the electrodes are connected through by oxide instead of CNTs) show no conduction, indicating the Al has fully oxidized or that all percolating pathways of Al have been cut off. Figure B.1A and B shows representative Raman spectra for a CNT before Al deposition and after baking the sample initially shows no additional decrease in the G-peak to D-peak intensity ratio (I_G/I_D).

The electrical measurements of the device with AlO_x are shown in Fig. B.1C. The initial measurement is typical of CNTs measured without oxide. However, on the

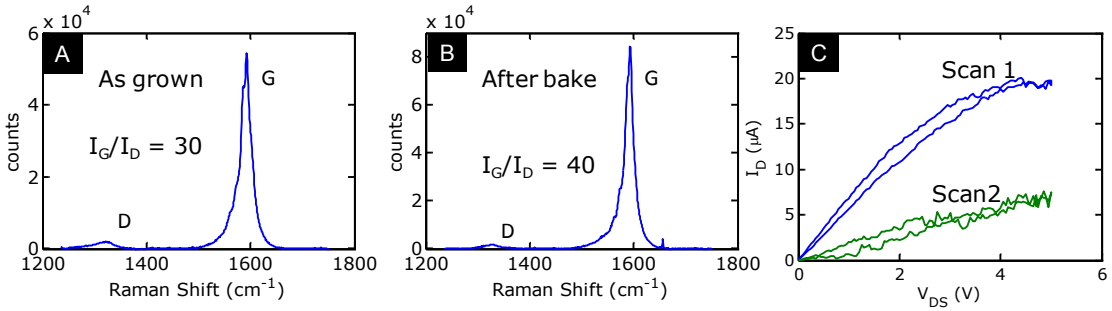

Fig. B.1. (A) Raman spectrum of a CNT network as grown, with $I_G/I_D = 30$. (B) Raman spectrum of a CNT network with AlO_x on top, with $I_G/I_D = 40$. (C) Electrical measurements performed in air of devices with AlO_x. Each subsequent measurement damages the CNT until it the device stops conducting altogether.

subsequent sweep, the current drops by a factor of 4. Each subsequent sweep shows a lower current, indicating that the CNT is being damaged during the sweep. Eventually, no current flows between the electrodes and the circuit is open.

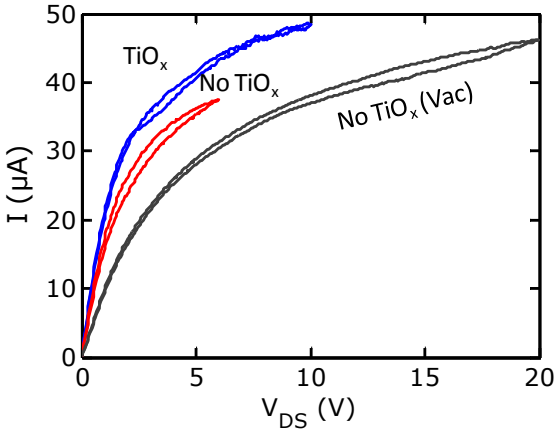

Fig. B.2. I-V measurements of the same CNT measured in air (red), in vacuum (black), and in air and covered with TiO_x. The current is the highest for a CNT covered with TiO_x.

B.2 TiO_x

An alternative to AlO_x is TiO_x. Similar to the way AlO_x is deposited, 2 nm of Ti is evaporated on top of three-terminal CNT devices. The samples are left in ambient air for 24 hours and baked on top of a hotplate at 200 °C for 5 min. Measurements of devices with no CNTs show no conduction. Measurements of CNT devices covered with TiO_x show repeatable I-V_{DS} curves, unlike CNTs with AlO_x on top. Figure B.2 shows that the currents in the TiO_x covered CNTs are actually higher than CNTs measured in air and vacuum. One possible explanation for the higher current could be that the TiO_x is screening surface phonon polaritons from the SiO_2 surface.

B.3 $Ge_2Sb_2Te_5$

GST was sputtered onto a random CNT network. Figure B.3 shows the Raman spectra for the initial as grown CNT network, the CNT network with as sputtered

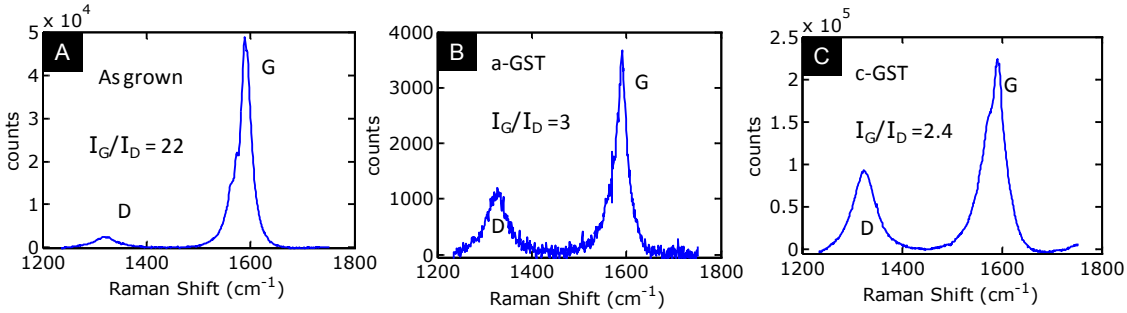

Fig. B.3. (A) Raman spectrum of a CNT network as grown, with $I_G/I_D = 22$. (B) Raman spectrum of a CNT network with as sputtered amorphous GST on top, showing $I_G/I_D = 3$. (C) Raman spectrum of a CNT network with crystalline GST on top, showing $I_G/I_D = 2.4$. The increase of the D-peak relative to the G-peak indicates that the CNT network is damaged by GST sputtering.

amorphous GST on top, and the sample after crystallizing the GST. The GST is crystallized by heating it on a hotplate. The GST is capped by SiO_2 to prevent oxidation. The D-peak intensity increases relative to the G-peak intensity, suggesting that defects, strain, or doping is introduced from the sputtered GST.

B.4 References

[1] A. Javey, J. Guo, D. B. Farmer, Q. Wang, D. W. Wang, R. G. Gordon, M. Lundstrom, and H. J. Dai, "Carbon nanotube field-effect transistors with integrated ohmic contacts and high-k gate dielectrics," *Nano Letters,* vol. 4, pp. 447-450, Mar 2004.

[2] F. Xiong, A. D. Liao, D. Estrada, and E. Pop, "Low-Power Switching of Phase-Change Materials with Carbon Nanotube Electrodes," *Science,* vol. 332, pp. 568-570, Apr 29 2011.